SMALL DUAL-CHANNEL WATERJET PROPULSION MODULE DESIGN AND DEVELOPMENT

BY

COREY MURPHY

A THESIS SUBMITTED IN PARTIAL FULFILLMENT OF THE

REQUIREMENTS FOR THE DEGREE OF

MASTER OF SCIENCE

IN

MECHANICAL ENGINEERING AND APPLIED MECHANICS

UNIVERSITY OF RHODE ISLAND

2021

MASTER OF SCIENCE IN MECHANICAL ENGINEERING THESIS

OF

COREY MURPHY

APPROVED:

Thesis Committee:

Major Professor Bahram Nassersharif

Stephen Jordan

Richard Vaccaro

Michael Antosh

Brenton DeBoef
DEAN OF THE GRADUATE SCHOOL

UNIVERSITY OF RHODE ISLAND

2021

ABSTRACT

A dive propulsion vehicle (DPV) is a specific type of underwater propulsion module used as a recreational tool to navigate underwater. With an increase in DPV popularity over the past decade, a significant amount of research, design, and development has been conducted to create a variety of commercially offered DPV's boasting impressive performance numbers. Unfortunately, the cost of these performance-oriented DPV's can be excessive for the average consumer. Although alternative, more affordable options exist, these DPV's typically lack the high-performance characteristics most consumers seek. This issue with current commercially offered DPV's led to further research to identify new methods to improve the performance of underwater propulsion modules at a reduced cost.

The primary goal of this study is to research, design, and develop a compact, high-performance underwater propulsion module that uses an innovative dual-channel nozzle to create additional, potentially efficient, thrust at a reduced cost. This dual-channel nozzle design consists of a primary inner nozzle and secondary outer nozzle that creates a Venturi tunnel between the two nozzles. The thrust generated solely by the inner channel nozzle creates a suction effect in the tunnel between the two channels, allowing for additional freestream fluid to enter the intake of the outer channel nozzle and conjoin with the energized fluid in the inner channel nozzle. This would lead to an increase in mass flow rate exiting the propulsion module, generating additional thrust. The entirety of the propulsion module (channel, nozzles, impellers) was designed and developed from scratch and was 3D printed (excluding mechanical components) to prioritize reduced costs.

Several iterations of this underwater propulsion module were designed, manufactured, and tested to improve the functionality and performance of the module. A complete control system was not implemented in this final prototype. Therefore, all of the tests were completed using a static test apparatus. The dual-channel nozzle design was not proven to generate efficient thrust when the module's forward velocity is greater than 0; however, the design was proven through significant data and testing to generate additional thrust when the module's forward speed is equal to 0.

ACKNOWLEDGMENTS

Throughout my time as a graduate student at the University of Rhode Island, I have received a great deal of support and assistance. I would first like to take this opportunity to thank my Major Professor and project sponsor, Dr. Bahram Nassersharif. Dr. Nassersharif's wide range of knowledge and expertise was an invaluable resource that he never hesitated to share with me along my journey to complete my thesis. Despite the many challenges I faced along the way, he continued to patiently provide me with the vision, encouragement, and advice required to succeed in my research project. I have gained a wealth of knowledge and refined countless skills working for Dr. Nassersharif and can confidently say I have grown significantly as an engineer and professional under his guidance.

I would also like to thank the University of Rhode Island and my thesis committee members, Dr. Stephen Jordan, Dr. Richard Vaccaro, and Dr. Michael Antosh, for providing me with an exceptional mechanical engineering education over my six years at the institution. My time at the university has prepared me for a rewarding engineering career as I move on from academia.

Finally, I would like to thank my parents for their unwavering support and motivation throughout my years of study. Without them, this accomplishment would not have been possible.

TABLE OF CONTENTS

LIST OF FIGURES

LIST OF TABLES

DEFINITION OF ACRONYMS

Acronym	Definition
ABS	Acrylonitrile Butadiene Styrene
AWG	American Wire Gauge
BEC	Battery Eliminator Circuit
BLDC	Brushless DC Electric Motor
CAD	Computer Aided Design
CFD	Computational Fluid Dynamics
COG	Center of Gravity
DPV	Dive Propulsion Vehicle
ESC	Electronic Speed Controller
FDM	Fused Deposition Modeling
IGBT	Insulated-Gate Bipolar Transistor
LiPo	Lithium Polymer Battery
MCE	Mechanical Engineering
MCU	Microcontroller Unit
MOSFET	Metal-Oxide-Semiconductor Field-Effect Transistor
PETG	Polyethylene Terephthalate Glycol
PLA	Polylactic Acid
PVA	Polyvinyl Alcohol
RPM	Revolutions Per Minute
SSD	Solid State Drive
UBEC	Universal Battery Eliminator Circuit
vRAM	Video Random Access Memory

1. Significance of Study

1.1 Dive Propulsion Vehicles

This study's original inspiration can be traced to exploring the current performance available in commercially offered recreational underwater scooters, also known as Dive Propulsion Vehicles (DPV). Over the past decade, the market for recreational DPVs has exhibited consistent growth, with many companies creating a variety of products aimed at consumers looking for an enhanced underwater recreational experience. A substantial amount of research, design, and development has been conducted and published in the past several years to improve underwater scooters' performance. Although many of the current "high-end" DPVs available offer the consumer a compelling package of performance, the cost of these products routinely exceeds $1000, where some top-of-the-line offerings are commanding a price tag above $3000. "Entry-level" DPVs typically range in price from $300 to $800. However, the performance available from these products can leave the consumer with something more to be desired. A majority of the preliminary market research was focused on these entry-level DPVs to identify potential ways to increase performance at a decreased cost.

All entry-level DPVs, along with many high-end offerings, share a similar open-impeller propulsion design, utilizing a lead-acid or LiPo battery and brushed motor connected via a driveshaft to an impeller that intakes fluid through the exposed caged housing. The Yamaha RDS250, displayed in Figure 1.1 below, represents a DPV that depicts this entry-level DPV propulsion design method.

Figure 1.1: YAMAHA RDS250[17]

Priced at $550, the YAMAHA RDS250 targets consumers who prefer extended run time (up to 2 hours) with the sacrifice of top speed (4 km/h) at a relatively standard maximum operational depth of 30 m[17]. This DPV is also on the heavier side, weighing in at 8.2 kg due to its large lead-acid battery. Entry-level DPVs that aim for increased top speeds typically come with primary performance sacrifice in run time. The Lefeet S1, displayed in Figure 1.2 below, is very light at 2.3 kg and operates at a maximum depth of 40 m with a top speed of 5.4 km/h, but is only rated to run at this speed for 30 minutes[11].

Figure 1.2: Lefeet S1[11]

Increasing the top speed of a DPV also clearly comes with the significant sacrifice of the cost when considering the Lefeet S1 is priced towards the upper range of entry-

level DPVs at $800. For a ~35% increase in top speed, the consumer must sacrifice a ~75% reduction in run time and a ~45% increase in price.

Commercial DPVs employing alternative propulsion methods that provide enhanced top speed performance were also researched. The company SCUBAJET is the only DPV manufacturer that utilizes an alternative method for its propulsion designs. In contrast to the previously described DPVs, the SCUBAJET NEO ($1250), displayed in Figure 1.3 below, generates thrust from a single channel waterjet system that uses a "honeycomb" inlet design to intake fluid from the surrounding environment.

Figure 1.3: SCUBAJET NEO[14]

Boasting an impressive maximum thrust output of 22 lbs, a top speed of 8 km/h, and weighing only 2.9 kg, the SCUBAJET NEO offers an attractive package for consumers who prioritize top speed and maneuverability[14]. This device's 100 Wh battery is only rated to run at its top speed in "Full" mode for 15 minutes, with a "Cruise" and "Low" battery setting that yield operational times of 30 and 60 minutes, respectively. At a cost premium of ~56% over the Lefeet S1, the SCUBAJET NEO cannot be considered an entry-level product. However, the ~48% improvement in top speed demonstrates the potential of implementing a waterjet propulsion system for additional thrust instead of the traditional caged impeller approach.

Waterjet propulsion technology has yet to reach the entry-level DPV market for many reasons, mainly due to the increased costs associated with the implementation. A conventional single-channel waterjet system requires larger batteries and powerful motors for the system to run efficiently[5]. Additional costs associated with manufacturing a complex intake, fluid channel, nozzle, and housing for the system must also be considered. Generating thrust values capable of producing high top speed performance also dramatically impacts the run time of the DPV. These performance and cost issues with current waterjet DPVs led to a further investigation into how they could be improved.

1.2 Project Objectives

The primary goal of this study is to develop a fully submersible dual-channel waterjet propulsion module to research, test, and evaluate the innovative dual-channel design's ability to create additional efficient thrust while prioritizing reduced costs. Given that this study is a design project starting from scratch, all three phases of research, design, and development will need to be addressed to achieve a final, operational prototype. Multiple objectives first need to be addressed. These objectives are outlined below.

i. Generate and theoretically evaluate innovative dual-channel waterjet concepts that could aid in creating additional hydrodynamic thrust
ii. Research and identify innovative additive manufacturing methods to reduce costs
iii. Design and manufacture a suitable testing apparatus to test various propulsion module components and prototypes

iv. Test provided motors to determine the suitable choice of motor for generating hydrodynamic thrust

v. Design, develop and test various impellers to determine the optimal impeller for generating efficient hydrodynamic thrust

vi. Design, develop and test various nozzles to determine the optimal nozzle for generating additional hydrodynamic thrust

vii. Design, develop and test various waterjet propulsion module prototypes to optimize the functionality of the module

viii. Implement and test innovative dual-channel nozzle designs with final module prototype to determine if this new concept creates additional efficient hydrodynamic thrust

1.3 Potential Applications

Although inspired by the unique performance capabilities of DPV's, this study was not solely focused on creating an improved propulsion module that only satisfies the requirements of a recreational DPV. Instead, the waterjet propulsion module concept and prototype described in this thesis were created to prioritize reduced costs, high performance, and versatility. This waterjet propulsion module's innovative dual-channel design concept could be used for several applications with some modifications.

There are multiple recreational applications for which this propulsion module could be used. Of course, this module could be modified to fulfill the requirements of a recreational hand-held DPV. Much of the research and findings from this study could be directly applied to create an improved recreational DPV to compete in the

consistently growing DPV market. This propulsion module could also be used as a versatile alternative propulsion device mounted to a paddle board, boogie board, or small boat. A set of detachable mounts could be sold alongside the propulsion module to attach the module directly to the consumer's recreational item of choice. The user would be able to control the thrust output using a handheld controller of the module to add to their recreational enjoyment.

Over the past few decades, there has been an increasing effort to further humanity's understanding of the ocean and its existing life forms. Small underwater vehicles have also become prevalent in the field of marine research. With the improvement of technology, exploring the ocean has become a more feasible prospect with the help of these small underwater vehicles[12]. This specific underwater propulsion module described in this thesis would require heavy modifications to allow the device to function correctly in the harsh environment of the deep ocean. However, many of the findings conducted in this study could be applied to future research-specific underwater vehicles.

The Navy also employs underwater propulsion modules for various tasks, including marine research and surveillance. Implementing an autonomous control system and further durability improvements could make this propulsion module a valuable tool for Navy operations.

2. Concept Generation

2.1 Engineering Design Specifications

Before the commencement of research and development, a list of engineering design specifications for the propulsion module was determined. These parameters, listed in Table 2.1 below, were set to adhere to the propulsion module's previously specified usage cases.

Table 2.1: Engineering Design Specifications

Production Cost	< $100
Construction	3D Printed
Thrust Output (v = 0)	10-20 lbs
Length	< 12 in
Diameter	< 6 in
Battery	Modular, Rechargeable
Operational Time	> 30 min

One of the primary objectives of this project was to keep the overall production cost of the propulsion module as low as possible, leading to an optimistic production cost target of less than $100. It was crucial to consider how the module that would be manufactured to reach the cost target. It was determined that the propulsion module (excluding battery/motor/driveshaft) would be constructed with additive manufacturing technology. 3D printing offers an exceptional amount of flexibility in terms of the geometries produced and the materials used. The speed at which a design can be manufactured and experimentally tested is significantly faster than many traditional methods. Crucially, 3D printing was by far the most cost-effective method

of manufacturing for this study as only a small number of prototypes will need to be produced.

A target thrust output for the module when its forward velocity is equal to 0 was set to a range of 10-20 lbs. This range references the typical thrust outputs of the DPV's discussed above, with 10 lbs reflecting the output of current entry-level DPV models and 20 lbs reflecting the output of current high-end DPV models. Achieving a thrust output as close to 20 lbs as possible at a reduced cost served as a baseline target.

Ideally, this propulsion module would be as small as possible to decrease weight and increase performance/efficiency. Dimensional specifications of less than 12 inches long with a diameter less than 6 inches were selected. These specifications would keep the module to a desired compact size. The dimensions also do not exceed the maximum build area dimensions of the 3D printers available for this study, ensuring that larger module sections can be printed in one piece.

The battery must be modular and rechargeable to increase versatility and improve usability. Once the module's battery is depleted, the user can swap in a fully charged battery to immediately resume activities. This allows more tests to be completed with the module in a significantly reduced amount of time.

The final engineering design specification that was determined for this propulsion module was the operational run time. An operating run-time target of more than 30 minutes was selected to compete with some of the current high-end DPV's. This specification does not require the module to operate at maximum thrust to

achieve the set run time. Instead, this value can be achieved when the module is running at a lower throttle setting.

Although these initial engineering design specifications are not perfectly replicated in the final propulsion module prototype, they served as a basic set of guidelines to narrow the design project's focus.

2.2 Preliminary Design Concept

A preliminary design concept was created (based on engineering design specifications) to explore an innovative waterjet design methodology that utilizes two cylindrical channels (inner and outer). This innovative concept creates additional efficient thrust via the Venturi Effect as the module's forward velocity increases. Displayed in Figure 2.1 and Figure 2.2 below are a cross-sectional sketch and a simplified CAD model of the preliminary dual-channel waterjet propulsion module concept.

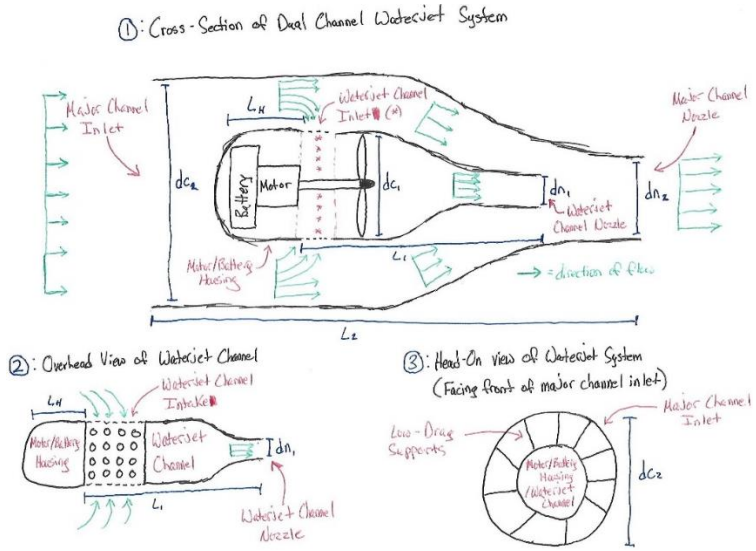

Figure 2.1: Preliminary Dual Channel Waterjet Propulsion Module Concept Sketch

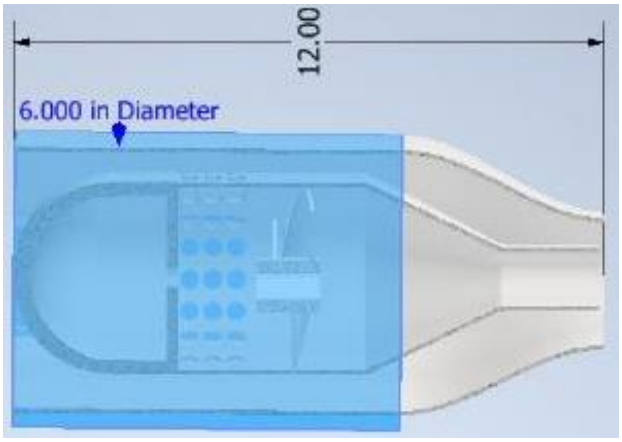

Figure 2.2: Preliminary Dual Channel Waterjet Propulsion Module CAD Model

The inner channel houses the main waterjet propulsion components (battery, motor, driveshaft, impeller). It will be responsible for creating a specified amount of thrust when the module's forward velocity equals 0. A "honeycomb" inlet will be featured on this inner channel with openings designed using specific geometry to mimic the shape of the freestream fluid flow in the outer channel, maximizing the intake efficiency of fluid flow[9]. The fluid closest to the inner channel boundary is "sucked" through the inlet caused by the rotating impeller's negative pressure. The fluid is then energized as it passes through the impeller, increasing the velocity of the flow. Following this process, the fluid will flow into the inner channel nozzle, where the speed of the flow will continue to increase. Water is an incompressible fluid, therefore decreasing the nozzle diameter about the channel's diameter will result in an increased fluid velocity. The ideal diameter of the waterjet nozzle is directly dependent on the diameter of the waterjet channel[16]. The battery and motor housing

will be fully waterproofed with a cylindrical opening, sealed with a bearing, for the impeller driveshaft.

The outer channel is the larger of the two channels. It encompasses the inner duct and serves as the study's primary focus. The outer channel's first purpose is to intake fluid from the upstream environment at the outer-channel inlet. This cylindrical inlet will essentially be entirely open for the freestream of fluid flow at the front of the module. The inlet will be designed to have a very close diameter to the diameter of the module itself, maximizing the total volume of fluid that can be brought into the waterjet system. Once the fluid enters the outer channel inlet, it will flow towards the inner channel inlet. The fluid closest to the inner-channel boundary will be "sucked" through the waterjet inlet caused by the increased mass flow rate from the impeller. The fluid that does not enter the waterjet inlet will continue to flow between the exterior wall of the inner channel and the outer channel's interior wall. The distance between these two walls will continue to decrease until reaching the inner channel nozzle.

Gradually decreasing the distance between these two walls creates a constrained section (or choke) of the area between the outer and inner channels, effectively creating a Venturi nozzle. When the fluid flows through this constrained section, it will experience a decrease in the fluid pressure caused by the Venturi effect, increasing the fluid flow velocity[10]. Increasing the fluid velocity that does not enter the inner waterjet channel should theoretically result in additional thrust gains once this flow conjoins with the flow exiting the inner waterjet nozzle. An increase in the module's forward velocity will lead to a rise in the speed of the fluid at the inlet,

therefore increasing the speed of the fluid once it reaches the constrained section of the channel. Theoretically, the greater the module's forward velocity, the greater the thrust gains due to the Venturi effect. Consequently, the outer channel's additional surface area will create further drag/frictional-related losses that could outweigh the benefits of the Venturi effect.

Once the fluid flows past the constrained section, the flow will reattach with the energized flow exiting the nozzle's waterjet channel. The conjoined flow will then pass through the outer channel nozzle, where it will then exit from the rear of the module. It will be crucial to design this outer channel nozzle to reattach both flows as efficiently as possible. Many issues could arise during this process caused by the flow's different velocities, such as creating unwanted vortices that would disturb the direction of flow, leading to a decrease in overall thrust output and efficiency[6]. If designed correctly, the outer channel nozzle will eliminate these issues and further increase the total fluid velocity, increasing the system's overall thrust output.

The inner channel will be suspended within the outer channel. Low drag supports, designed with inspiration from shark-fin surfaces, will be mounted to the internal channel's exterior wall and the interior wall of the outer channel. It will be ideal to require as few supports as possible as they will inherently add surface area and consequently drag to the system.

The preliminary design concept discussed above was heavily researched before conducting physical testing. Figure 2.3 on the following page displays an advanced CAD model of this initial concept.

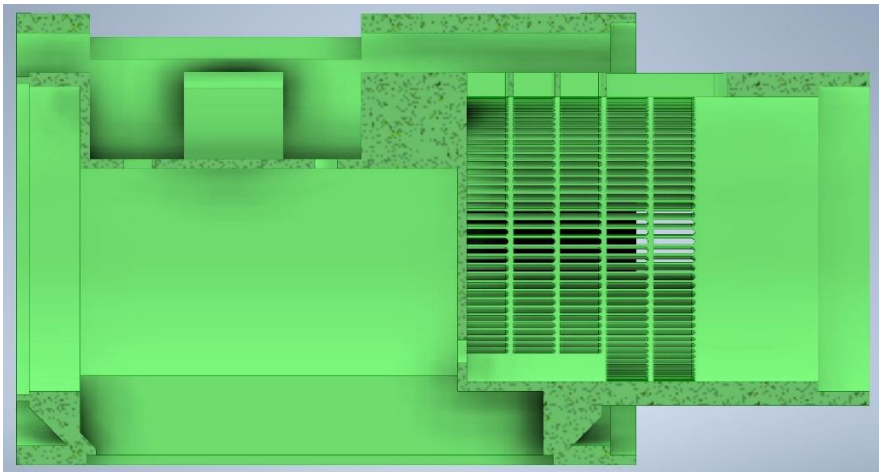

Figure 2.3: Advanced CAD Model of Preliminary Design Concept

After further evaluation and testing of waterjet mechanical components, an inherent flaw was discovered with this preliminary design concept. The power produced from the tested motor and impeller combinations would not efficiently generate enough suction to move the volume of fluid from the outer-channel intake into the inner-channel intake. Therefore, the module's max thrust output would be decreased with this specific dual-channel design compared with the thrust output of the single-channel alone. A more powerful motor and larger battery combination would be required to generate the necessary thrust to allow this concept to operate efficiently. Upgrading these two components would increase the cost of the module increase the module's size to accommodate. Due to these flaws, the preliminary design concept was modified into a new dual-channel design concept that would continue as the primary focus of this study.

2.3 Modified Design Concept

A modified design concept that utilizes a dual-channel nozzle was proposed to address the issues with the preliminary design concept. This design will use similar ideas from the previous iteration. Still, it will instead focus on harnessing the benefits of a secondary outer channel attached to the nozzle of the propulsion module.

The propulsion module will be designed as a single channel waterjet system responsible for creating the hydrodynamic thrust. Attached to the primary channel of the propulsion module will be an innovative dual-channel nozzle that will be explored throughout this study. Figure 2.4 below is a basic cross-sectional CAD rendering that displays this proposed design concept.

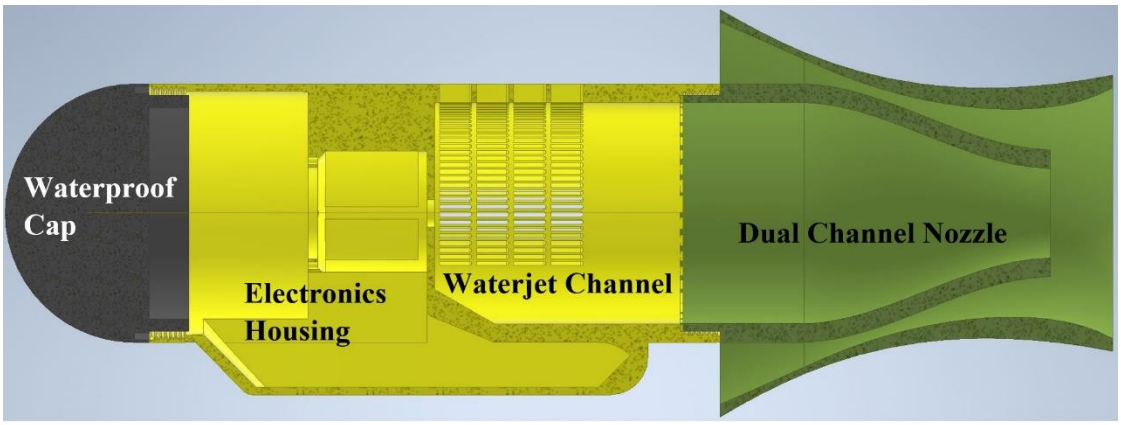

Figure 2.4: Modified Design Concept CAD Model

The electronics housing will store the electronic components necessary to power the propulsion module. These components include the battery, motor, speed controller and wiring. The motor will be mounted along the centerline of the module. A cylindrical opening for the motor's driveshaft will be designed into the wall connecting the electronics housing and waterjet channel, sealed with a bearing. It will

be crucial that this compartment is adequately waterproofed with the design of a waterproof cap to ensure the electronics housed within are not damaged when the module is submerged. The components must be thoughtfully packaged within the electronics housing to keep the compartment as compact as possible without inducing any thermal compromises.

The primary waterjet channel, connected directly to the electronics housing, will include the module's main intake and house the driveshaft and impeller assembly. The impeller will be connected to the motor's driveshaft and located just ahead of the "mesh" shaped intake. Fluid from the surrounding environment will be drawn through the intake caused by the rotating impeller's negative pressure. The fluid is then energized as it passes through the impeller, increasing the velocity of the flow. Following this process, the energized fluid will then flow into the inner channel of the dual-channel nozzle, further increasing the velocity of the flow. The length and diameter of the inner section of the nozzle will be optimized for maximum performance relative to the waterjet channel. The high-velocity fluid will then exit the nozzle's inner channel and enter the final stage of the nozzle's outer channel.

The outer channel of the dual-channel nozzle encompasses the nozzle's inner duct and is responsible for creating additional, efficient hydrodynamic thrust. This outer channel can be split into three stages, as depicted in Figure 2.5 on the following page.

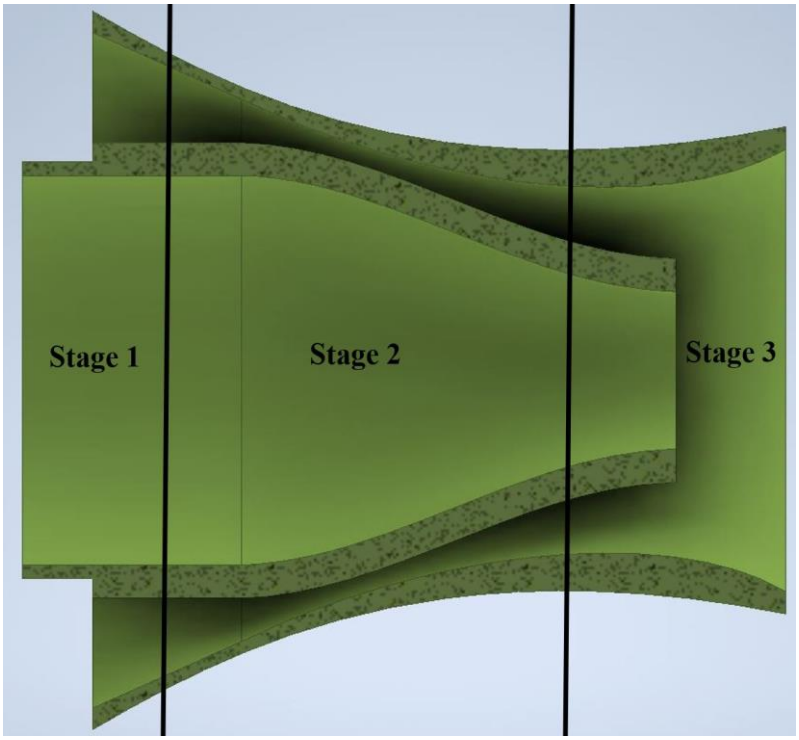

Figure 2.5: Schematic of Dual Channel Nozzle Stages

Stage 1 represents the outer channel's inlet. The inlet is completely exposed to the underwater environment's free stream of fluid. When the module has a forward velocity equal to 0, the fluid that enters the inlet at stage 1 is solely dependent on what is occurring in stage 3. The high-velocity fluid exiting the inner channel flows directly into stage 3 of the outer channel. This fluid flow will create a low-pressure "suction" zone between the inner wall of the outer channel and the stream of fluid. The low-pressure zone created in stage 3 will permeate throughout the length of the outer channel into the inlet section at stage 1. Fluid from the external environment closest to the outer channel boundary will be drawn through the inlet at stage 1. It will be crucial to maximize the hydrodynamic thrust exiting the nozzle's inner channel. Any increase in fluid velocity entering stage 3 from the inner section of the nozzle will

result in a greater low-pressure zone, increasing the velocity of fluid entering the outer section of the nozzle at stage 1.

The volume of fluid that enters stage 1 of the outer channel will then move towards stage 2. At this stage, the distance between the outer wall of the inner channel and the inner wall of the outer channel gradually decreases to create a constrained section, effectively creating a Venturi tunnel. When the fluid flows through this constrained section, it will experience a decrease in the fluid pressure caused by the Venturi effect, increasing the fluid flow velocity. This fluid volume will then continue to flow into stage 3 at an increased velocity. The flow conjoins with the high-velocity fluid exiting the nozzle's inner channel, theoretically resulting in additional thrust gains due to an increased mass flow rate of fluid exiting the module at stage 3.

A basic CFD model was created to demonstrate fluid flow dynamics within this preliminary dual-channel nozzle. Two different velocity inlets were used in this model. The first inlet was positioned at the start of the inner channel to replicate the flow of energized fluid coming from the waterjet channel. A 2 m/s velocity magnitude was chosen for this inlet based on preliminary waterjet performance expectations. The second inlet was positioned at the start of the fluid domain. A 1 m/s velocity magnitude was set for this inlet to replicate the propulsion module's 1 m/s forward velocity. Figures 2.6, 2.7, and 2.8 display the velocity contours, velocity vectors, and pressure contours along the X-Y plane of the nozzle, respectively.

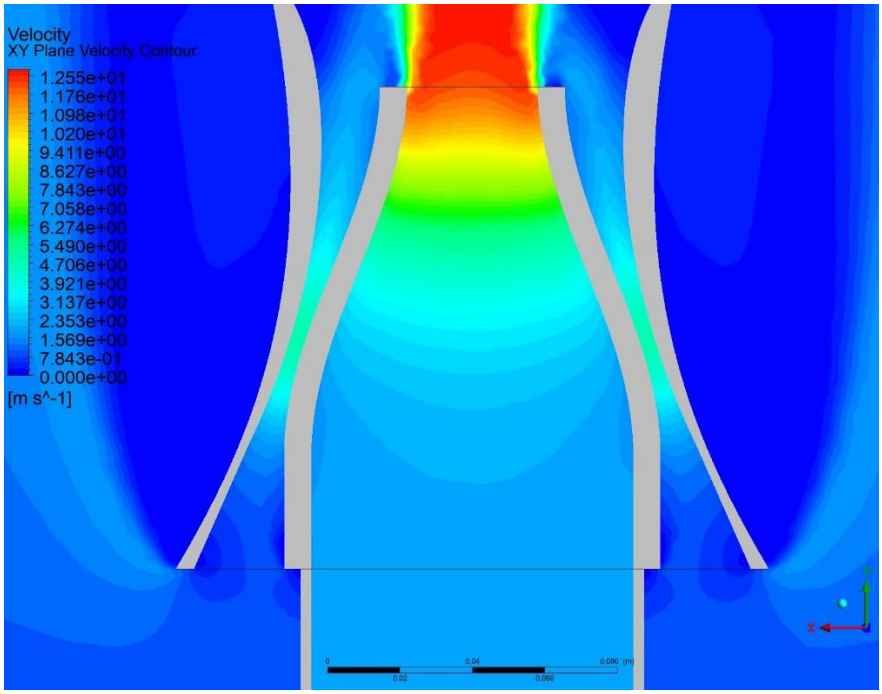

Figure 2.6: Dual Channel Nozzle Velocity Contours

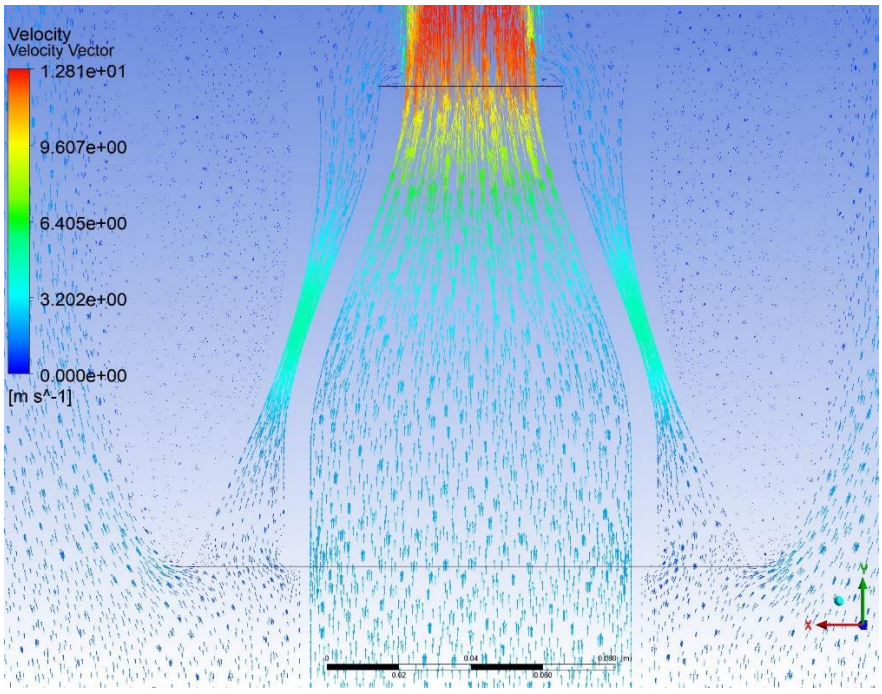

Figure 2.7: Dual Channel Nozzle Velocity Vectors

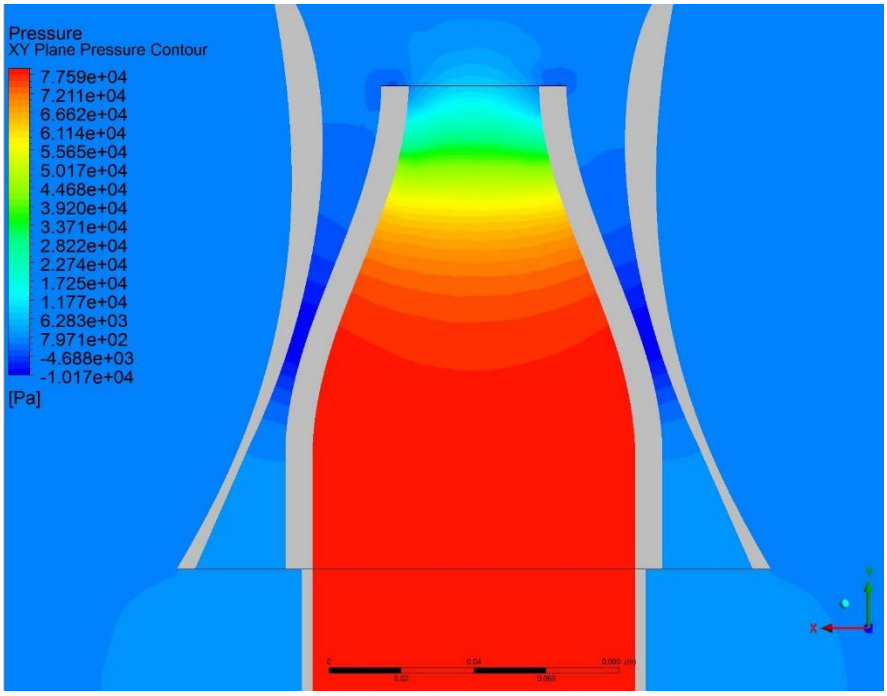

Figure 2.8: Dual Channel Nozzle Pressure Contours

Fluid closest to the outer channel boundary is drawn into the outer channel intake at stage 1 and continues to flow towards the constrained Venturi tunnel section at stage 2. At this point, the volume of fluid experiences a drop in pressure and an increase in velocity. The fluid closest to the inner channel wall then conjoins with the energized fluid exiting the inner channel, computationally confirming the expected dynamics of the nozzle.

It will be crucial to optimize the nozzle's outer channel (length, diameter, taper angle, overlap percentage) relative to the nozzle's inner channel to ensure the dual-channel nozzle operates as efficiently as possible. Likewise, it will be essential to select a material for constructing the dual-channel nozzle that minimizes the coefficient of friction along the nozzle walls. Any additional friction introduced to the

flow of fluid along the nozzle walls will reduce the performance and efficiency of the propulsion module.

3. Research, Design, and Development Procedures

3.1 Project Timeline

A simplified timeline of this project from start to completion can be divided into 15 total stages. These stages, along with their definitions and completion dates, can be viewed in Table 3.1 below.

Table 3.1: Project Timeline

Project Stage	Description	Start Date	Completion Date	Duration
1	Concept Generation	Sep-20	Nov-20	2 months
2	Testing Apparatus Design and Build	Oct-20	Oct-20	1 month
3	Motor Testing	Nov-20	Nov-20	1 month
4	CFD Simulation Work	Nov-20	Jan-21	3 months
5	Initial Impeller Design and Manufacturing	Nov-20	Jan-21	2 months
6	Prototype V1 Design and Manufacturing	Feb-21	May-21	3 months
7	Thermal Testing	Jun-21	Jun-21	1 month
8	Prototype V2 Design and Manufacturing	Jun-21	Jul-21	2 months
9	Prototype V2 Testing	Jul-21	Jul-21	1 month
10	Final Impeller Design and Manufacturing	Jul-21	Aug-21	2 months
11	Final Prototype Design and Manufacturing	Jul-21	Aug-21	2 months
13	Dual Channel Nozzle Design and Manufacturing	Aug-21	Sep-21	2 months
14	Final Prototype Testing	Aug-21	Sep-21	2 months
15	Dual Channel Nozzle Testing	Sep-21	Sep-21	1 month

3.2 Software and Computational Resources

3.2.1 Requisite Software

A variety of engineering software was used throughout this study. Two different CAD packages were used to design the components of the propulsion module, both supplied by Autodesk. Autodesk offers free one-year licenses to all of its professional products and services to students and educators. These one-year licenses are also renewable as long as the user remains eligible. Autodesk Inventor Professional 2021 was the primary CAD package for designing and visualizing components and prototype assemblies. Fusion 360, Autodesk's cloud-based CAD

software, was used as a secondary CAD package due to its unique additive manufacturing-focused feature set. Propulsion module components that required 3D printed threads were first designed using Inventor Professional and then exported into Fusion 360. Unlike Inventor Professional, Fusion 360 allows the user to insert modeled threads onto components automatically. A specified tolerance can then be modified into the threads to ensure the threads operate correctly after printing.

Two different slicing software packages were used to prepare propulsion module CAD models for 3D printing. Both applications are free downloads for all users. Raise 3D Ideamaker was used to slice basic models that would not require support to be printed using the Raise 3D N2 printer. Ultimaker Cura was used to slice more complex models that require support to be printed using the Ultimaker S5 printer. The Calibration Shapes plugin was used with Cura to optimize various slice settings to improve print quality. Ultimaker also offers the cloud-based Digital Factory tool which was used to remotely monitor and manage various print jobs taking place on the Ultimaker S5 printers.

CFD simulation work was completed using the student edition of ANSYS 2020 R2. ANSYS offers a free, renewable one-year license to their student edition of ANSYS 2020 R2. ANSYS 2020 R2 includes a bundle of different engineering software accessible via the ANSYS Workbench application. ANSYS Workbench offers a graphical user interface that enables users to set up and manage an entire simulation project that utilizes multiple ANSYS programs in one environment[2]. Inventor components can be imported directly into ANSYS DesignModeler, one of the CAD packages provided by ANSYS, to prepare the geometry for meshing. The

geometry file is sent to ANSYS Mesh, where a suitable mesh is applied to the geometry and then exported to ANSYS Fluent, which served as the primary CFD simulation software for this study. Once the simulation is complete, the results are analyzed in the ANSYS Post-Processing application. Figure 3.1 below displays the CFD simulation project workflow used to analyze the final dual-channel nozzles.

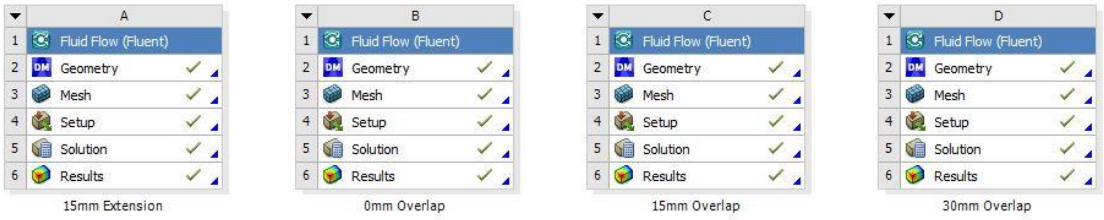

Figure 3.1: CFD Project Workflow of Final Dual Channel Nozzles

3.2.2 Computational Specifications

The machine used to execute the software listed above was a personal workstation computer. Relevant specifications of this workstation are listed in Table 3.2 below.

Table 3.2: Workstation Computer Specifications

CPU	AMD Ryzen 9 5900x 12-Core
GPU	GTX 1080ti 11 GB vRAM
Memory	32 GB (2 x 16 GB) DDR4-3600 CL16
Storage	2 TB NVME SSD, 500 GB SSD, 2 TB Hard Drive

CFD simulation, 3D slicing, and CAD rendering greatly benefit from high clock speed and high core count CPUs that can perform many operations per clock cycle[2]. The AMD Ryzen 9 5900X offers 12 total cores that can boost up to 4.8 GHz and is one of the best-performing CPUs on the market in terms of performance per

clock. This CPU significantly reduces CFD simulation time and slicing speed, enhancing efficiency and productivity.

The 11 GB of vRAM featured on the GTX 1080ti allows for smooth CAD performance when working on complex components and assemblies. The GPU's vRAM can also be utilized in ANSYS Fluent to aid in solving various CFD simulation equations, further decreasing simulation time.

This specific high-speed memory kit runs at 3600 mHz, which increases the data transfer rate between the memory and CPU, decreasing simulation and rendering times. Increased system memory allows larger, more complex models to be simulated via CFD and rendered in CAD/slicing applications. 32 GB of memory proved to be more than enough for this study and allowed for both simulation and CAD workloads to be completed simultaneously.

3.3 Project Locations

A majority of the research and design work was completed remotely due to COVID-19 related restrictions. Because of the pandemic physical distancing requirements, weekly Zoom meetings with Dr. Nassersharif have been conducted to maintain adequate communication throughout the project's duration. Prototyping and experimental testing of Prototype V1 and Prototype V2 took place at the University of Rhode Island's Fascitelli Center for Advanced Engineering facility in strict adherence to the university's COVID-19 health and safety guidelines. Final Prototype testing was conducted remotely for logistical purposes.

4. 3D Printing

4.1 Advantages of 3D Printing

3D printing was chosen as the primary manufacturing method for this project because of its rapid prototyping capabilities, cost benefits, and flexibility[1]. Designing a product from scratch requires multiple prototypes first to be manufactured to optimize and develop each component. Traditional manufacturing methods would be too time-consuming and costly to make sense for this study logistically. Rapid prototyping allows for components to be designed, manufactured, and tested in a short amount of time, dramatically increasing efficiency. If changes need to be made to the design after testing, the component can be reprinted immediately without adversely affecting the speed of the manufacturing process.

Manufacturing multiple prototypes can be quite costly using subtractive manufacturing methods that require parts to be carved out of a solid block of material, leading to an increase in wasted material. 3D printing, a type of additive manufacturing, builds the part from the ground up, resulting in far less wasted material[15]. Traditional manufacturing methods also require the use of expensive machines and skilled labor, further increasing the cost of the manufacturing process. Only a single machine and operator is required for 3D printing. Using more printers allows for more components to be manufactured at once, further increasing manufacturing efficiency.

Another advantage of 3D printing is the flexibility to manufacture almost any component that will fit within the printers build volume. With traditional

manufacturing processes, each new part or change in part design requires a new tool, mold, die, or jig to properly manufacture the part. When 3D printing, the part is fed into a slicing software where the print settings can be adjusted to suit the specific part without changing the physical machinery or equipment. Complex geometries that may be impossible to create using traditional manufacturing methods can be produced using 3D printing. Multiple materials can also be used to manufacture a single 3D printed part, enabling an array of colors, textures, mechanical properties, and supports to be mated together.

4.2 3D Printers Used

All of the propulsion module components (excluding mechanical components), as well as various other testing-related parts, were manufactured using the 3D printers available through the University of Rhode Island's Mechanical Engineering Makerspace. The Makerspace is home to seven FDM printers, including two Raise 3D N2 printers and five Ultimaker S5 printers. FDM printers work by extruding thermoplastic filament through a heated nozzle, melting the material, and applying the plastic layer by layer to a build platform[8]. FDM printers are the most widely used type of 3D printer at the consumer level due to their quick and low-cost prototyping capabilities.

4.2.1 Raise 3D N2

The Raise 3D N2 is a dual-extruder, direct-drive FDM 3D printer that features a fully enclosed build platform and a heated print bed, making this printer an excellent choice for printing with ABS or Nylon material. Ideamaker, also distributed by Raise 3D, serves as the primary slicing software for the Raise 3D N2. The standout

characteristic of the Raise 3D N2 is it's 12in x 12in x 12in build volume, allowing for large-scale models to be printed. The Raise 3D N2 and a schematic of its build volume are pictured in Figure 4.1 below.

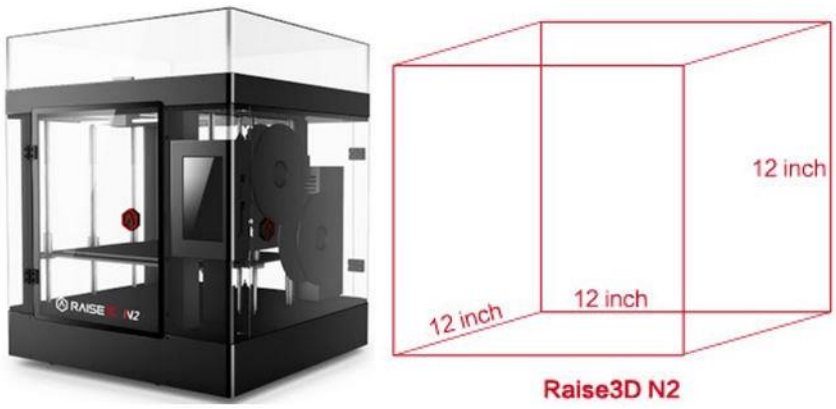

Figure 4.1: Raise 3D N2 and Build Volume

The Raise 3D N2 can print with a variety of 1.75mm diameter filament such as PLA, ABS, Nylon, and PETG. Both Raise 3D N2's in the Makerspace had dual-extruder setups with a 60mm primary nozzle and 80mm secondary nozzle. These larger nozzle diameters enhance the speed at which a part can be printed but decrease the resolution of the part. Because of this, the Raise 3D N2 printers were primarily used for early prototypes and basic components that could sacrifice resolution for decreased print times.

4.2.2 Ultimaker S5

The Ultimaker S5 is a dual-extruder, gear-driven FDM printer that is regarded as the class of the field amongst FDM printers, aimed towards professional applications. Cura, also distributed by Ultimaker, serves as the primary slicing software to use with the Ultimaker S5. The Ultimaker S5 features a slightly smaller

build volume than the Raise 3D N2 but makes up for it with its enhanced precision. Figure 4.2 displays the Ultimaker S5 and a schematic of its build volume.

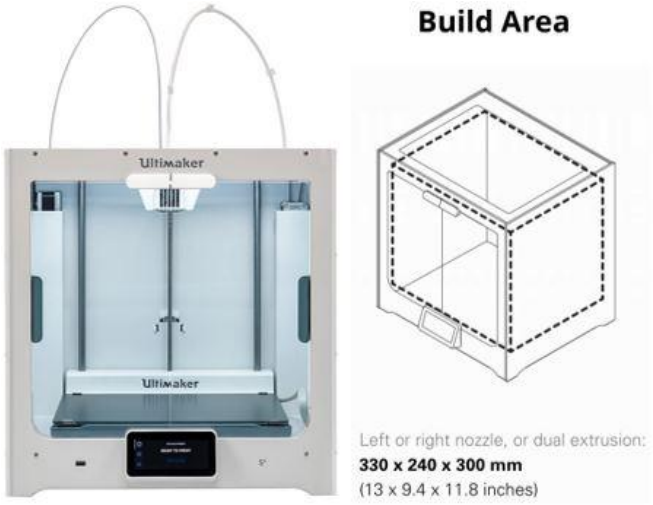

Figure 4.2: Ultimaker S5 and Build Volume

Similar to the Raise 3D N2, the Ultimaker S5 is capable of printing with a variety of different filaments. Unlike the Raise 3D however, the Ultimaker S5 requires 2.85mm diameter filament and can also print Ultimaker specific support materials, such as PVA Natural and Breakaway White. These Ultimaker specific materials allow for more complex models requiring support to be printed without decreasing the model's finish. On all five of the Ultimaker S5 printers, both nozzles are 40mm in diameter, enhancing print resolution and precision. All components from this project with complex geometries requiring support were printed using the Ultimaker S5 printers.

4.3 Materials Used

4.3.1 eSun PLA+

Selecting the optimal material for the construction of propulsion module components was crucial to ensure the module would operate in its given use cases. The material had to withstand underwater environmental factors, be strong enough to maintain rigidity under load, and possess good thermal characteristics that would allow the material to house electronics without failing. On top of this, it was also important to consider the price of the material to prioritize low manufacturing costs.

The initial plan was to print the propulsion module's structural components with PLA due to its strong mechanical characteristics, ease of printing, and low cost. These components would include the nozzle, primary waterjet channel and intake, motor mount/housing, and waterproof cap. The propulsion module's electronics housing, which holds the battery and control electronics, would then be printed using ABS filament with excellent durability and heat-resistant characteristics. The electronics housing would then be adhered to the motor mount/housing to combine the two components. Further along in the design process, it was decided that creating the motor mount/housing, electronics housing, intake, and primary waterjet channel as one component would be more beneficial to the overall design. Keeping the electronics housing separate would open the door for potential waterproofing issues at the connection point between the housing and module. Printing these parts together as one component would eliminate additional waterproofing issues while also increasing the module's structural integrity.

With this new design direction, a single material needed to be chosen to print all propulsion module parts. After further research, PLA+ was discovered to be the ideal choice of material for propulsion module components. Table 4.1 below displays some necessary physical specifications of eSun PLA+ filament.

Table 4.1: eSun PLA+ Physical Specifications

Filament	Density	Tensile Strength	Flexural Strength	Flexural Modulus	IZOD Impact Strength	Heat Distortion Temp
PLA+	1.25 g/cm^3	65 MPa	75 MPa	2102 MPa	8.5 KJ/m^2	52 C, 0.45 MPa

PLA+ retains many of the same benefits as standard PLA but features improved strength/thermal characteristics and is less prone to micro-cracks, increasing the water-resistance of the material. The additional thermal resistance provided by PLA+ allows this material to be used for the electronics housing without the risk of failure at increased temperatures. The materials impressive strength characteristics help improve the structural integrity of the propulsion module and decrease the potential for vibrations caused by the motor. PLA+ also offers a significantly smoother surface finish than standard PLA, reducing the coefficient of friction along the outer walls of printed components. eSun PLA+ costs $23.99 ± $0.99 for a 1kg 2.85mm filament spool. Compared to PLA filament spools of the same quantity, PLA+ is roughly $1.99 ± $0.99 more expensive.

PLA+ is also significantly more straightforward to print than ABS. ABS is prone to heavy warping and dimensional inaccuracies due to the high temperatures required to print the material. A fully enclosed print environment is also required to print ABS, which is only possible using the Raise 3D N2. The only complication with

printing PLA+ is the material's potential for oozing, which can quickly be addressed by optimizing temperature and retraction settings.

4.3.2 Ultimaker Breakaway White

Typically, 3D printed supports are built using the same material used to build the model. This method effectively builds high-strength supports, but the supports fully adhere to the model, requiring a tool to cut them off. This compromises the surface finish of the model and requires extensive post-processing to get the surface finish back to a desirable state.

Ultimaker Breakaway White is an Ultimaker specific material designed to negate these issues, creating high-strength supports that are easier to remove, leaving a smooth surface finish. Breakaway White shares similar print characteristics with PLA/PLA+, making the material easy to print. Instead of requiring a tool to remove supports, Breakaway white can be simply snapped off the model without leaving any blemishes on the model's surface. A smooth surface finish is essential for external propulsion module components to minimize frictional and drag losses. All of this project's printed components that required supports were printed using Breakaway White.

Breakaway White is significantly more expensive than traditional build filaments, coming in at $69.95 for a 750g filament spool. It was imperative to minimize the number of supports required on printed components to keep costs as low as possible.

5. Motor Testing

5.1 Provided Motors

The motor serves as the primary power generator for the waterjet propulsion module and must exhibit high-performance levels driving an impeller in an underwater environment. Peak underwater thrust performance does come at a cost, however. Typically, a higher-performing motor will require additional energy in the form of a larger, heavier battery to generate power over an extended period. This increase in battery size and mass will directly lead to an increase in the size and mass of the propulsion module. In addition to performance, it is also essential to consider the mass and dimensions of the provided motors. The motor is one of the dimensionally largest and heaviest mechanical components featured on the propulsion module. To incorporate a larger-sized motor, a larger mounting mechanism, and waterjet channel will need to be designed, increasing the dimensions and mass of the propulsion module. The optimal motor for this propulsion module must demonstrate the least amount of compromise between performance, size, and mass.

Dr. Nassersharif provided four different electric DC motors (three brushed, one brushless) to test and evaluate to reduce the overall project cost. On the following page, Figure 5.1 and Table 5.1 display the provided motors (from left to right in order of appearance in Table 5.1) and their dimensional specifications, respectively.

Figure 5.1: Provided Motors

Table 5.1: Dimensional Specifications of Provided Motors

Motor	Type	Mass (g)	Motor Diameter (mm)	Motor Length (mm)
DYS D3548-5	Brushless	156	35.00	48.00
RS 775 12V	Brushed	337	47.00	71.25
RS 887 18V	Brushed	470	48.00	68.25
KingClean 6238DC	Brushed	614	56.25	73.00

These four motors were experimentally tested, analyzed, and evaluated to determine the optimal choice of motor to serve as the primary thrust generator for this waterjet propulsion module.

5.2 Brushed Motors

The RS775 12V, RS887 18V, and KingClean 6238DC are all examples of brushed DC motors. All DC motors use wound coils of wire to create a magnetic field. For brushed motors, their coils are a part of the motor's subassembly called the rotor and are typically wound around an iron core. The coils are free to rotate to move a driveshaft. The exterior casing of the motor, known as the stator, is fixed due to the presence of a stationary magnetic field created by permanent magnets positioned on the inside wall of the stator. The rotor's magnetic field needs to rotate so that its field

attracts and repels the fixed field of the stator to create torque and spin the rotor continuously. A sliding electrical switch, consisting of a mechanical commutator mounted to the rotor and fixed brushes mounted to the stator, is used to make the magnetic field rotate. The commutator constantly switches different sets of rotor windings on and off as the rotor turns, causing the coils on the rotor to be attracted and repelled to the permanent magnets on the stator, spinning the rotor. Figure 5.2 is a schematic illustrating the key components found within a brushed DC motor. Figure 5.3 displays the inner workings of an actual brushed motor.

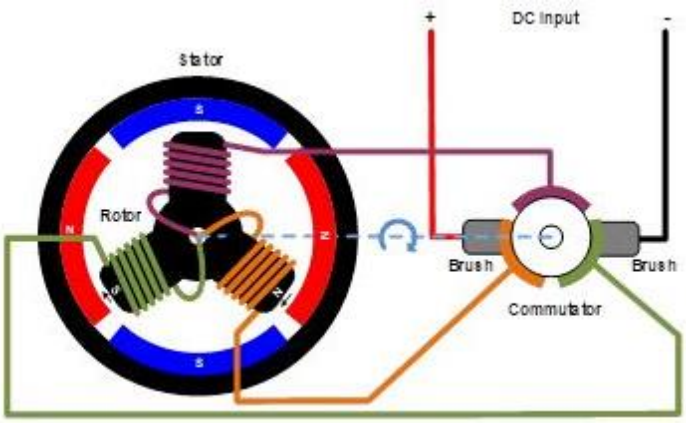

Figure 5.2: Brushed DC Motor Components[4]

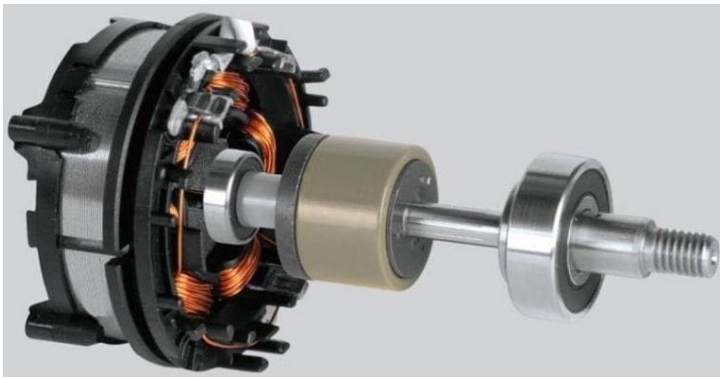

Figure 5.3: Inner Workings of Brushed DC Motor[3]

DC voltage is applied across the brushes, passing a current through the rotor windings, energizing the coils, and allowing the motor to spin. A simple switch controlling the DC voltage can turn the motor on and off. Speed, torque, and direction can be controlled using an H-bridge circuit composed of electronic switches such as transistors, IGBTs, or MOSTFETs. The H-bridge circuit allows voltage to be applied to the motor in either polarity to rotate the motor in both directions and modulate the pulse width of the switches to control motor speed and torque. If motor rotation is only required in one direction and speed and torque are not controlled, no control electronics are necessary to operate the motor.

Brushed motors have long been used in a various products such as children's toys, power tools, and home appliances due to their inexpensive production costs and simple control methods. Both the RS775 and RS887 are brushed motors that were previously used in lawn trimmers. The KingClean 6238DC served as a drive motor in a commercial washing machine.

5.3 Brushless Motors

The DYS D3548-5 motor was the only brushless motor provided for this study. Brushless DC motors operate using the same magnetic attraction and repulsion principle as their brushed counterparts but differ in construction. Unlike brushed motors, brushless motors do not feature a mechanical commutator and brushes to transfer current. Instead, the stator's magnetic field is rotated by using electronic communication with active control electronics.

Brushless motors can be configured as either “outrunner” motors or “inrunner” motors. For outrunner brushless motors, the rotor is the rotating case of the motor and has permanent magnets fixed to the inside wall, while the stator has windings and is housed within the rotor. The exact opposite is true of inrunner brushless motors, with the rotor located inside of the stator. The DYS D3548-5 is an example of an outrunner brushless motor. Figure 5.4 below is a cross-sectional rendering of an outrunner brushless motor.

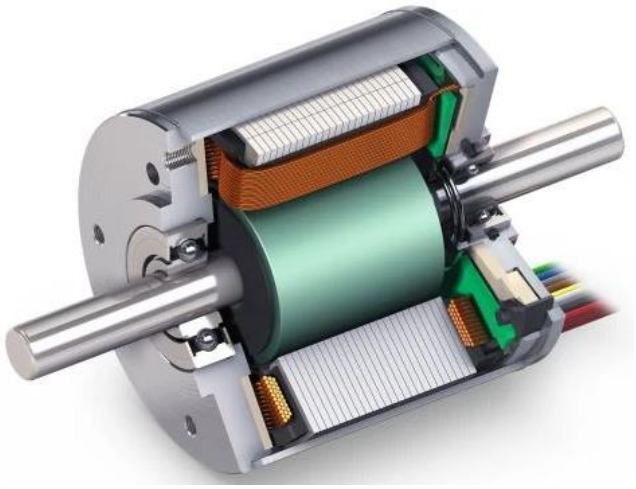

Figure 5.4: Cross-Sectional Rendering of Outrunner Brushless Motor[4]

The number of windings on the stator of the brushless motor is referred to as the number of phases. Most brushless motors are constructed with three phases like the DYS D3548-5 and are organized in a “delta configuration” connected by three wires. A different number of magnetic configurations or poles can be used with three-phase motors. A simple three-phase motor with a two-pole design will only have one pair of magnetic poles, one North and one South. Motors built with more poles require more permanent magnets on the rotor and more windings on the stator. The

DYS D3548-5 is a twelve-pole brushless motor. Figure 5.5 below is a schematic of a two-pole and four-pole brushless motor.

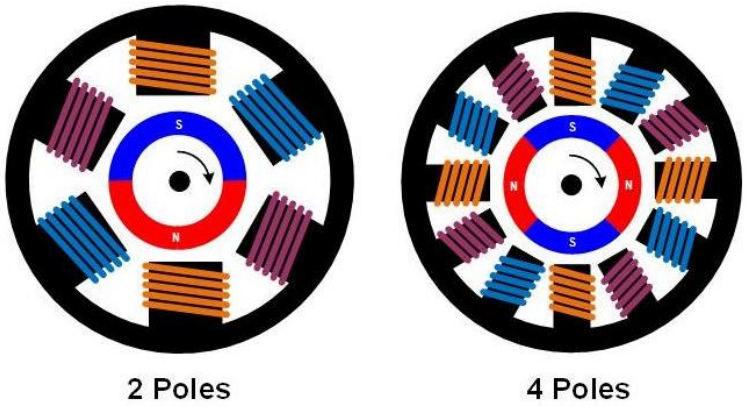

Figure 5.5: Two-Pole vs Four-Pole Brushless Motor[4]

Each phase of a brushless motor needs to be driven to either the input supply voltage or ground for a brushless motor to operate. This is accomplished by employing a half-bridge drive circuit for each phase consisting of two switches, bipolar transistors, IGBTs, or MOSFETs, depending on voltage and current requirements[18].

The motor's control electronics need to know the physical position of the rotor's magnets relative to the stator to rotate the magnetic field correctly. Hall sensors mounted on the stator obtain this information by picking up the rotor's magnetic field as the rotor turns. The control electronics can use this information to pass current through the windings on the stator in a specified sequence, causing the rotor to spin. Figure 5.6 on the following page is a schematic of this process for a two-pole brushless motor.

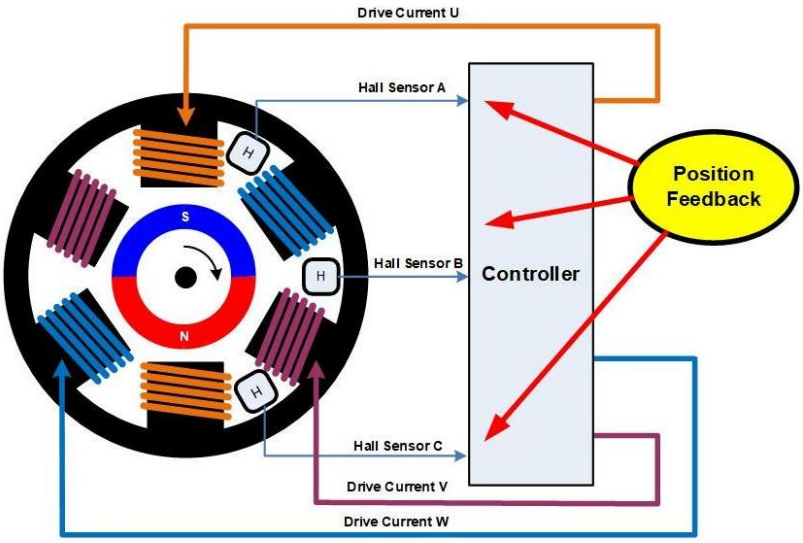

Figure 5.6: Control Electronics Positional Feedback Loop[4]

Several communication control methods can be used to drive a three-phase brushless motor. Trapezoidal communication is one of the most common and straightforward control methods connecting one phase to the ground, leaving one phase open, and driving the last phase to the supply voltage. The phase driven to the supply voltage can be pulse-width modulated to control speed and torque. Torque ripple can occur when employing the trapezoidal communication control method due to the abrupt switching of phases at each communication point. Other higher performance control methods, such as the Sine method, drive current through all three motor phases all the time, reducing torque ripple, acoustic noise, and vibration[18].

Due to their efficiency and advanced control methods, brushless motors have dominated the recreational remote-controlled vehicle industry. As brushless motor technology has improved, the automobile industry has begun rapidly adopting the technology to operate components that must operate continuously, such as pumps and

fans. The DYS D3548-5 is a popular choice of a brushless motor for medium-sized remote-controlled aircraft.

5.4 Brushed vs. Brushless Motors

There are a few key advantages and disadvantages of both brushed and brushless motors depending on the specific application they will be used for. Brushed motors are relatively inexpensive to manufacture compared to brushless motors due to the maturity of the technology. Brushless motors also require additional control electronics to operate the motor, further increasing the gap in overall cost between the two motors. Applications that do not require speed and torque control can opt to control a brushed motor using a simple on/off switch and still achieve the desired performance. This reduces the cost of the product and the complexity of implementing the motor as control electronics can prove to be faulty over time.

The primary advantage brushless motors have over brushed motors comes down to a fundamental difference in design. Brushed motors use brushes that must be in contact with the commutator to deliver an electrical charge which creates mechanical friction. Because this is an electrical contact, the contact cannot be lubricated, generating additional heat and wear. The mechanical wear on the brushes and commutator reduces the motor's lifetime, even with periodic maintenance. Brushless motors do not have any moving contacts. They therefore will not suffer from mechanical wear or additional heat generation, extending the lifetime of brushless motors while also allowing them to run cooler and more efficiently.

Their mechanical components also impact the rotational speed of brushed motors. At high speeds, the brush to commutator contact point can become erratic. This increases the likelihood of brush arcing occurring, leading to critical motor failures and increases in electrical noise. Brushed motors typically use a laminated iron core in the rotor that gives the motor sizeable rotational inertia, hindering the acceleration and deceleration capabilities of the motor.

Although additional control electronics do increase the overall cost and complexity of brushless motors, these advanced electronics allow for enhanced control of the motor's speed, torque, and direction. High-performance brushless motor control methods also significantly reduce the torque ripple that can occur when switching currents from one winding to another. For applications requiring specified control of the motor's performance, a brushless motor along with a controller would provide the best option.

When choosing a motor to be used in an underwater propulsion module, it is important to consider the waterproofing requirements for each type of motor. Most of the heat generation in brushed motors occurs in the coils located on the spinning rotor within the stator. Because of the location of the coils, there is not many ways in which the heat generated from the coils can be conducted outside of the motor, therefore requiring a good source of airflow to maintain optimal performance. The coils on a brushless motor are a part of the stationary stator, creating a direct conductive path from the coils to the outside of the motor, eliminating the need for airflow through the motor. This makes operating a brushless motor in a sealed, waterproof compartment much easier as an additional source of airflow will not need to be designed into the

compartment. Brushless motors can also operate wholly submerged underwater due to their lack of electrical contact. This does sacrifice the maximum lifespan of the motor but can be improved with proper bearing lubrication.

5.5 Motor Control and Power

5.5.1 Brushed Motor Power and Control

All three of the provided brushed motors were previously used in other products. Both the RS775 12V and RS887 18V are brushed motors that were previously used in lawn trimmers. The KingClean 6238DC served as a drive motor in a commercial washing machine. Specifications for the RS775 12V and RS887 18V, as shown in Table 5.2 below.

Table 5.2: RS775 12V/RS887 18V Specifications

Motor	Nominal Voltage (V)	Free Speed (RPM)	Unloaded Current (A)	Stall Current (A)	Max Power (W)	Stall Torque (Nm)
RS 775 12V	12	13050	2.7	97	246	0.78
RS 887 18V	18	23500	4.5	265	1180	1.90

The identification labels on the KingClean 6238DC had faded away, most likely due to extensive previous use. Because of this, it wasn't easy to locate the exact specifications for the motor. The KingClean 6238DC was eventually ruled out for testing primarily due to its substantial size and mass relative to the other motors. A motor of this size would dramatically increase the overall size and cost of the propulsion module.

A variable voltage DC power supply was used to power the motors to run the motors at their rated nominal voltage. The motor wires were connected directly to the

wires of the power supply. The on/off switch on the power supply served as the only method of controlling the brushed motors during testing.

5.5.2 Brushless Motor Power and Control

Before discussing how the specific components are used to control and power the DYS 3548-5 brushless motor during initial motor testing, it is helpful to first look at some of its specifications. Table 5.3 below displays some of the essential specifications of the DYS 3548-5 brushless motor that must be considered before determining how to drive the motor for testing.

Table 5.3: DYS 3548-5 Specifications

Specification	Value
KV (RPM/V)	900
Max Current (A)	70
Max Power (W)	770
Battery Cells	3-5
Battery Voltage (V)	11.1-18.5

The KV rating of a brushless motor refers to the constant velocity of the motor. KV is measured by the number of revolutions per minute that the motor turns when one volt is applied with no load attached to the motor. The maximum unloaded RPM a brushless motor will produce can be calculated using the motor's KV rating and the voltage rating of the battery. The DYS 3548-5 has a KV rating of 900 which is on the lower end for brushless motors used for recreational remote-controlled aircraft and drones. Typically, enthusiasts prefer smaller, high KV motors (2000 KV+) due to their weight savings and ability to make power at higher RPM for these applications.

Lower KV brushless motors tend to make more power and torque at lower RPM which would be beneficial for driving an underwater impeller[13].

The maximum current draw of the DYS 3548-5 is 70 A with a max power output of 770 W. This value represents the maximum current the motor draws under recommended load conditions. As this brushless motor is advertised to be used for remote-controlled aircraft, the recommended load conditions refer to the size of the propeller mounted to the motor. The factory maximum recommended propeller size for the DYS 3548-5 is 13 in x 7 in. Considering this application requires the motor to drive an impeller underwater, it is safe to assume that the actual maximum current draw of the motor exceeds the 70 A specification provided by the manufacturer. This is crucial to consider when selecting the control electronics for the motor.

Most recreational remote-controlled vehicles driven by brushless motors use LiPo batteries to power them. A LiPo battery is a form of rechargeable battery that is composed of a specific number of cells. The recommended number of LiPo battery cells for the DYS 3548-5 is 3-5 cells. The nominal voltage of a LiPo battery cell is 3.7 V. Multiplying this number by the number of cells in the battery gives the total advertised LiPo battery voltage. Considering the recommended 3-5 cell count, the recommended LiPo battery voltage for the DYS 3548-5 is 11.1-18.5 V.

With these specifications known, the control electronics and battery used to test the DYS 3548-5 brushless motor could then be selected. For efficiency, it was essential to construct the control electronics as straightforward as possible while also testing the motor properly. A suitable ESC, an electronic circuit that controls and

regulates the speed of a brushless motor, was the first component that needed to be selected. ESCs are rated based on the maximum amount of current they can supply to the motor at a given time. Although the manufacturer recommended a 70 A ESC based on the motor's max current draw, an 80 A ESC was selected for this application to allow for some head room if the motor overdraws its rated 70 A. The 80 A Electricparts.com RC ESC used for testing is pictured in Figure 5.7 below.

Figure 5.7: 80A Electricparts.com RC ESC

This ESC can deliver power from 2-6 cell LiPo batteries and comes with various programmable features and protections to ensure the brushless motor operates efficiently and safely. The ESC also features a 5.5 V UBEC to power additional receivers or external controllers without requiring an additional battery. A simple servo tester was connected to the UBEC wire to modulate the speed of the motor.

The Gens Ace 5000 mAh 11.1 V 3S 25C LiPo battery, pictured in Figure 5.8, was chosen as the power supply for brushless motor testing. A three-cell 11.1 V battery with 5000 mAh of capacity provides plenty of power and performance to the brushless motor for multiple maximum thrust output tests without requiring a charge.

The maximum unloaded RPM a brushless motor will produce can be calculated using Equation 5.1.

$$RPM_{Max} = KV * V_{Battery} \qquad Eq.\ 5.1$$

KV is the KV rating of the motor, and $V_{Battery}$ is the battery's nominal voltage. With a 900 KV rating and 11.1 V nominal voltage, the DYS 3548-5's maximum unloaded RPM is 9990 RPM. When driving an impeller underwater, the maximum RPM the motor could achieve will be significantly lower due to the additional load generated by friction forces. LiPo batteries also feature a C Rating specification. C Rating is the measurement of the current in which a battery can be charged and discharged. The maximum current a battery can be charged and discharged can be calculated using Equation 5.2 below.

$$Current_{Max} = (C\ Rating) * Q \qquad Eq.\ 5.2$$

Q is the battery's rated capacity in amps. Considering the DYS 3548-5 has a max current output of 70 A, the battery powering the motor must deliver at least 70 A of current. With a C rating of 25 and a rated capacity of 5 A, the maximum current output of this specific battery is 125 A, safely above the maximum current output of the motor.

Figure 5.8: Gens Ace 5000mAh 11.1V 3S 25C LiPo Battery

5.6 Experimental Motor Housings

5.6.1 Brushed Motor Housing

Waterproof housings had to be designed to ensure the two brushed motors could be operated safely underwater. These housings would need to be waterproof and easily assembled/disassembled to increase testing efficiency. Initial motor testing was primarily focused on identifying the maximum thrust output that the motors could produce. These results could be achieved with minimal runtimes that will not thermally stress the motors. It was not imperative to incorporate a proper cooling solution into the housing's design.

Both the RS775 and RS887 are similar in geometry but differ slightly dimensionally. The similar geometries allowed for one general design concept to be used for both housings. CAD models of the brushed motor waterproof housing are shown in Figure 5.9 below.

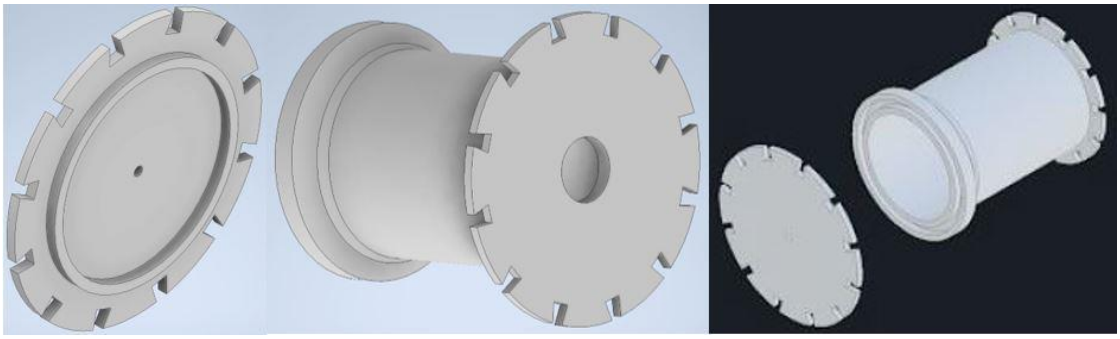

Figure 5.9: Brushed Motor Housing CAD Models

The waterproof housing consists of a cap and a cylindrical body. The cylindrical body was designed based on the length and diameter of the motor it would house. On the face of the cap facing the inside of the body is an extruded seal lip.

When the housing is assembled, this lip sits inside the silicone-coated seal channel located around the opening of the cylindrical body. The notches around the cap and bottom of the body are used to grip elastic bands that apply a force to the two housing components, compressing the lip into the silicone coated seal channel, creating a watertight seal. This design was used to create housings for both the RS775 and RS887, with the dimensions differing slightly to properly fit each motor. These housings were both 3D printed using PLA+. Figure 5.10 below displays the housings used for the RS775 and RS887 from left to right.

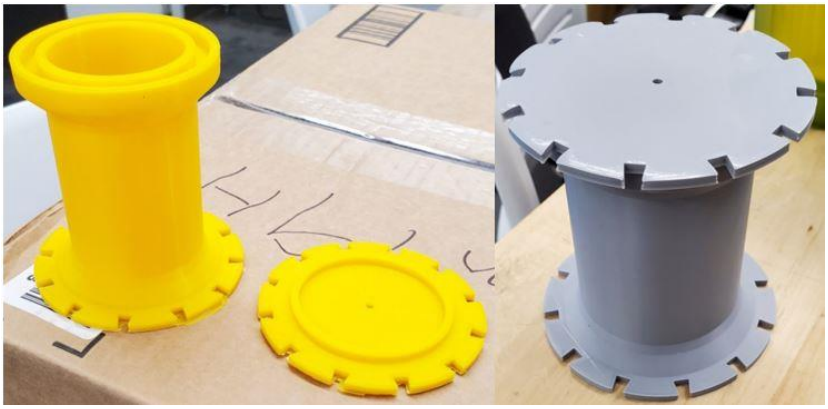

Figure 5.10: RS775 and RS887 Housings (Left to Right)

The 3mm hole in the middle of the cap was used to route the two motor wires through. Silicone was used to seal off this hole. The 11 mm hole at the bottom of the cylindrical body allows for a lubricated bearing to fit the housing. The 8 mm diameter motor shaft fits snuggly within the 8 mm inner diameter bearing, keeping the housing watertight. Both brushed motors have 8mm shaft diameters so both bearings were of the same specification. Figure 5.11 on the following page displays the bearing fit to the RS887 housing.

Figure 5.11: Bearing Mounted to RS887 Housing

5.6.2 Brushless Motor Housing

Brushless motors can be safely operated when submerged in water. Instead of creating a waterproof housing to test the DYS 3548-5 brushless motor, a cylindrical motor mount that would be completely exposed to the underwater environment was manufactured. Testing the brushless motor in this environment gave insight into its performance in these conditions and confirmed its durability. Figure 5.12 below displays a CAD model of the brushless motor test housing.

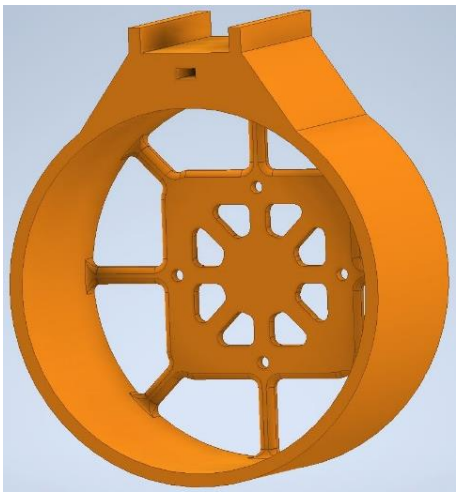

Figure 5.12: Brushless Motor Test Housing

The cylindrical housing has an inner diameter of 88mm, roughly twice the DYS 3548-5 diameter, to control the flow of turbulent vortices that shed off the brushless motor while it spins. Eight support pillars flank the square mount section of the housing, strengthening the mechanism while leaving open space for the motor wires to be fed through. A stainless-steel mounting bracket was supplied with the DYS 3548-5 to attach to the back of the motor with four screws. This bracket, displayed in Figure 5.13, could then be used to secure the motor to the housing with an additional four screws, washers, and nuts.

Figure 5.13: DYS 3548-5 Mounting Bracket

Like the brushed motor housings, this brushless motor housing was also 3D printed using PLA+ filament, providing adequate strength to hold the motor in place while spinning at high RPM without critical failure. On top of the housing is a rectangular seat designed to secure the housing to the lever arm of the test apparatus. A square hole was added to this section to loop a zip tie through the housing an around the lever arm. The housing assembled with the motor, bracket, and lever arm is shown in Figure 5.14 on the following page.

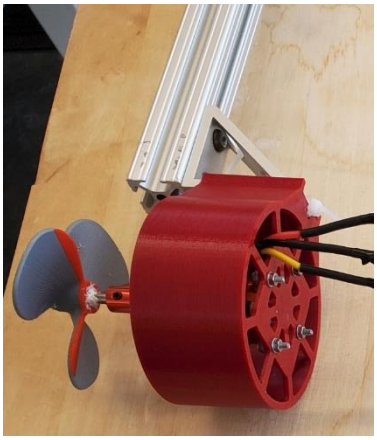

Figure 5.14: Brushless Motor Housing Assembly

5.7 Experimental Testing Apparatus

To properly test the underwater thrust performance of the provided motors, an experimental testing apparatus needed to be designed and constructed. This apparatus would have to be capable of withstanding the forces generated by the motor, accurately measuring thrust outputs, and fit in the MCE Capstone Lab without taking up too much space. The original concept sketch of the testing apparatus is displayed in Figure 5.15 below.

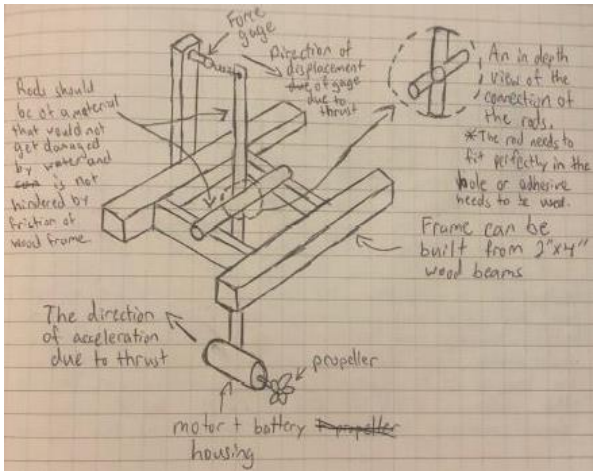

Figure 5.15: Testing Apparatus Concept Sketch

The rectangular frame of the apparatus was designed to sit on top of a 110-gallon plastic tub, constructed with 2 in x 4 in pieces of lumber screwed together. Two slots were cut using a rotary tool into the midpoint of the two short planks on the frame where a horizontal, lubricated metal rod is seated. This rod intersects with a vertical aluminum bar that can freely rotate about the center of the rod, serving as the lever arm of the apparatus. The motor housings were secured to the triangular anchor at the bottom of the lever arm with zip ties, while the top of the lever arm was attached to a Dr. Meter ES-PS01 force gauge using high strength electrical wire. This force gauge, shown in Figure 5.16, read to a tolerance of 0.01 lbs ± 0.005 and served as the primary output thrust data collector.

Figure 5.16: Dr. Meter ES-PS01 Force Gauge

The handle of the force gauge is mounted to two protruding vertical screws on top of the vertical 2 in x 4 in plank, which is secured to the rectangular base. With the apparatus fully assembled over the 110-gallon tub, as shown in Figure 5.17, the lever arm rests parallel to the vertical 2 in x 4 in plank, tangent to the rectangular base of the

apparatus. The electrical wire connecting the lever arm to the force gauge is set to a length that ensures no slack in the wire when zero applied force is present in the system.

Figure 5.17: Fully Assembled Experimental Testing Apparatus

The impeller, connected to the motor's driveshaft, faces outwards relative to the force gauge. When power is supplied to the motor, the impeller produces a thrust force in the direction opposite of the force gauge, represented by the Equation 5.3 below.

$$T = ma \qquad \textit{Eq. 5.3}$$

T is the thrust force created by the driven impeller, *m* is the total mass of the housing, motor, and impeller assembly, and *a* is the acceleration of the assembly. This thrust force creates a moment about the point of the lever arm connected to the horizontal rod, causing the top half of the rod to move in the direction of the thrust force. In

contrast, the housing assembly moves in the opposite direction, represented by Equation 5.4 on the following page.

$$M = -T(L - x) \qquad \textit{Eq. 5.4}$$

M is the moment about the point of the lever arm connected to the horizontal rod, *T* is the thrust force created by the driven impeller, *L* is the length of the lever arm and *x* is the distance from the point where the lever arm is connected to the horizontal rod to the point of the applied thrust.

The electrical wire connecting the lever arm to the force gauge will resist the motion of the lever arm, allowing the force gauge to output a thrust force reading. This thrust force reading is a slight underestimate of the actual thrust force produced by the driven impeller. Even with extensive sanding and lubrication, the contact surface between the lever arm and horizontal rod will still inevitably create a small amount of friction force opposing the direction of thrust force. The additional mass of the aluminum lever arm is minimal relative to the housing assembly but will also cause a slight reduction in the thrust force readout from the force gauge.

Due to the thrust force, the entire apparatus wants to move in the opposite direction of the thrust. Two wooden sawhorses were placed on either side of the back of the apparatus against the protruding sections of the rectangular frame, keeping the apparatus stationary. When testing the brushless motor, the battery, ESC, and servo controller needed to be secured to the frame of the apparatus to connect the circuit to the housing assembly. These electrical components were mounted to the rectangular

frame using strips of velcro. The testing apparatus, fully assembled for brushless motor testing, is shown in Figure 5.18 on the following page.

Figure 5.18: Testing Apparatus Assembled for Brushless Motor Testing

Large thrust force values create turbulent vortices inside of the 110-gallon tub, sending vibrations through the apparatus. These vibrations can lead to the ends of the horizontal rod separating from their slots, causing the apparatus to fail during testing. For the initial motor testing, the high-strength tape was placed over the ends of the rod to secure them in place. During prototype testing, the rods were secured in the slots using clamps when dealing with higher thrust values. The testing apparatus, fully assembled for final prototype testing, can be seen in Figure 5.19 below.

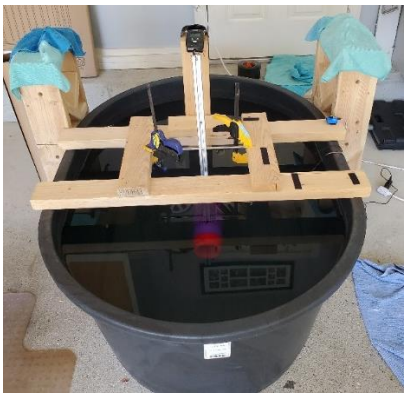

Figure 5.19: Testing Apparatus Assembled for Final Prototype Testing

5.8 Test Impellers

Both impellers used for motor testing share similar design parameters but differ in their total number of blades. Motor testing provided the opportunity to test the performance impact of the number of blades on an impeller. One impeller used for motor testing was designed with three blades, while the other used a four-blade design. Both impellers were tested with each motor to evaluate the performance differences between the two. The two impellers and their specifications can be viewed in Figure 5.20 and Table 5.4, respectively.

Table 5.4: Impeller Specifications

Diameter	Hub Length	Hub Diameter	Blade Pitch	Blade Height
84mm	24mm	14mm	50mm	35mm

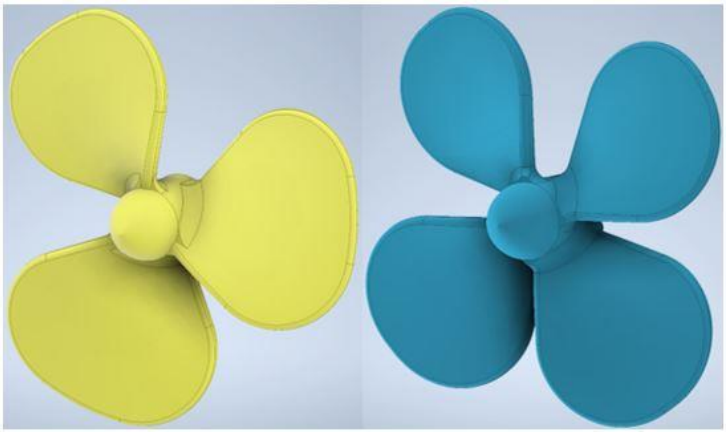

Figure 5.20: 3-Blade and 4-Blade Impellers

A CFD model was created before physical testing to simulate and compare the performance of these impellers in an underwater environment. The CFD model's geometry, mesh, and simulation parameters are organized into Tables 5.5, 5.6, and 5.7, respectively. The results from this simulation were then compared to the experimental results to verify the correlation between simulation and physical testing, identifying

potential issues with CFD setup parameters to improve simulation accuracy for further propulsion module development.

Table 5.5: Impeller CFD Model Geometry Parameters

Geometry Parameter	Value
Enclosure 1	Cylinder, Uniform 2.5mm
Enclosure 2	Box, 70mm (width) x 350mm (length)
Boolean 1	Subtract, Target = Fluid Domain, Tool = Rotor, Preserve
Boolean 2	Subtract, Target = Rotor, Tool = Impeller, No Preserve
Parts	Fluid Domain, Rotor

Table 5.6: Impeller CFD Model Mesh Parameters

Mesh Parameter	Value
Element Size (mm)	10.0
Max Element Size (mm)	10.0
Defeaturing	On
Capture Curvature	On
Capture Proximity	On
Smoothing	High
Inflation	10-Layer on Rotor
Face Meshing	Fluid Domain Faces, Mapped

Table 5.7: Impeller CFD Model Simulation Parameters

Simulation Parameter	Value
Solution	Transient
Model	k-ε, Scalable, Realizable
Cell Zone Conditions	Mesh Motion on Rotor, 1000 RPM
Boundary Conditions	2 Pressure-Outlets (Front/Back Fluid Domain)
Methods	Coupled, Least Squares, Second Order All
Convergence Criteria	10^{-3}
Time Step Size (s)	0.03
Number of Time Steps	100
Max Iterations/Time Step	80

The two impellers were simulated at a baseline rotational velocity of 1000 RPM over three seconds to compare the maximum flow velocity produced by each impeller. The Y-Z plane velocity contours for the 3-blade and 4-blade impeller at t = 3 seconds are displayed in Figures 5.21 and 5.22, respectively.

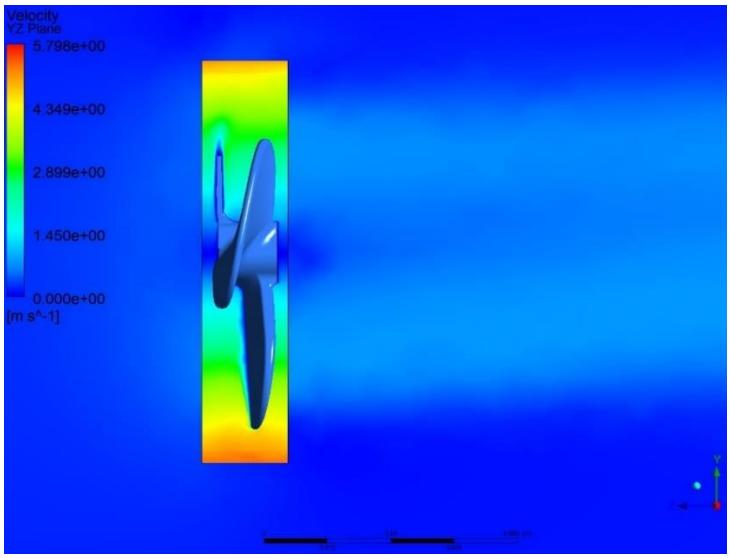

Figure 5.21: 3-Blade Impeller YZ-Plane Velocity Contour (t = 3s)

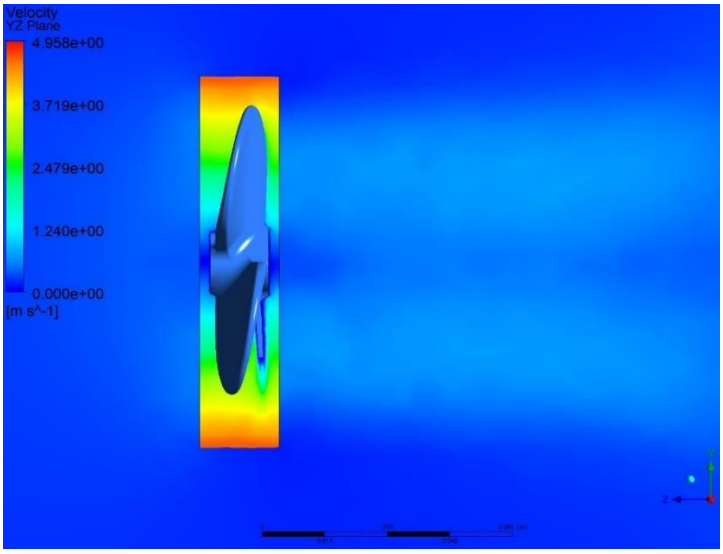

Figure 5.22: 4-Blade Impeller YZ-Plane Velocity Contour (t = 3s)

The maximum flow velocity produced by the 3-blade impeller was 5.798 m/s while the maximum flow velocity produced by the 4-blade impeller was 4.958 m/s. This result was expected as it was initially theorized that the additional surface area from adding a fourth blade would likely lead to additional frictional losses, causing a decrease in overall impeller performance. 4-blade impellers typically produce higher acceleration values but lower maximum speeds than 3-blade impellers.

The impellers were 3D printed using PLA+ filament in conjunction with Breakaway White support material to ensure the supports required to print the impellers could be easily removed without compromising the surface finish of the blades. A 5.5 mm diameter, 13 mm depth "D-connector," shown in Figure 5.23, was designed into the hub of the impeller to mount a 5mm diameter, 50 mm long driveshaft to the impeller.

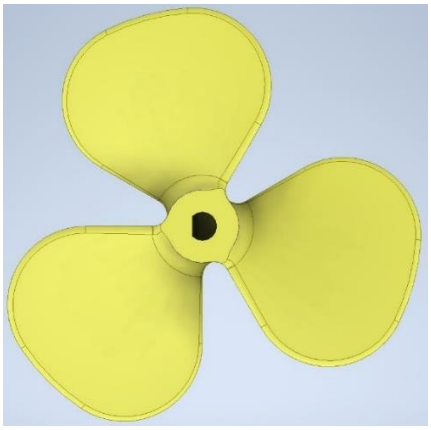

Figure 5.23: Impeller "D-Connector"

A 13 mm section of the driveshaft was ground down to resemble the geometry of the D-connector on the impeller. This section was then placed into the D-connector and secured in place using marine adhesive. The remaining 37 mm section of the

driveshaft protruding from the impeller was connected to a shaft coupler, connecting the impeller to the motor. The brushless motor required a 5 mm diameter to 5 mm diameter shaft coupler, while both brushed motors required a 5 mm diameter to 8 mm diameter shaft coupler. Figure 5.24 displays the brushless motor and three-blade impeller fully assembled for testing.

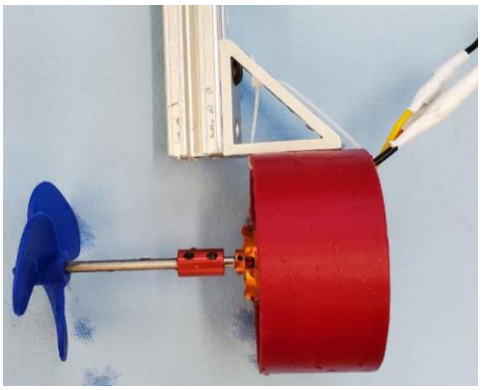

Figure 5.24: Brushless Motor and 3-Blade Impeller Testing Assembly

5.9 Motor Testing Results

All three motors were each tested once with the 3-blade impeller and once with the 4-blade impeller. The motors were set up to run at their maximum rated performance settings to determine their maximum thrust output. Maximum thrust output data for all three motors acquired during motor testing can be seen in Table 5.8.

Table 5.8: Motor Testing Max Thrust Output Data

Motor	Impeller	Max Thrust Output (lbf)
RS775	3-Blade	12.88
RS775	4-Blade	10.12
RS887	3-Blade	8.96
RS887	4-Blade	7.03
DYS 3548-5	3-Blade	11.78
DYS 3548-5	4-Blade	9.47

The RS775 brushed motor proved to be the top performer of the three motors, with a maximum thrust output of 12.88 lbf using the three-blade impeller. The DYS 3548-5 brushless motor using the three-blade impeller posted a maximum thrust output of 11.78 lbf, 8.54% lower than the RS775's output. The RS887 brushed motor only managed a maximum thrust output of 8.96 lbf, representing a 23.94% and 30.43% reduction in thrust output compared to the DYS 3548-5 and RS775, respectively. As expected from the preliminary impeller CFD simulations, the three-blade impeller proved to be the top-performing impeller for all three motors. The average maximum thrust output of the three-blade impeller was 26.37% greater than the average maximum thrust output of the four-blade impeller considering all three motors.

The RS887 was the heaviest of the three motors tested and ran erratically during testing, contributing to its low maximum thrust output. This motor was also significantly heavier than the others, putting the motor out of contention for this propulsion module. The RS775 and DYS 3548-5 posted comparable maximum thrust outputs, with the RS775 just edging the DYS 3548-5. Considering that the RS775 outperformed the DYS 3548-5 by only 9.34%, it was essential to look at the other inherent differences in the two motors before selecting the motor used for this propulsion module. Referring to Table 5.1, the RS775 is 116.03% heavier, 48.44% longer, and 34.29% wider than the DYS 3548-5. Although the RS775 was the marginally better performer, it is substantially heavier and larger than the DYS 3548-5. Using the RS775 for this propulsion module would increase the overall dimensions

and weight of the module due to the need for a larger battery and motor compartment, increasing overall costs.

For these reasons, it was decided that the DYS 3548-5 brushless motor would be the optimal choice of motor for the first propulsion module prototype. The DYS 3548-5 can deliver nearly the same performance as the RS775 in a significantly smaller package. The motor's reduction in size and weight could potentially lead to an increase in performance of the final propulsion module while also decreasing overall costs.

6. Propulsion Module Prototype V1

The primary goals of the first propulsion module prototype were to verify the waterjet system's functionality, optimize the module's performance using a traditional single-channel nozzle, and identify any significant issues to analyze and address in the following prototype. Although this prototype was not able to complete a successful underwater test, many important lessons were learned that improved the design of the propulsion module.

6.1 Electronic and Mechanical Components

The DYS 3548-5 brushless motor, 80 A Electricparts.com RC ESC, 3-blade impeller, and 5 mm to 5 mm shaft connector used for motor testing were all carried over to be used in Prototype V1. It was not intended for this prototype to have an integrated control system as it was focused on verifying mechanical functionality. Because of this, the servo tester used for motor testing was also carried over to control the speed of the brushless motor. A 300 mm extension cable was used to connect the servo tester, mounted on the testing apparatus, to the UBEC on the ESC, located inside the propulsion module.

The only mechanical component that differed from the components used for brushless motor testing was the 3-blade impeller's driveshaft. Instead of the 50 mm long 5 mm diameter driveshaft used for testing, a 60.15 mm long 5 mm diameter driveshaft was used for Prototype V1. The specific length of this driveshaft was derived from positioning the impeller directly in front of the propulsion module's intake.

The Gens Ace 5000 mAh 3S LiPo battery used for motor testing was ruled out for Prototype V1. At 381 g with 155 mm x 46 mm x 24 mm dimensions, this battery was determined to be too large in size and mass for this prototype. Instead, it was theorized that sacrificing battery capacity to reduce size and weight would improve overall propulsion module performance. The HOOVO 3200 mAh 11.1 V 3S 50C LiPo battery, pictured in Figure 6.1, was selected as the battery of choice for Prototype V1.

Figure 6.1: HOOVO 3S 11.1V 3200mAh 50C LiPo Battery

Featuring a C Rating of 50 and a 3200 mAh capacity, this battery can discharge 160 A of maximum current at a given time, safely above the 70 A maximum current output of the DYS 3548-5. Sacrificing 1800 mAh of capacity reduces the size and mass of the battery, with 131 mm x 44 mm x 17 mm dimensions and a mass of 216 g. This battery was shipped with a male T connector plug. An XT60 plug, rated for higher current loads relative to the T connector, was later soldered on instead to connect the battery to the ESC.

It was essential to estimate expected operational run times for the battery to address the reduction in battery capacity. A simple formula, denoted by Equation 6.1 on the following page, was used to calculate these estimations[7].

$$t_{run} = \left[\frac{\left(\frac{Q}{1000}\right)}{I_{load}}\right] * 60 \qquad \textit{Eq. 6.1}$$

Q is the battery's capacity in mAh, I_{load} is the current drawn from the battery by the motor and other equipment in amps, and t_{run} is the estimated operational run time in minutes. I_{load} can be calculated using Equation 6.2.

$$I_{load} = (I_{motor} * N_{motors}) + I_{other} \qquad \textit{Eq. 6.2}$$

I_{motor} is the current drawn from the motor in amps, N_{motors} is the number of motors used, and I_{other} is the current drawn from other equipment in amps. A single motor was used for this case, and the servo controller was the only additional current drawing equipment. The maximum current drawn from the servo controller is 15 mA. Considering the rated maximum current draw of the DYS 3548-5 is 70 A, the battery's maximum current load (I_{max}) is 70.015 A.

As the speed of the brushless motor can be altered using the servo controller, three different run time estimations were calculated to replicate the motor running at low (I_{load} = 30% I_{max}), medium (I_{load} = 65% I_{max}), and maximum (I_{load} = I_{max}) performance levels. Table 6.1 displays these estimations below.

Table 6.1: Operational Run Time Estimations

Performance Level	I_{load} **(A)**	t_{run}	$t_{run,\ 80\%}$
Low	21.005	9 min 8 sec	7 min 19 sec
Medium	45.510	4 min 13 sec	3 min 23 sec
Maximum	70.015	2 min 45 sec	2 min 12 sec

Two operational run times were calculated for each performance level: an expected operational run time if 100% of the battery's capacity is used (t_{run}), and an expected operational run time if 80% of the battery's capacity is used ($t_{run,\ 80\%}$). The 80 A ESC used for this propulsion module features a battery protection setting that limits the maximum capacity discharge allowed for the connected battery. LiPo batteries tend to degrade at a much quicker rate when fully discharged regularly. A battery discharge rule of 80% is regarded as a safe rule to follow to extend the life of LiPo batteries.

Even with the motor performance level set to low, the expected run time without the 80% discharge rule just misses the lower end of the 10-20 minute run time design specification. Despite this, the potential performance gained from the reduction in battery dimensions and mass was still thought to outweigh the downsides of decreased capacity. This theory was eventually disproved after further propulsion module development.

6.2 Propulsion Module Design

The primary propulsion module component, containing the waterjet channel, intake, electronics housing, and motor mount, was designed to be printed as a single part to improve the module's rigidity and decrease the potential for waterproofing issues. A CAD model of the primary propulsion module component and a cross-sectional view displaying the different sections within the component, can be viewed in Figures 6.2 and 6.3, respectively. An additional cross-sectional perspective of this component is provided in Figure 6.4.

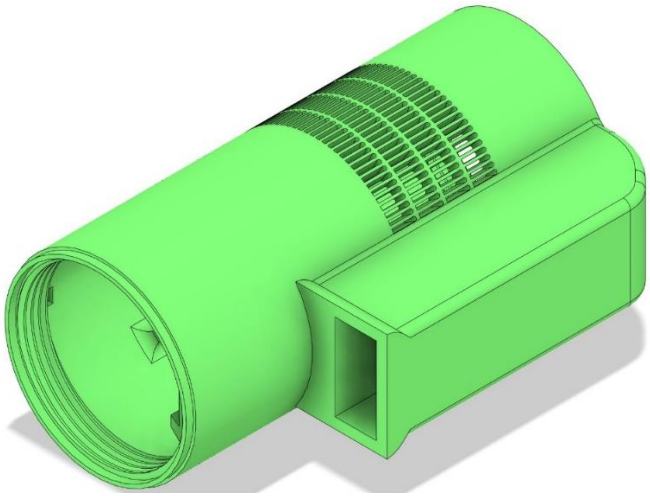

Figure 6.2: Prototype V1 Propulsion Module Component CAD Model

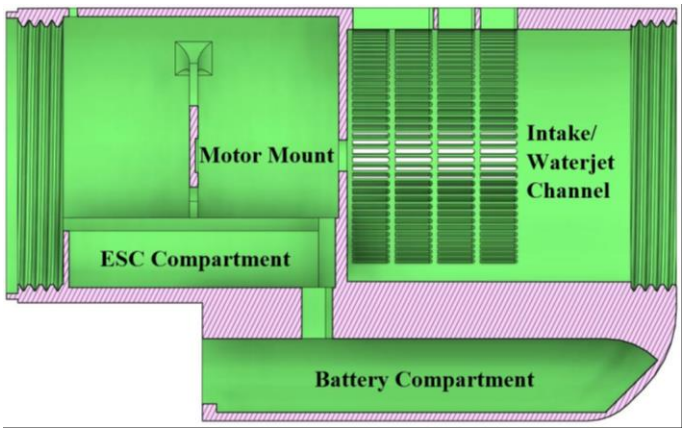

Figure 6.3: Prototype V1 Propulsion Module Component Labeled Cross-Section

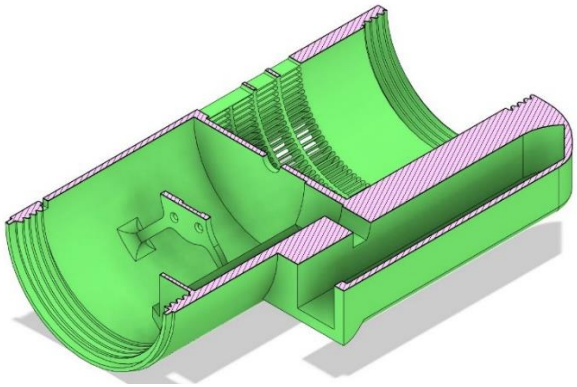

Figure 6.4: Prototype V1 Propulsion Module Component Cross-Section

6.2.1 Waterjet Channel and Intake

The waterjet channel, which houses the impeller and driveshaft assembly, was the first component of Prototype V1 to be designed. A cylindrical geometry was selected for the waterjet channel to minimize the drag coefficient of the module and increase impeller efficiency. The impeller/driveshaft assembly is located within the waterjet channel, with the driveshaft protruding from the 3 mm thick wall separating the electronics housing from the waterjet channel. Dimensional specifications for the waterjet channel are organized in Table 6.2 below.

Table 6.2: Prototype V1 Waterjet Channel Dimensional Specifications

Length (mm)	116.00
Outer Diameter (mm)	104.00
Inner Diameter (mm)	89.00
Cavity Volume (mm^3)	721652.11

The inner diameter of the channel was dependent on the diameter of the 3-blade impeller. With a channel inner diameter of 89 mm, the 84 mm diameter 3-blade impeller was granted 2.5 mm of clearance between its blade tips and the channel's inner wall. 2.5 mm was determined to be the optimal amount of clearance for the best impeller performance based on the CFD study mentioned in section 5.8. An outer diameter for the channel was set to 104 mm, creating a channel wall thickness of 7.5 mm. A 7.5 mm wall thickness, printed at 20% infill, provided adequate strength and allowed two 16 mm long M95 x 4 interior threads to be printed at either end of the module without reducing wall thickness below 4 mm.

The intake was designed to resemble a mesh-like geometry using four rows of individual slits. This mesh-like geometry allows fluid to flow smoothly into the waterjet channel and acts as a filter. Larger underwater debris, such as seaweed or stones, would not be able to enter the waterjet channel and compromise any of the module's components. Intake specifications and a sketch of the geometry are displayed in Table 6.3 and Figure 6.5, respectively.

Table 6.3: Prototype V1 Intake Specifications

Intake Length (mm)	58
Number of Rows	4
Slits Per Row	81
Total Number of Slits	324
Slit Surface Area (mm^2)	25.571
Total Intake Surface Area (mm^2)	8284.938
Slit Volume (mm^3)	191.781
Total Intake Volume (mm^3)	62137.035

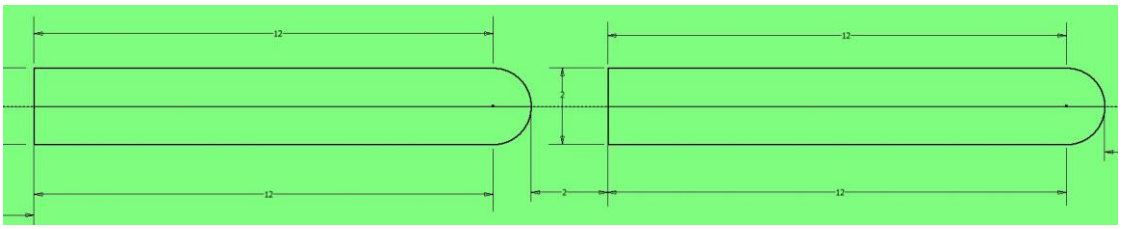

Figure 6.5: Prototype V1 Intake Sketch

Each slit consists of a 12 mm x 2 mm rectangular base with a 1 mm radius circular top for a total length of 13 mm. The propulsion module component was printed with the rectangular base of the slits facing the build plate with the circular top as an overhang. The intake was printed without any supports. When the propulsion module moves forward, the circular section of the intake faces the direction of fluid flow, reducing drag and increasing the amount of fluid entering the waterjet channel.

It was important to maximize the number of slits featured on the intake without compromising the module's structural integrity. After some experimentation, it was determined that the minimum 3D printed PLA+ wall thickness that would provide acceptable strength and stability was 1.3 mm. This, along with the location of the battery compartment, limited the maximum number of slits per row to 81, with a 1.335 mm wall between each slit. A 2 mm wall separated each row of slits to improve printability. Located on the top of the intake is a single 2.85 mm wide, 28.425 mm long slit, positioned closest to the wall separating the waterjet channel from the electronics housing. This slit was added to the intake to feed a hex key through the slit and tighten the set screws on the shaft connector.

The length of the intake determined the maximum number of rows that could be featured on the intake. Increasing the number of intake rows increases the total volume of the intake, allowing for more fluid to enter the channel. However, lengthening the intake requires a longer impeller driveshaft, creating additional performance losses. A 58 mm intake length required a 60.15 mm driveshaft to locate the impeller directly in front of the intake. This appeared to be an acceptable trade-off at the time, favoring an increased intake volume for a slightly longer (relative to motor testing) driveshaft.

6.2.2 Motor Mount and ESC Compartment

Initial open-air testing of the DYS 3548-5 brushless motor and 80 A Electricparts.com RC ESC did not demonstrate any thermal concerns that would require any additional cooling solutions. Because of this, Prototype V1 was designed to house the motor and ESC in the same waterproof compartment. The motor mount

was designed to replicate the mounting bracket used for motor testing, allowing the motor to be screwed directly into the mount with four screws. This mount, flanked by four 5 mm wide by 3 mm thick rectangular support pillars, is located directly above the ESC compartment to simplify wire connections. The front and rear perspectives of the motor mount and ESC compartment are displayed in Figure 6.6 below.

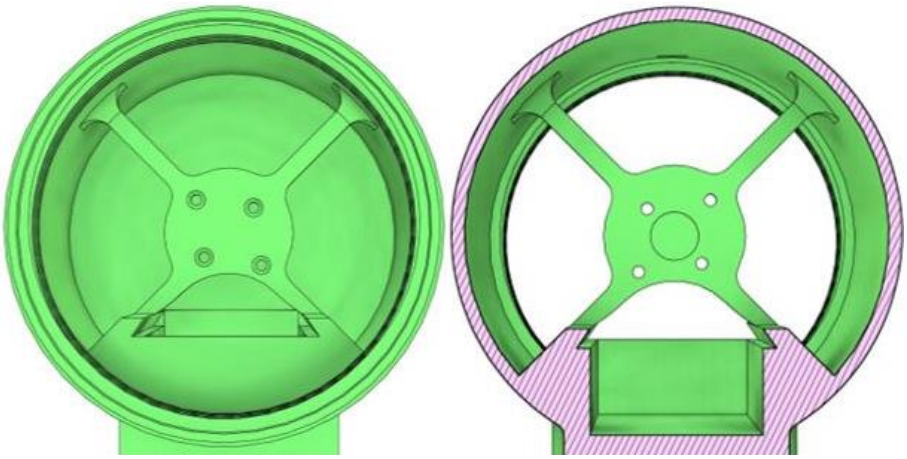

Figure 6.6: Prototype V1 Motor Mount and ESC Compartment

The motor had to fit between the side of the mount and the housing's inner wall to accommodate the assembly of the motor within the module. The back of the motor would then be placed on the bottom of the ESC compartment and angled upward to feed the motor's driveshaft through the bearing hole. A 24.5 mm ESC compartment depth was designed to ensure the motor could be angled correctly for this action to work. With the driveshaft protruding through the bearing hole, the rear of the motor could then be lifted upwards and secured to the mount.

Two dovetail rails were designed into the top of the ESC compartment to protect and secure it, where a sliding lid, displayed in Figure 6.7, would sit. The lid

features a rectangular hole to route the ESC's motor wires through. At 39 mm wide, the compartment provided 2 mm of clearance between the sides of the 35 mm wide ESC and compartment walls. With a length of 88 mm, the compartment was long enough to fit the ESC without compromising the position of its wires. A hole located at the bottom of the ESC compartment was designed to feed the female XT60 plug of the ESC into the battery compartment. The compartment wall closest to the wall separating the electronics housing from the waterjet channel features a circular design to minimize the number of 3D printed supports. A bird's-eye view of the ESC compartment can be viewed in Figure 6.8.

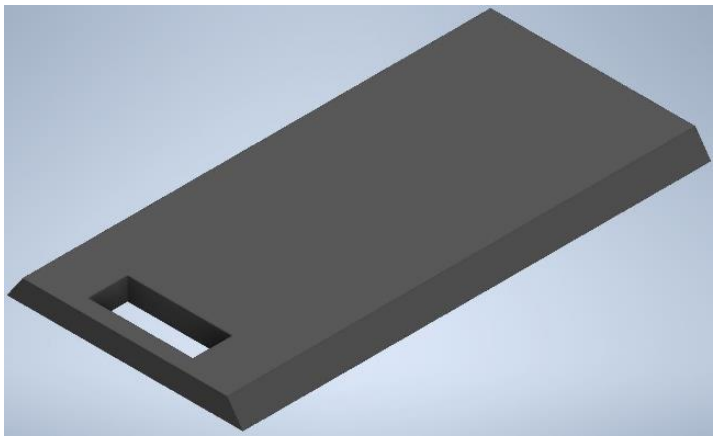

Figure 6.7: Prototype V1 ESC Compartment Lid

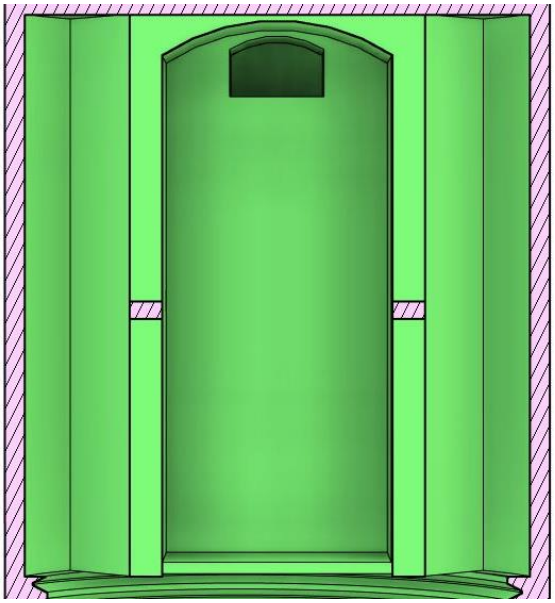

Figure 6.8: Prototype V1 ESC Compartment Bird's-Eye View

A small rectangular hole, pictured in Figure 6.9, was designed above the motor mount to route an extension cable into the module. This cable would connect the servo controller, located outside of the module, to the UBEC on the ESC inside of the module. Silicone was used to seal off the hole once the extension cable was routed through.

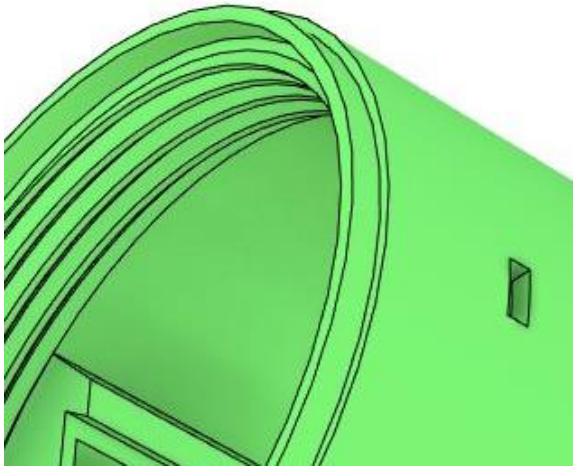

Figure 6.9: Prototype V1 ESC Extension Cable Hole

6.2.3 Battery Compartment

At 216 g, the LiPo battery was the heaviest component included in Prototype V1. The position of the battery compartment on the propulsion module had a significant impact on the location of the module's center of gravity. To ensure the propulsion module remained correctly oriented without flipping over when submerged, the module's center of gravity had to be as low as possible. Placing the battery compartment at the bottom of the module lowered the overall center of gravity, improving the module's stability.

LiPo batteries tend to expand under load at higher temperatures. The 137 mm long, 48 mm wide battery compartment was designed to fit the 132 mm long, 44 mm wide LiPo battery while also providing additional clearance to account for potential expansion. The height of the compartment was dependent on the connection between the battery and ESC. The ESC's female XT60 plug would be fed through the hole in the ESC compartment and into the battery compartment, requiring the connection between the battery ESC to occur on top of the battery. This connection introduced an additional 8 mm height on top of the 17 mm required to fit the battery. With a height of 26 mm, the battery and XT60 connection fit securely inside the battery compartment. The far wall of the battery compartment was revolved forward at a 45-degree angle to eliminate the need for 3D printed supports inside the battery compartment.

A 3D printed waterproof battery door was designed to insert and remove the battery from the propulsion module easily. This door featured a rotating hinge mechanism and a snap-fit lock to secure the door in place when closed. Both

cylindrical and angular snap-fit lock designs were developed and tested. Two battery door CAD models featuring these different lock designs are displayed in Figure 6.10 below.

Figure 6.10: Prototype V1 Battery Door CAD Models

After testing both designs, the angular locking mechanism proved to be the more durable and secure option. A lip and seal channel were designed into the walls of the battery door to prevent water from entering the battery compartment. When the door is locked shut, the 2 mm lip is compressed into the silicone-filled 3 mm deep seal channel, creating a watertight seal. Due to it's geometrical complexities, this battery door was printed as a separate component cemented to the module's battery compartment entrance. A 3 mm tall step located at the entrance of the battery compartment was added to prevent the battery from colliding with and potentially opening the battery door.

6.3 Waterproof Cap and Nozzle Design

6.3.1 Waterproof Cap

A waterproof cap was needed to be designed to protect the propulsion module's electronic components from the underwater environment. This cap would connect to the module's front, seal the electronics housing, and be easy to attach and remove. A low drag external geometry design was a priority as the cap served as the leading edge of the propulsion module. Figure 6.11 displays CAD renderings of the final waterproof cap designed for Prototype V1.

Figure 6.11: Prototype V1 Waterproof Cap CAD Model

Prototype V1's 58 mm long waterproof cap employed a spherical external geometry to minimize drag, with a maximum diameter of 104 mm to mirror the diameter of the propulsion module. The cap connects to the module using a modeled 16 mm long M95x4 thread, with the external thread applied to the cap and the internal thread applied to the module's front. A cylindrical 6 mm deep seal channel was added directly behind the external thread on the cap to make this connection watertight. This seal channel, filled with silicone, compresses into the cylindrical 4 mm lip on the propulsion module (see Figure 6.9) when the cap is screwed into place. A hollow, 85

mm diameter space surrounded by the external thread was left to attach lead ballast to the cap. Because the waterproof cap is located at the front of Prototype V1, adding ballast to the cap is a powerful way to move the module's center of gravity forward if necessary.

6.3.2 Nozzle V1

The primary nozzle-specific objective of Prototype V1 was to create, test, and optimize a traditional single-channel nozzle. Once this single-channel nozzle is optimized for maximizing the performance and efficiency of Prototype V1, the nozzle would serve as the basis for the development of the final dual-channel nozzle.

Five different nozzles were manufactured for Prototype V1 testing. These nozzles share a common design methodology but differ in outlet diameter. A CAD model and manufactured prototype of the 40 mm outlet diameter single-channel nozzle are displayed in Figure 6.12 on the following page.

Figure 6.12: Nozzle V1 40 mm Outlet Diameter CAD Model and Prototype

Similar to the waterproof cap, Nozzle V1 features a modeled 16 mm long M95x4 external thread that connects to the internal thread at the end of the waterjet channel on

the propulsion module. Specifications shared between the five nozzles are organized in Table 6.4. Table 6.5 displays the specifications that differ between the five nozzles.

Table 6.4: Nozzle V1 Shared Specifications

Inlet/Channel Diameter (mm)	Wall Thickness (mm)	Channel Length (mm)	Channel Volume (mm^3)
89	7.5	50	311056.943

Table 6.5: Nozzle V1 Different Specifications

Outlet Diameter (mm)	Tapered Section Length (mm)	Total Length (mm)	Tapered Section Volume (mm^3)	Total Volume (mm^3)
20	96.756	146.756	263048.112	574105.055
30	98.396	148.396	301662.698	612719.641
36	99.246	149.246	327465.616	638522.559
40	99.759	149.759	345756.897	656813.84
50	100.855	150.855	395242.451	706299.394

All five nozzles share the same 50 mm length from the start of the external thread to the start of the tapered section. This effectively increases the overall length of the 89 mm diameter waterjet channel to 150 mm. The length of each nozzle from the start of the tapered section to the outlet differs slightly. As the outlet diameter of the nozzle increases, the nozzle's total volume increases.

At the time, it was unclear how the different variations of Nozzle V1 would perform in physical testing. Theoretically, nozzles featuring smaller outlet diameters should yield increased thrust values due to increased fluid flow from nozzle inlet to outlet. However, this assumes that the mechanical waterjet components can provide the required power necessary to overcome the increase in pressure in nozzles with smaller outlet diameters. Fluid tends to flow in the direction where the least amount of resistance is present. If the pressure buildup in the nozzle exceeds the performance capabilities of the motor and impeller, the direction of fluid flow may reverse. Instead of fluid entering through the propulsion module intake and exiting through the nozzle

outlet, fluid enters through the nozzle outlet and exits through the propulsion module intake. Because of this, it was expected that the nozzles with larger diameter outlets would be the superior performers. The impact of nozzle length, taper angle, and volume was also unclear at the time and would need to be proved through physical testing.

Regardless, a basic CFD model was generated to display the theoretical maximum performance deltas between the five nozzles. All nozzles were simulated using a baseline inlet velocity of 1 m/s. Average outlet velocity and outlet thrust results are organized in Table 6.6 below.

Table 6.6: Nozzle V1 CFD Simulation Velocity and Thrust Results

Nozzle V1 Outlet Diameter	Avg. Outlet Velocity (m/s)	Outlet Thrust (lbf)
20mm	19.881	27.623
30mm	8.815	12.284
36mm	6.119	8.539
40mm	4.954	6.917
50mm	3.169	4.429

The results from this simulation were expected, with the smaller outlet diameter nozzles producing larger average outlet velocities and outlet thrust values. Interestingly, the 20 mm outlet diameter nozzle more than doubled the performance of the 30 mm outlet diameter nozzle. Nozzle performance appeared to increase linearly as the nozzle outlet diameter was decreased. These results did not carry over after physical testing due to concerns previously mentioned.

6.4 Prototype V1 Assembly

Before physically constructing Prototype V1, a CAD assembly was created to verify the fitment and layout of propulsion module components. Two isometric views and a cross-sectional view of the CAD assembly are shown in Figures 6.13 and 6.14, respectively.

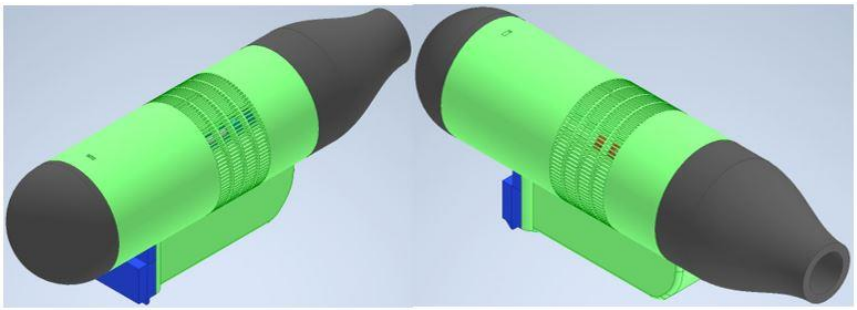

Figure 6.13: Prototype V1 CAD Assembly Isometric View

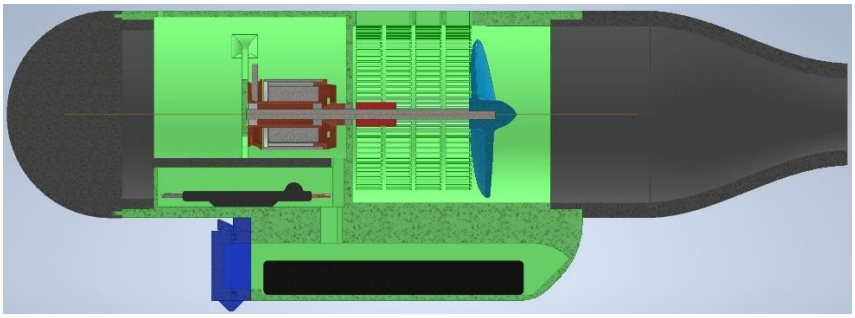

Figure 6.14: Prototype V1 CAD Assembly Cross-Sectional View

A breakdown of each component's mass in Prototype V1 can be found in Table 6.7. The module component, motor, waterproof cap, and battery were the heaviest components in the assembly.

Table 6.7: Prototype V1 Component Mass

Component	Mass (g)
Propulsion Module V1	466.50
Nozzle V1 36 mm	156.10
Waterproof Cap	180.10
Battery Door	57.70
ESC Lid	14.40
3-Blade Impeller	14.40
3200 mAh LiPo Battery	216.71
DYS 3548-5 Brushless Motor	169.03
80 A ESC	96.82
Driveshaft	9.00
Bearing	1.45
Shaft Connector	5.50
Total Mass (g)	1387.71

To physically assemble Prototype V1, the motor had to be the first component installed on the motor mount. With the motor installed, the bearing sealing off the waterjet channel from the electronics housing could be fixed around the motor's driveshaft. At this point, an installation motor run would be completed to verify that the motor is aligned correctly and spinning without resistance. Once this is confirmed, the battery door can be cemented to the entrance of the battery housing. Screwing on the waterproof cap completes the seal of the electronics compartment, allowing Prototype V1 to be submerged in the test tub to check for potential leaks. Assuming Prototype V1 passes these tests, the electronics could then be connected and installed to prepare the module for testing.

6.5 Critical Design Flaw

During the assembly process, a critical design flaw was discovered with Prototype V1. After installing the motor to the motor mount and securing the bearing,

an installation run of the motor was conducted to identify any potential issues. At start-up, the motor appeared to be operating as intended and handled throttle modulations without trouble. Roughly two minutes into the test, smoke appeared from inside the electronics housing, and the motor was shut down. Upon further inspection, the 3D printed motor mount failed due to thermal deformation, offsetting the motor's orientation and causing the driveshaft to rub against the bearing. A photo of the failed motor mount is displayed in Figure 6.15 below.

Figure 6.15: Prototype V1 Motor Mount Critical Failure

Although initial testing of the DYS 3548-5 brushless motor did not reveal any critical thermal issues when running in the open air, it was now apparent that the motor's operating temperature inside the electronics housing was too extreme for the PLA+ motor mount. The mount appeared structurally sound but thermally deformed at all four screw holes, with the worst failure occurring at the bottom right screw hole. In this configuration, the motor was in direct contact with the mount, with the screws

passing through the 3 mm mount and into the motor. The heat from the motor was conducted into the screws, allowing the heat to dissipate freely throughout the mount's interior.

Prototype V1 had to be scrapped following this failure, preventing the module from participating in any physical testing. A new method of mounting the motor within the propulsion module had to be conceptualized to eliminate the motor's thermal issues. The thermal issues presented by the motor also lead to a further investigation into the potential thermal limitations of the ESC and LiPo battery. The design of Prototype V1 did not include any additional methods of cooling electronic components. Further thermal testing of the ESC and battery had to be completed before designing Prototype V2.

7. Thermal Testing

After the critical thermal failure of Prototype V1 caused by the brushless motor, the thermal limitations of the ESC and LiPo battery needed to be investigated. The data collected from thermal testing was crucial to the development of Prototype V2. Understanding the thermal limitations of the ESC and battery allowed for cooling systems to be designed and implemented, ensuring the safe operation of electronic components.

7.1 Thermal Imaging

Initial thermal testing was conducted using the same testing apparatus setup as displayed in figure 5.18. The brushless motor was installed on the test mount and connected to the ESC on the apparatus using 16 AWG 300 mm extension wires. The battery was also secured to the apparatus to connect to the ESC easily. The Seek Thermal Compact thermal imaging camera, shown in Figure 7.1, collected ESC and LiPo battery temperature data. This camera was connected to a Galaxy S10 cellphone to view and record live thermal data.

Figure 7.1: Seek Thermal Compact Thermal Imaging Camera

The primary objective of the first round of thermal testing was to identify the operating temperatures of the ESC and LiPo battery under maximum load. The motor was run at full throttle for the duration of a single battery charge. Multiple full throttle tests were run to confirm the consistency of the temperature data.

The 80 A Electricparts.com ESC features thermal protection where the controller throttles down the motor to 20% if ESC temperatures ≥ 100 C are detected. The ESC continues to operate the motor at 20% throttle until either ESC temperatures drop below 80 C or the battery voltage protection limit is reached. A 3.2 V battery voltage protection limit was set for this test. During the full-throttle tests, the ESC began to thermally throttle after approximately 3 minutes of running and fully shut down the motor just under 4 minutes after reaching the battery voltage protection limit. Upon further inspection, the LiPo battery cell with the lowest voltage after testing was never lower than 3.65 V, demonstrating the conservative nature of the ESC's 3.2 V battery voltage protection limit.

The thermal imaging camera was fixed above the ESC and battery to monitor and record temperature data of the electronic components throughout each test. A collection of thermal images taken of the electronic components directly after motor shutdown are displayed in Figures 7.2, 7.3, and 7.4. Maximum temperature data collected from these thermal images are organized in Table 7.1.

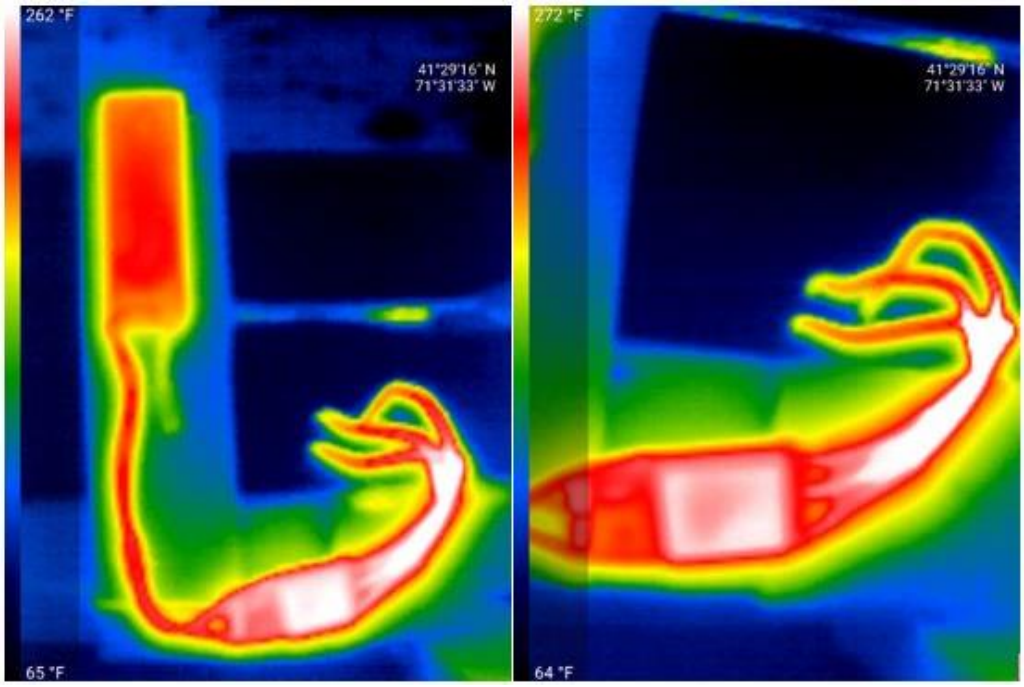

Figure 7.2: LiPo Battery, ESC, and Motor Wires Thermal Images

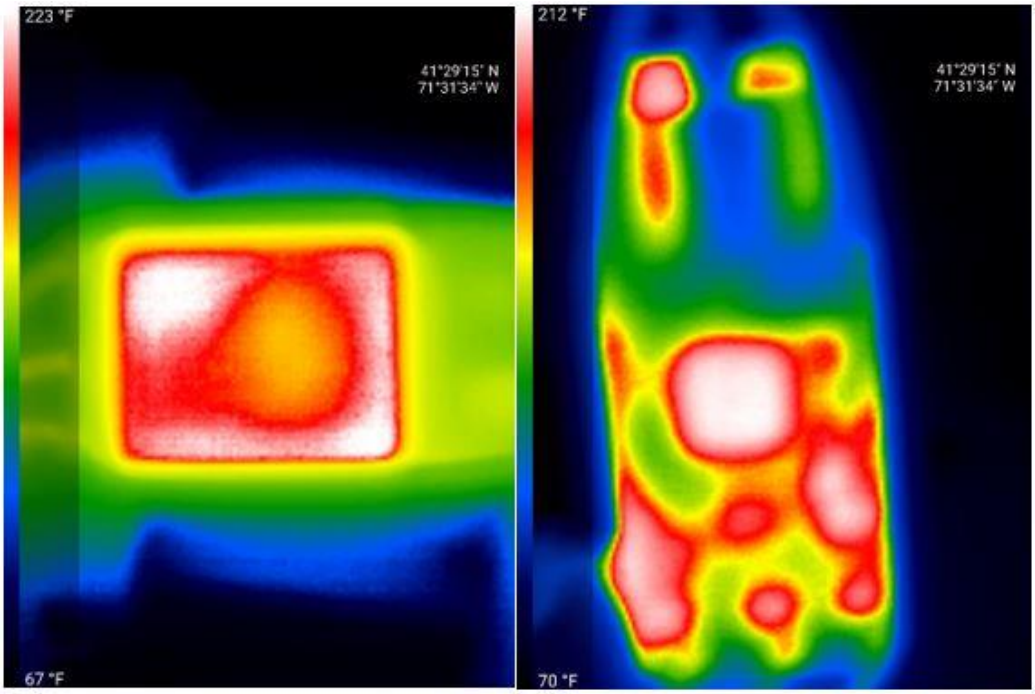

Figure 7.3: ESC Aluminum Heat Sink and MCU Side Thermal Images

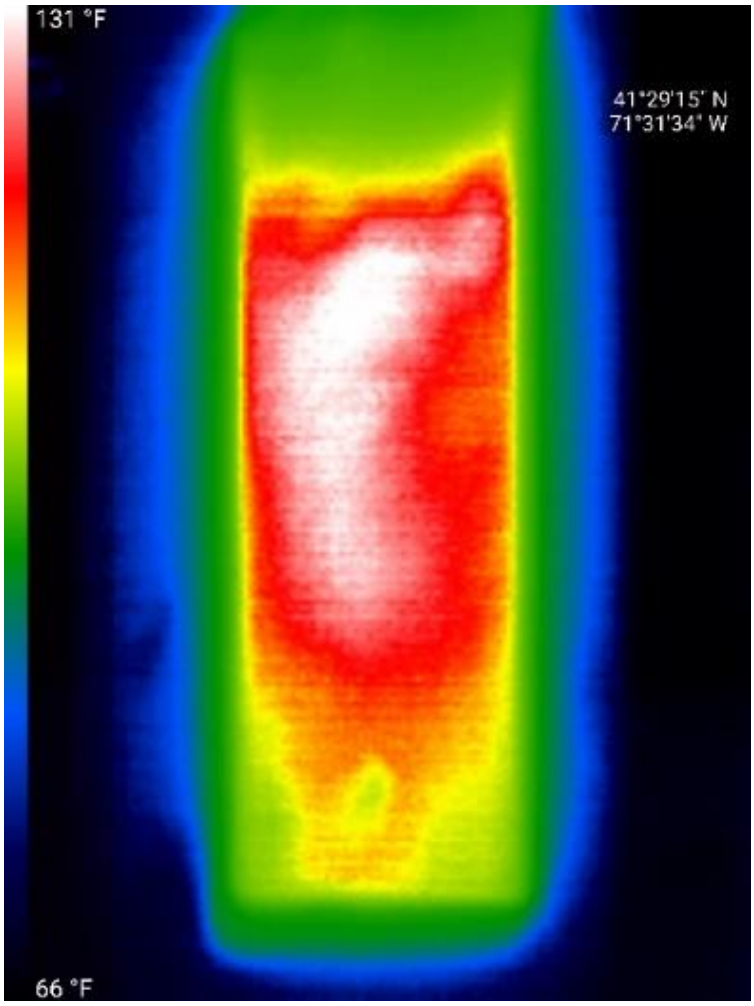

Figure 7.4: LiPo Battery Thermal Image

Table 7.1: ESC and LiPo Battery Temperature Data

Component	Max Temp (F)	Max Temp (C)
LiPo Battery	131	55
ESC (Heat Sink)	223	106
ESC (MCU)	212	100
Motor Wires	272	133

As expected, the maximum recorded temperatures of the ESC were both around the ESC's thermal protection limit of 100 C. The maximum temperature of the MCU side of the ESC, which faced against the wooden frame of the apparatus, was

100 C. Most of the heat buildup on this side of the ESC came directly from the centrally located MCU and MOSFETS along the sides of the ESC. The maximum temperature of the aluminum heat sink side of the ESC, which was fully exposed to open air, was 106 C spread evenly across the heat sink. The LiPo battery produced the lowest maximum temperature value of 55 C, located at the center of the battery. 70 C is generally regarded as the maximum safe operating temperature for LiPo batteries. The 16 AWG motor wire extension cables produced the highest maximum temperature value of 133 C. Most of the extension cable length was above the water line during testing. The heat buildup was spread evenly across the wires exposed to open air. The length of the extension cable below the water line remained at ambient water temperature.

7.2 Motor Wires and ESC Cooling Solutions

7.2.1 Motor Wires

The three 300 mm 16 AWG motor wire extension cables proved to be the component generating the most heat in the electrical circuit. These extension cables are connected to the 14 AWG motor wires on the ESC and brushless motor via 3.5 mm bullet connectors. Further research was conducted to identify recommended wire and connector specifications that could handle the 70 A of current draw from the DYS 3548-5 brushless motor. Table 7.2 on the following page displays recommended wire gauge based on the wire length and amperage load.

Table 7.2: Recommended Wire Gauge Based on Amperage/Length

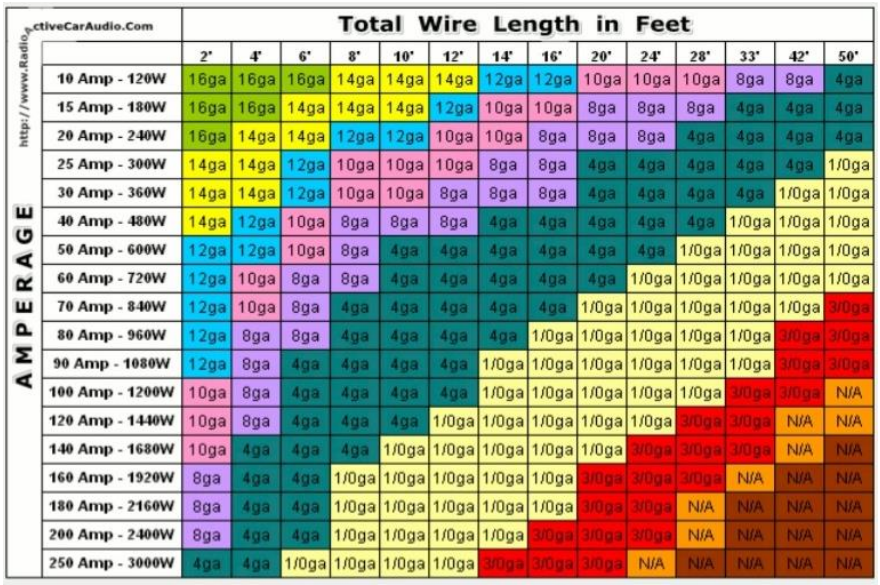

http://www.RadioactiveCarAudio.Com AMPERAGE	Total Wire Length in Feet													
	2'	4'	6'	8'	10'	12'	14'	16'	20'	24'	28'	33'	42'	50'
10 Amp - 120W	16ga	16ga	16ga	14ga	14ga	14ga	12ga	12ga	10ga	10ga	10ga	8ga	8ga	4ga
15 Amp - 180W	16ga	16ga	14ga	14ga	14ga	12ga	10ga	10ga	8ga	8ga	8ga	4ga	4ga	4ga
20 Amp - 240W	16ga	14ga	14ga	12ga	12ga	10ga	10ga	8ga	8ga	8ga	4ga	4ga	4ga	4ga
25 Amp - 300W	14ga	14ga	12ga	10ga	10ga	10ga	8ga	8ga	4ga	4ga	4ga	4ga	4ga	1/0ga
30 Amp - 360W	14ga	14ga	12ga	10ga	10ga	8ga	8ga	8ga	4ga	4ga	4ga	4ga	1/0ga	1/0ga
40 Amp - 480W	14ga	12ga	10ga	8ga	8ga	8ga	4ga	4ga	4ga	4ga	4ga	1/0ga	1/0ga	1/0ga
50 Amp - 600W	12ga	12ga	10ga	8ga	4ga	4ga	4ga	4ga	4ga	4ga	1/0ga	1/0ga	1/0ga	1/0ga
60 Amp - 720W	12ga	10ga	8ga	8ga	4ga	4ga	4ga	4ga	4ga	1/0ga	1/0ga	1/0ga	1/0ga	1/0ga
70 Amp - 840W	12ga	10ga	8ga	4ga	4ga	4ga	4ga	4ga	1/0ga	1/0ga	1/0ga	1/0ga	1/0ga	3/0ga
80 Amp - 960W	12ga	8ga	8ga	4ga	4ga	4ga	4ga	1/0ga	1/0ga	1/0ga	1/0ga	1/0ga	3/0ga	3/0ga
90 Amp - 1080W	12ga	8ga	4ga	4ga	4ga	4ga	1/0ga	1/0ga	1/0ga	1/0ga	1/0ga	1/0ga	3/0ga	3/0ga
100 Amp - 1200W	10ga	8ga	4ga	4ga	4ga	4ga	1/0ga	1/0ga	1/0ga	1/0ga	1/0ga	3/0ga	3/0ga	N/A
120 Amp - 1440W	10ga	8ga	4ga	4ga	4ga	1/0ga	1/0ga	1/0ga	1/0ga	1/0ga	3/0ga	3/0ga	N/A	N/A
140 Amp - 1680W	10ga	4ga	4ga	4ga	1/0ga	1/0ga	1/0ga	1/0ga	1/0ga	3/0ga	3/0ga	3/0ga	N/A	N/A
160 Amp - 1920W	8ga	4ga	4ga	1/0ga	1/0ga	1/0ga	1/0ga	1/0ga	3/0ga	3/0ga	3/0ga	N/A	N/A	N/A
180 Amp - 2160W	8ga	4ga	4ga	1/0ga	1/0ga	1/0ga	1/0ga	1/0ga	3/0ga	3/0ga	N/A	N/A	N/A	N/A
200 Amp - 2400W	8ga	4ga	4ga	1/0ga	1/0ga	1/0ga	1/0ga	3/0ga	3/0ga	3/0ga	N/A	N/A	N/A	N/A
250 Amp - 3000W	4ga	4ga	1/0ga	1/0ga	1/0ga	1/0ga	3/0ga	3/0ga	3/0ga	N/A	N/A	N/A	N/A	N/A

Larger amperage loads require larger gauge wire to decrease the amount of resistance in the system. Longer lengths of wire increase the resistance in the system, requiring a larger wire gauge to handle a specified amount of amperage. The more resistance present in the system, the more temperature buildup occurs in the system's electronic components. Increasing the wire gauge and decreasing the length of wire should decrease the maximum operating temperatures of the electronic components in the system.

The total length of wire required to connect the ESC to the brushless motor in this propulsion module will be well below the minimum 2 feet wire length displayed in Table 7.2. Because of this, the 2 feet wire length column was used as the reference. 16 AWG wire was recommended for amperage loads between 10 to 20 A, well below the 70 A rating of the DYS 3548-5. 14 AWG wire, which the ESC and DYS 3548-5 motor wires were shipped with, was rated for amperage loads of 25 to 40 A. 12 AWG

wire was recommended for amperage loads between 50 to 90 A, satisfying the requirements for the DYS 3548-5.

Larger diameter bullet connectors are capable of handling larger amperage loads. The 3.5 mm bullet connectors attached to the ESC and DYS 3548-5 motor wires were only rated for amperage loads of up to 40 A. 4.0 mm bullet connectors, rated for 70 A, appeared to be the better option to handle the 70 A current draw from the brushless motor.

Motor wire extension cables would not be necessary to connect the ESC and brushless motor inside the propulsion module. Instead, the initial plan was to replace the 14 AWG wire and 3.5 mm bullet connectors attached to the ESC and motor with 12 AWG wire and 4.0 mm bullet connectors. This would decrease the total resistance within the system, decreasing the maximum operating temperatures of the wires, ESC, brushless motor, and LiPo battery.

7.2.2 ESC

The 80 A Electricparts.com ESC produced the second-highest maximum operating temperatures of the electrical components tested but posed the most challenging thermal problem. At its thermal limit of 100 C, the ESC powers down the motor to 20% throttle. The propulsion module must operate at full throttle for the entire duration of a battery charge, requiring a cooling system capable of keeping the ESC below 100 C at all times.

This specific ESC is traditionally used for RC aircraft applications. In this usage case, the ESC would be cooled by the flow of air around the controller. When

the ESC is delivering its maximum amount of current to the motor, the aircraft would have a higher forward velocity, increasing the velocity of air flowing past the ESC. During this study's thermal testing, the ESC was operated in stationary open-air conditions with no air flow present, unsurprisingly thermally throttling 30 to 45 seconds before shut down. Although the ESC could not be tested in Prototype V1, the closed environment of the electronics housing would undoubtedly cause the ESC to throttle earlier than the open-air testing environment thermally.

Introducing an active cooling fan into the electronics housing of the propulsion module would be a complicated and costly endeavor that would increase the size and weight of the module. Instead, a concept for cooling the ESC using the water from the surrounding environment was developed. A window would be designed into the side of the propulsion module to mount a rectangular piece of aluminum sheet. One side of the aluminum sheet would be facing the inside of the electronics housing, with the other side exposed to the underwater environment. The ESC would be mounted inside the electronics housing such that the ESC's heat sink lay flat against the aluminum sheet.

Aluminum is a great conductor of heat with thermal conductivity of 237 $Wm^{-1}K^{-1}$. The aluminum sheet would work as a heat sink for the ESC, conducting heat from the ESC's heat sink. When the module is stationary, heat from the aluminum sheet would be transferred to the surrounding underwater environment via free convection. When the propulsion module has a forward velocity, water flows across the aluminum sheet, increasing cooling performance from the effects of forced

convection. A schematic of the heat transfer problem and a CAD model of this proposed cooling system are displayed in Figures 7.5 and 7.6, respectively.

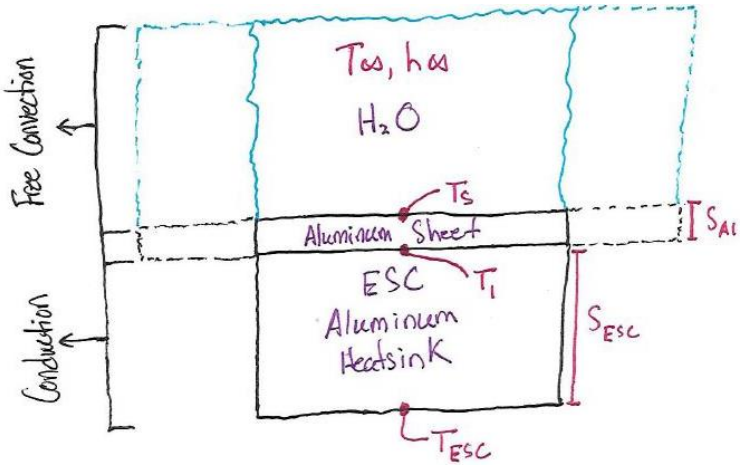

Figure 7.5: ESC Cooling System Heat Transfer Problem Schematic

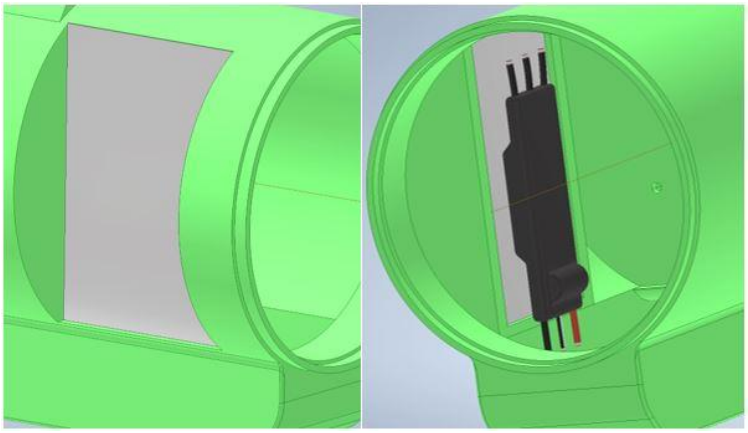

Figure 7.6: ESC Water Cooling System CAD Model

Extensive development and testing would have to have taken place for this concept to be successfully implemented on the propulsion module. Spending this amount of time designing a cooling system for an ESC that was not designed for underwater operation was not ideal for this project. Instead, the focus shifted towards researching other ESC options that would be better suited for this usage case.

The FLYCOLOR 150 A Waterproof ESC, pictured in Figure 7.7, was purchased to replace the 80 A Electricparts.com ESC. This waterproof ESC can operate when fully immersed in water. Copper heat pipes flanking both sides of the ESC provide cooling, cycling heat away from the ESC as water flows through the pipes.

Figure 7.7: FLYCOLOR 150A Waterproof ESC

The ESC features 10 AWG wires for both the motor and battery wires. 4.0 mm bullet connectors were soldered onto the motor wires further to decrease the amount of electrical resistance in the system. ESC's capable of delivering more considerable amounts of current are designed with improved cooling solutions to ensure safe operating temperatures. Capable of delivering 150 A of current, this ESC provided 80 A of current headroom for the 70 A rated DYS 3548-5 brushless motor. Instead of mounting the ESC inside of the propulsion module's electronics housing, this waterproof ESC could be externally mounted on the module to improve cooling performance.

7.3 LiPo Battery Cooling Solution Testing

7.3.1 LiPo Test Box Design

Prototype V1's battery housing design did not feature any built-in cooling solutions for the battery. Although the LiPo battery exhibited the lowest maximum operating temperature of 55 C, thermal testing did not replicate the sealed environment of Prototype V1's battery housing, which surely would increase operating temperatures. A cooling solution needed to be developed to ensure safe battery operating temperatures in Prototype V2.

Like the initial ESC cooling concept, the battery cooling concept would feature an aluminum sheet used as a heat transfer medium between the LiPo battery and the underwater environment. Ideally, this system would be able to keep the operating temperature of the LiPo battery below the recommended maximum safe operating temperature of 70 C. The dimensions of the aluminum sheet determined the rate at which heat can be transferred from the LiPo battery to the aluminum sheet and into the surrounding water. The heat produced by the LiPo battery would be conducted by the aluminum sheet and released into the surrounding water via forced or free convection, dependent on if the module has a forward velocity or not.

An experimental LiPo battery test box, displayed in Figure 7.8 on the following page, was designed to test the cooling performance of the aluminum sheet in a submerged environment.

Figure 7.8: LiPo Battery Test Housing CAD Model

The test box design replicated the sealed environment of the battery housing. A 146 mm by 54 mm window on one side of the box serves as the mounting point for the 0.5 mm thick aluminum sheet. A marine adhesive was applied to the 3 mm lips of the window to adhere the aluminum sheet to the test box. The LiPo battery lays flat against the aluminum sheet inside the 140 mm by 48 mm by 30 mm compartment, mirroring the dimensions of the battery housing. An upscaled version of the hinge mechanism from Prototype V1's battery door was used to open and close the test box. The test box was waterproofed using a lip and silicone-filled seal channel, locked in place using high-strength tape.

The connection between the battery and extension wires takes place inside the test box, with the XT60 connectors lying flat against the battery. A rectangular hole located at the top of the box was created to route battery extension wires and a thermometer through. This thermometer was secured to the center of the LiPo battery with aluminum tape to gather temperature data. The fully assembled battery test box is displayed in Figure 7.9 on the following page.

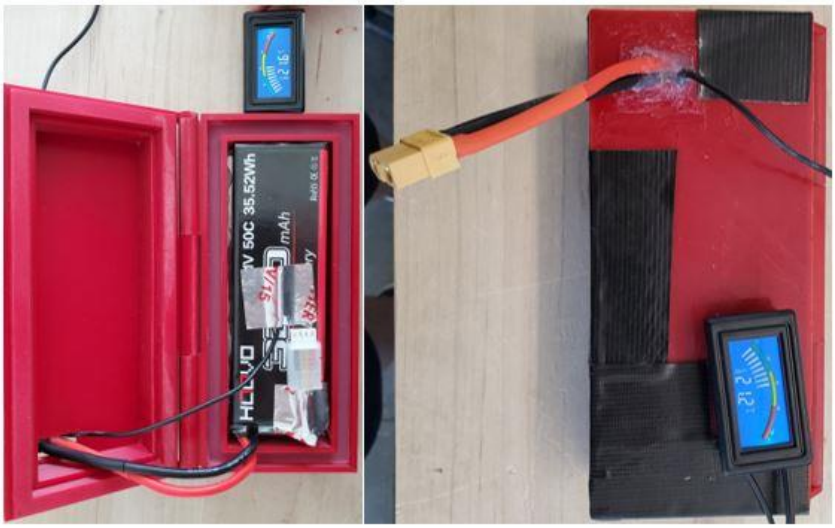

Figure 7.9: Fully Assembled LiPo Battery Test Box

7.3.2 LiPo Battery Thermal Testing

Three thermal tests were conducted to evaluate the performance of the aluminum sheet water cooling system. Each test was run for a complete battery discharge with the motor at full throttle. The FLYCOLOR 150 A Waterproof ESC was used for these tests. Rather than mounting the ESC to the testing apparatus, the new ESC was submerged in the 110-gallon tub to confirm its underwater capabilities. Two aluminum beams supported the battery test box at the bottom of the tub, with the aluminum sheet facing downward. Lead ballast located on top of the box prevented the box from resurfacing. A photo of the testing setup and battery thermal testing data are displayed in Figure 7.10 and Table 7.3, respectively, on the following page.

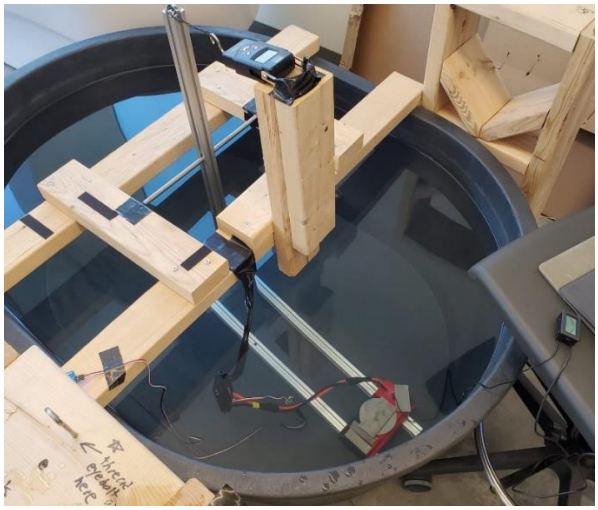

Figure 7.10: LiPo Battery Thermal Testing Setup

Table 7.3: LiPo Battery Thermal Testing Data

Test #	Initial Battery Temp (C)	Max Battery Temp (C)	Run Time
1	21.0	65.5	3 min 52 sec
2	21.6	68.7	3 min 54 sec
3	21.3	66.9	3 min 51 sec

The initial battery temperature was recorded directly after submerging the test box. After the motor shut down, the temperature of the LiPo battery continued to increase for approximately 30 seconds until reaching its maximum temperature. The average maximum battery temperature from the three tests was 67.03 C, just below the 70 C recommended limit. Following each test, an infrared thermometer was used to measure the temperature of the new ESC. All three ESC temperature readings were approximately the same as the ambient water temperature, confirming its cooling performance.

Crucially, the motor ran without thermally throttling for the entirety of all three tests, likely due to the new waterproof ESC. In the previous thermal tests where the battery was in an open-air environment, the maximum temperature the battery reached was 55 C. These tests were flawed, however, as the ESC thermally throttled after 3 minutes of operation. In the compact test box, the battery never reached dangerous temperatures despite operating under maximum load conditions for the entire run time, confirming the water-cooling performance of the aluminum sheet. This method of cooling would be carried forward to Prototype V2.

8. Propulsion Module Prototype V2

After the failure of Prototype V1, the primary goal for Prototype V2 was to create a functional propulsion module based on the lessons learned from the previous prototype and thermal testing. Prototype V2 would be used to optimize the performance of the waterjet channel using a traditional single-channel nozzle and serve as the reference for the Final Prototype.

8.1 Electronic and Mechanical Components

The DYS 3548-5 brushless motor, HOOVO 3200 mAh 11.1 V 3S 50C LiPo battery, 3-blade impeller, and 5 mm to 5 mm shaft connector were all carried over from Prototype V1 to be used in Prototype V2. The servo tester used for Prototype V1 was also carried over to control the speed of the brushless motor. A 300 mm extension cable was used to connect the servo tester, mounted on the testing apparatus, to the UBEC on the ESC, located inside the propulsion module. Only two components were changed from Prototype V1, one electronic and one mechanical. The FLYCOLOR 150 A Waterproof ESC replaced the 80 A Electricparts.com ESC, and a 29 mm driveshaft was used in place of the 60.15 mm driveshaft from Prototype V1.

8.2 Propulsion Module Design

Three fundamental design alterations were made to the propulsion module component of Prototype V2 to address the issues with Prototype V1. The mount for the DYS 3548-5 brushless motor was moved from inside of the electronics housing to the inside of the waterjet channel to reduce motor operating temperatures and prevent

motor mount failure. The new FLYCOLOR 150 A Waterproof ESC was implemented to the module, requiring the creation of a new external mounting mechanism. The battery compartment, which now featured the aluminum sheet cooling system, was integrated into the electronics housing, requiring a complete redesign of this section. These design changes, along with a few other minor alterations, proved to be successful, allowing Prototype V2 to function correctly and be physically tested. A CAD model of Prototype V2's propulsion module component and a cross-sectional view with labeled sections are displayed in Figures 8.1 and 8.2, respectively.

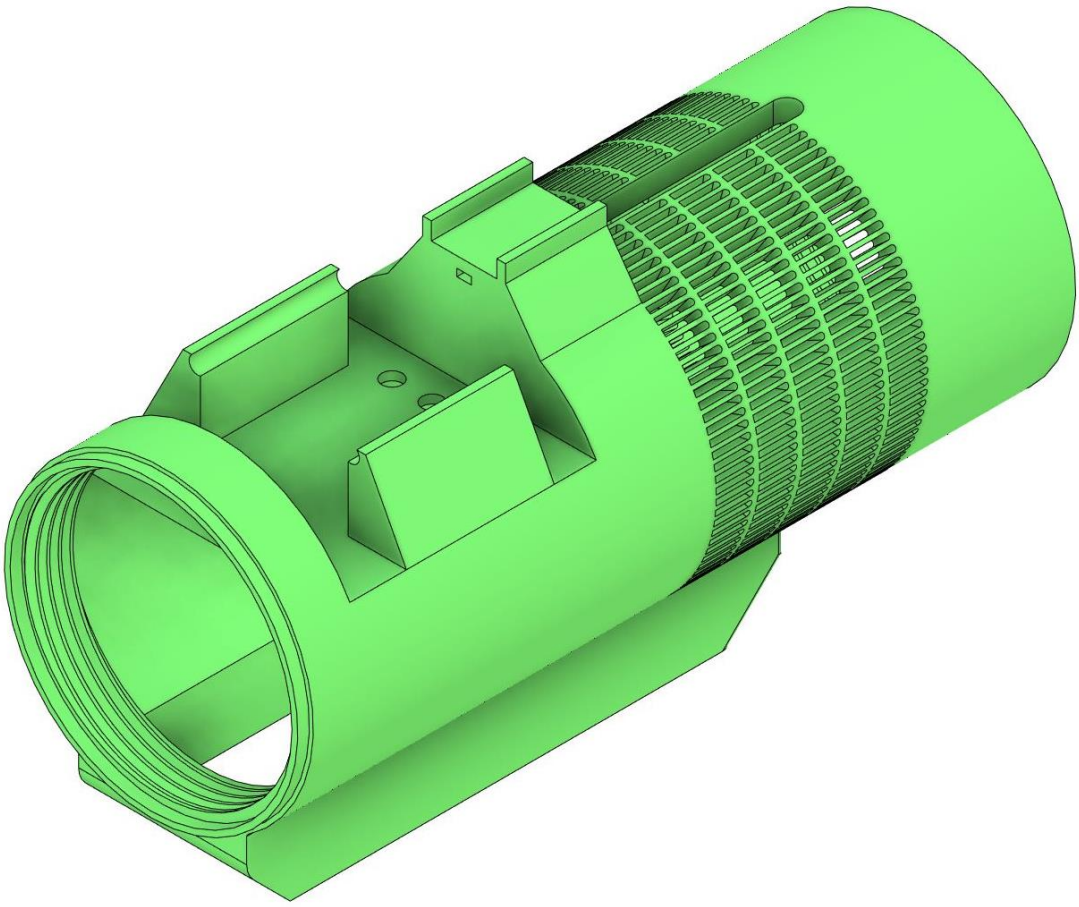

Figure 8.1: Prototype V2 Propulsion Module Component CAD Model

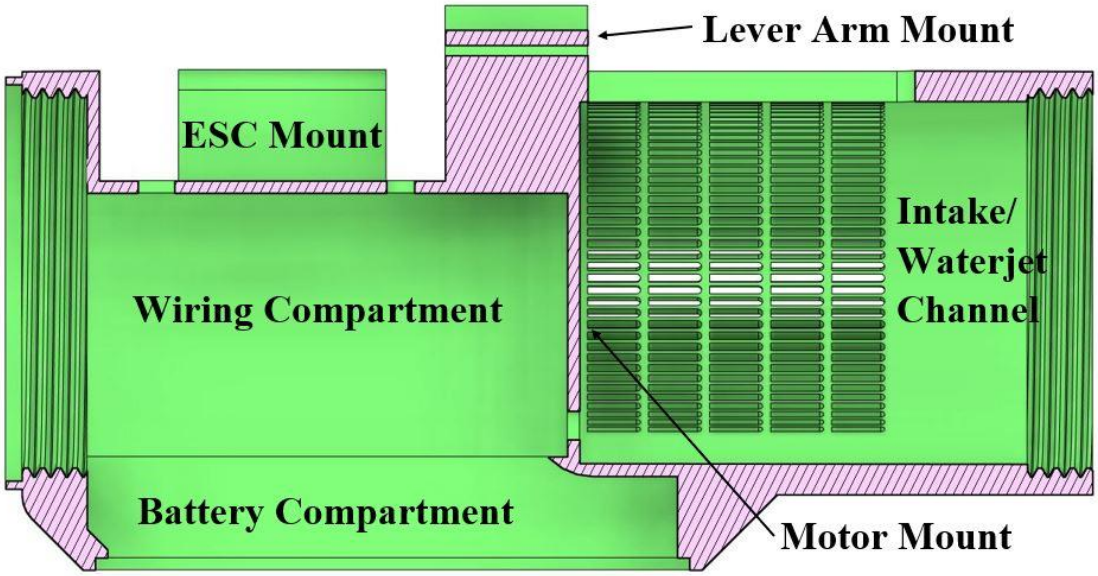

Figure 8.2: Prototype V2 Labeled Cross-Sectional View

Nozzle V1 was carried over from the previous prototype. After initial testing, a new nozzle was developed to address Nozzle V1's design issues. The waterproof cap used for Prototype V1 was also carried over and remained unchanged for Prototype V2.

8.2.1 Motor Mount, Waterjet Channel, and Intake

The motor mount was moved from the inside of the electronics housing in Prototype V1 to the wall separating the electronics housing and waterjet channel in Prototype V2. Mounting the motor inside of the waterjet channel allows the motor to be cooled by the surrounding water, greatly reducing operating temperatures. Unlike Prototype V1's motor mount, which was secured directly to the case of the motor, the new motor mount was designed to secure the mounting bracket attached to the motor (Figure 5.13) to the wall. Attaching the aluminum bracket between the motor and wall

mount improves the structural stability of the assembly. The motor mount, with labeled dimensions, is displayed in Figure 8.3 on the following page.

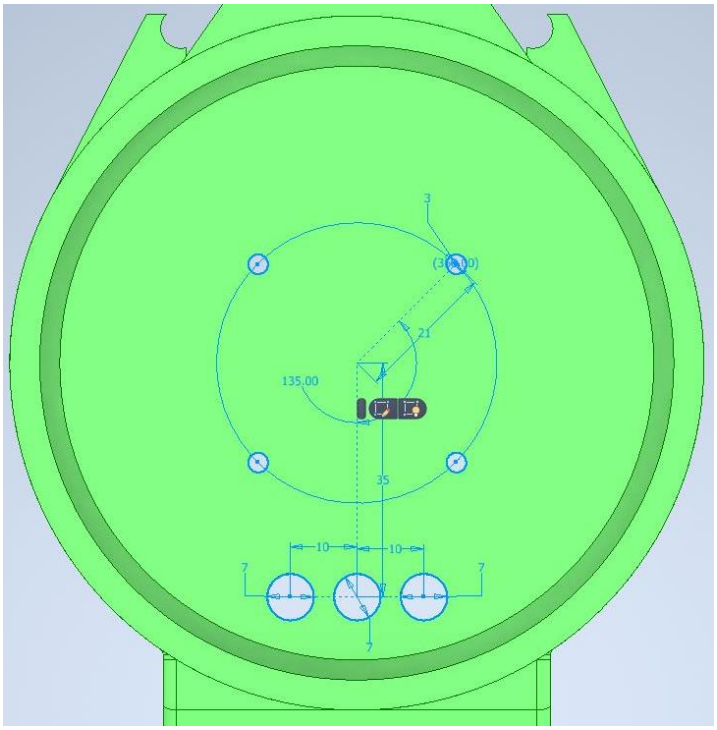

Figure 8.3: Prototype V2 Motor Mount CAD Model and Dimensions

The four 3 mm diameter screw holes served as the mounting points for the aluminum bracket. Once the bracket (with the motor attached) was screwed into place, a washer and nut were attached to the exposed screws on the electronics housing side of the wall to secure the motor. The three 7 mm diameter holes allow the motor wires to be routed into the electronics housing.

The length of Prototype V2's waterjet channel was increased by 10 mm to accommodate the brushless motor. The inner and outer diameters of the channel were left unchanged. A 16 mm long M95x4 interior thread at the end of the waterjet channel was again used to connect the nozzle. Two modifications were made to the

mesh-shaped intake relative to Prototype V1. An additional row of 76 slits was added to increase the total volume of the intake, and a larger slit was designed at the top of the intake to simplify the shaft coupler assembly process. Dimensions of the individual intake slits remained unchanged. Specifications for Prototype V2's waterjet channel and intake can be viewed in Tables 8.1 and 8.2, respectively.

Table 8.1: Prototype V2 Waterjet Channel Specifications

Length (mm)	126.00
Outer Diameter (mm)	104.00
Inner Diameter (mm)	89.00
Cavity Volume (mm^3)	783863.50

Table 8.2: Prototype V2 Intake Specifications

Intake Length (mm)	73
Number of Rows	5
Slits Per Row	76
Total Number of Slits	380
Slit Surface Area (mm^2)	25.571
Allen Key Slit Surface Area (mm^2)	539.089
Total Intake Surface Area (mm^2)	10255.992
Slit Volume (mm^3)	191.781
Allen Key Slit Volume (mm^3)	4043.168
Total Intake Volume (mm^3)	76919.937

8.2.2 ESC Mount

An external mount for the new 150 A ESC was created to harness the water cooling benefits from its waterproof design. Before implementing the external mount to Prototype V2, a prototype of the mount was designed and manufactured to ensure

its functionality. A CAD model of the FLYCOLOR 150 A Waterproof ESC was created based on dimensions acquired with a set of calipers. This CAD model was used to aid in developing the external mount prototype and verifying tolerances. CAD models of the waterproof ESC and external mount prototype can be found in Figures 8.4 and 8.5, respectively.

Figure 8.4: FLYCOLOR 150 A Waterproof ESC CAD Model

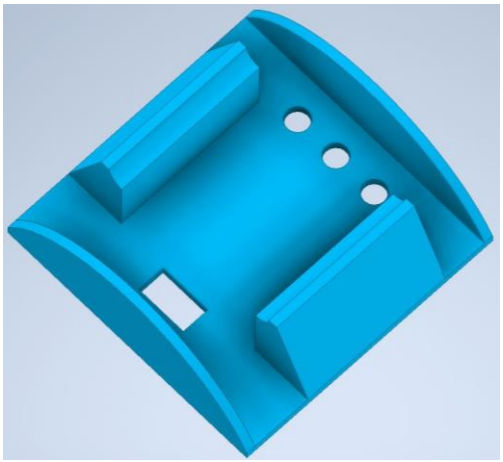

Figure 8.5: Prototype V2 ESC External Mount Prototype CAD Model

The mount was designed to compactly fit the 76.10 mm by 50.25 mm ESC and sit directly above the module's electronics housing. The ESC would be supported along its circular plastic heat pipe shrouds and oriented with the wires facing the

mount. Three 7.5 mm holes at one end of the mount were used to route the 10 AWG motor wires through, and a rectangular hole at the other end was used to route the XT60 battery connector through. When the wires are routed through the holes and connected, the ESC cannot move horizontally. Silicone sealant was used to waterproof the wiring holes, keeping the ESC from moving vertically once seated in the mount. The ESC mounted to the external mount prototype is displayed in Figure 8.6 on the following page.

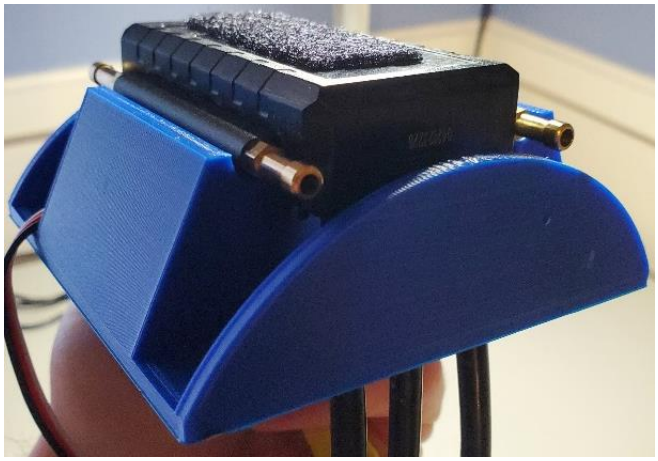

Figure 8.6: External Mount Prototype and ESC Assembly

After confirming functionality with the prototype, the external mount was then added to the design of Prototype V2. At 188.45 g, the ESC was one of the heaviest components on the module. Ideally, the ESC would be located as low on the module as possible to maintain a low center of gravity. However, the location of the ESC mount was restricted by the location of the motor mount. Adequate space had to be left between the inner wall of the ESC mount and the top two screw holes of the motor mount. If the ESC mount was positioned too close to the screw holes, there would not be enough room to assemble the nuts and washers to the motor mount screws. 5.5 mm

of space was left between the inner wall of the ESC mount and screw holes, providing adequate room for assembly. This is displayed in Figure 8.7 below.

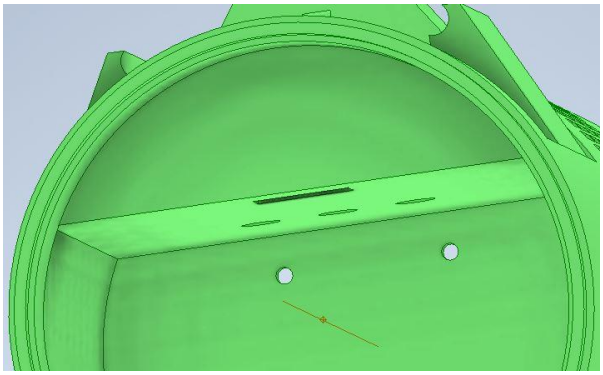

Figure 8.7: Space Between ESC Mount and Screw Holes

8.2.3 Electronics Housing

The new ESC mount receded into the electronics housing, decreasing the total volume of the cavity. This would prove to be a good design change, as a decrease in cavity volume reduced the positive buoyancy of the module. Moving the motor and ESC outside of the electronics housing created additional space for connecting motor and battery wires. The motor wires produced the highest temperature values during thermal testing. Although the larger 10 AWG wire replaced the 16 AWG wire used during thermal testing, the motor wires were still expected to operate at relatively high temperatures. Without the ESC and motor inside the electronics housing, the wires would have plenty of room to be connected without overlapping each other, decreasing thermal-related concerns.

The redesigned battery compartment was also integrated into the electronics housing. Prototype V1's battery compartment was significantly larger and required an additional hinged door to access the battery. This added potential waterproofing

issues, complicated the connection between ESC and battery, and increased the total volume of the module. Moving the battery into the electronics housing simplified the design and reduced the size of the module.

The new battery compartment, displayed in Figure 8.8, featured a 146 mm by 54 mm window to mount the 0.5 mm thick aluminum sheet.

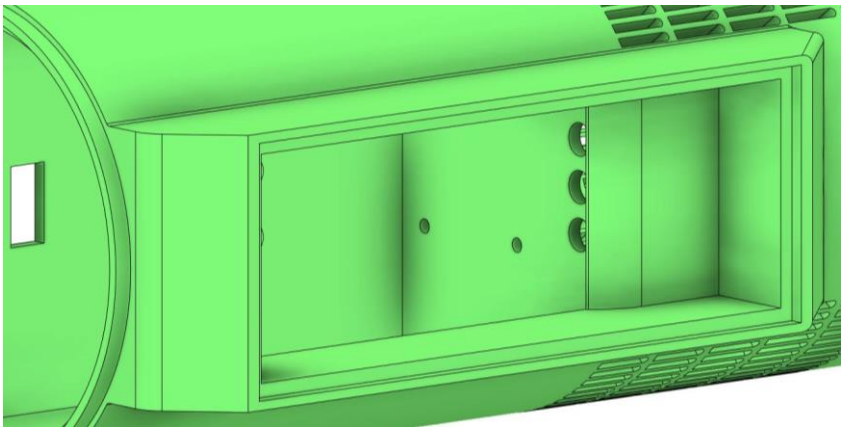

Figure 8.8: Prototype V2 Battery Housing

The 140 mm by 48 mm inner dimensions of the housing were the same as the inner dimensions of the battery test box. To allow the battery to be inserted and removed at the minimum angle possible from the compartment, the electronics housing was lengthened by 21 mm relative to Prototype V1. This also required the battery compartment to be moved from under the waterjet channel to as close to the waterproof cap as possible.

8.3 Center of Gravity and Buoyancy Analysis

Before manufacturing and assembling the components of Prototype V2, a CAD assembly was created to analyze the center of gravity and buoyancy of the propulsion module. Ideally, the module's center of gravity would be at the center of the

horizontal axis and as low as possible on the vertical axis. A horizontally centered, vertically low center of gravity will maintain the module's intended orientation when submerged without flipping over. Neutral buoyancy was targeted to minimize the number of opposing forces acting on the module

8.3.1 Methodology

Autodesk Inventor includes a feature called iProperties, which allows the user to view and edit the physical properties of a specific component or assembly. Using iProperties, the mass of each component in the assembly was edited to reflect the component's actual mass and the volume of each component could be viewed. Inventor defines a component's volume only by the volume of material in the component. Inventor did not account for the volume of empty cavity space within a component but was crucial to consider when estimating for buoyancy.

After creating the assembly, the iProperties tab could be referenced to view the total mass and volume of the module. These values would be used to calculate the buoyancy of the module. The iProperties tab also displays the center of gravity relative to the assembly's datum (0,0,0) defined by Inventor. As this datum did not represent the actual center point of the assembly, the actual center point relative to the datum had to be manually calculated. This value would be used to evaluate the X, Y, and Z delta between the assembly's center point and its center of gravity.

The total length (Y-axis) of Prototype V2's assembly was 454.246 mm and the maximum height was 138.500 mm (X-axis). The calculated center point of the

assembly and CAD rendering displaying the datum and calculated center-point can be viewed in Table 8.3 and Figure 8.9, respectively.

Table 8.3: Calculated Center Point of Prototype V2 Assembly

Prototype V2 Center Point		
X (mm)	Y (mm)	Z (mm)
1.250	132.123	0.000

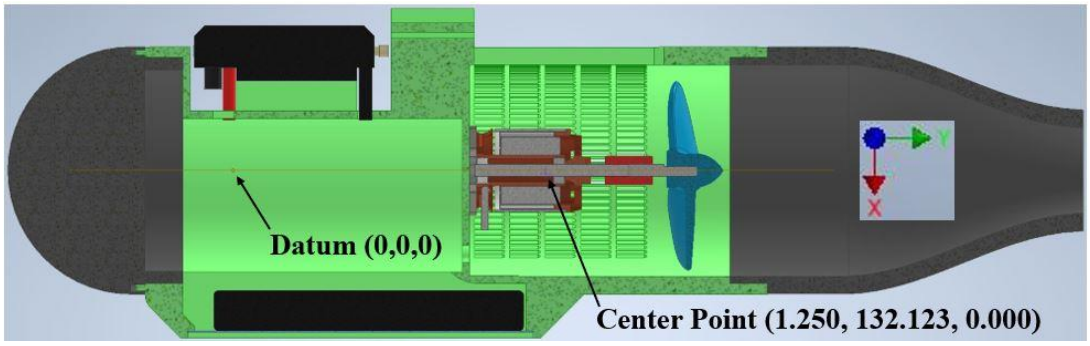

Figure 8.9: Prototype V2 Assembly with Datum and Center Point

8.3.2 COG and Buoyancy Calculation Without Ballast

A baseline center of gravity and buoyancy calculation was first completed to determine if ballast would be required. In addition to the propulsion module components, this assembly also included volumes of water inside the waterjet channel and nozzle to replicate the total mass and volume of the module when submerged. A CAD model of the assembly, and a list of all assembly components and their masses, can be viewed in Figure 8.10 and Table 8.4, respectively, on the following page.

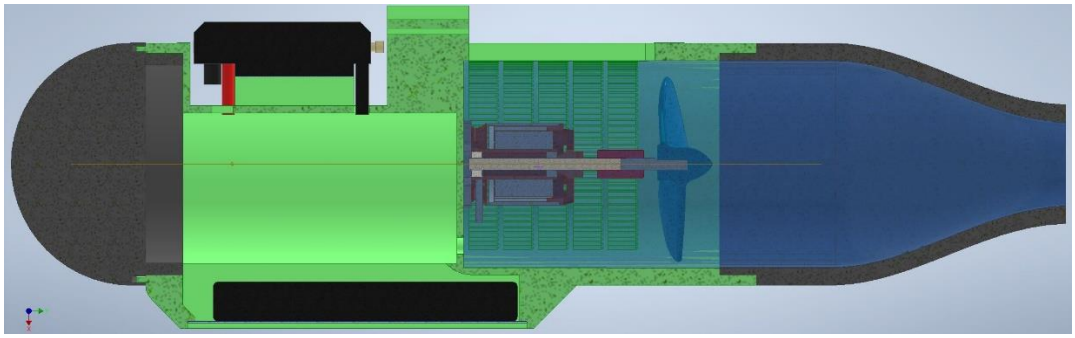

Figure 8.10: Prototype V2 Assembly with Water Volumes

Table 8.4: Prototype V2 Assembly Component Mass (with Water)

Component	Mass (g)
Propulsion Module V2	461.54
Nozzle V1 36 mm D	151.22
Waterproof Cap	189.40
3-Blade Impeller	14.40
3200 mAh LiPo Battery	216.71
DYS 3548-5 Brushless Motor	160.99
150 A Waterproof ESC	188.45
Driveshaft	4.41
Shaft Connector	5.50
Brushless Motor Mount Bracket	10.60
146x54 mm Aluminum Sheet	8.69
Nozzle V1 36 mm D Water	636.61
Waterjet Channel Water	643.69
Total Mass (g)	2692.20

The total dry mass of Prototype V2 was 1411.91 g. After adding volumes of water in the waterjet channel and nozzle, the wet mass increased to 2692.20 g. It was important to calculate the center of gravity and buoyancy of the assembly with water in the channels. This replicated the submerged environment that the module will operate in.

The first parameter calculated was the center of gravity relative to the module's center point. iProperties displays the X, Y, and Z components of the assembly's center of gravity. These values were used to calculate the deltas between the center of gravity and the center point of the module. Equation 8.1 below was used to calculate the X, Y, and Z deltas.

$$X_{Delta} = X_{COG} - X_{CP} \qquad Eq.\ 8.1$$

X_{COG} is the X/Y/Z component of the center of gravity, X_{CP} is the X/Y/Z component of the center point, and X_{Delta} is the difference between the two values. These deltas could then be used to identify where ballast should be located to maneuver the center of gravity closer to the center point of the module. The center of gravity and delta to midpoint values for the assembly are displayed in Table 8.5. The location of the center of gravity on the assembly is shown in Figure 8.11.

Table 8.5: Prototype V2 Assembly (No Ballast) Center of Gravity and Deltas

Center of Gravity (No Ballast)				
X (mm)	X Delta from Midpoint (mm)	Y (mm)	Y Delta from Midpoint (mm)	Z (mm)
1.706	0.456	143.777	11.654	0.000

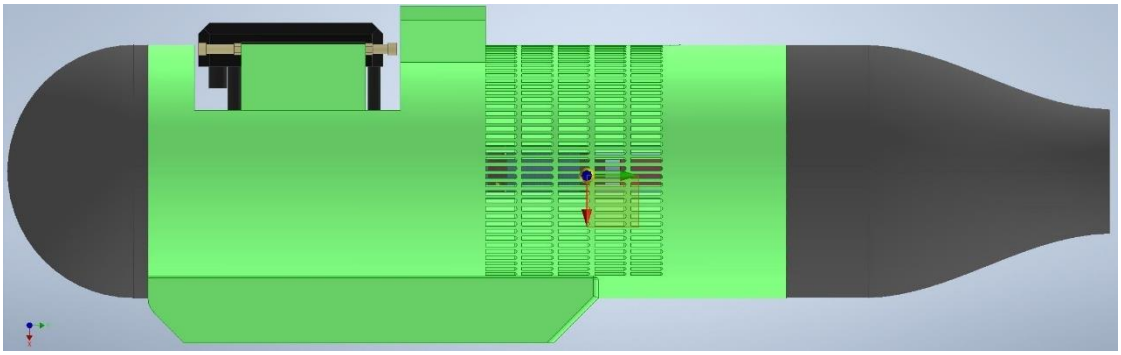

Figure 8.11: Prototype V2 Assembly (No Ballast) Center of Gravity Location

The X delta between the center of gravity and midpoint was only 0.456 mm, with the center of gravity slightly below the midpoint of the module. The Y delta was much larger at 11.654 mm as the center of gravity was further towards the rear of the module (nozzle) than the midpoint. The Z delta was 0 mm as the Z component of both the center of gravity and midpoint was 0.

If the module were submerged in water in its current configuration, it would tilt with the nozzle facing downward. This orientation would significantly decrease the thrust performance and efficiency of the module. The ballast will have to be placed towards the front of the module to move the center of gravity closer towards the center point and ensure the module will remain parallel to the Y-axis when submerged.

The buoyancy of the module was the next parameter calculated. iProperties displays the total volume and mass of the assembly. The volume parameter from iProperties only represents the volume of all the components in the assembly. It does not account for the volume of the empty cavity. Using Inventor's patch and sculpt tools, the cavity volume of the electronics housing was calculated. This value included the battery compartment and space between the cap and housing. The LiPo battery was the only component in the electronics housing, but its volume was already accounted for in the iProperties total volume output. Because of this, the volume of the LiPo battery was subtracted from the cavity volume to get a more accurate estimation. The cavity volume was then added to the total volume calculated by iProperties.

The cylindrical volume of water added inside the waterjet channel overlapped the motor, mounting bracket, driveshaft, shaft coupler, and impeller. To account for this, the volume of these motor assembly components needed to be subtracted from the total volume output from iProperties to increase the accuracy of the buoyancy calculation. Table 8.6 below displays the iProperties, cavity, and motor assembly volumes used to calculate the final assembly's volume.

Table 8.6: Prototype V2 Assembly (No Ballast) Volumes

iProperties Assembly Volume (mm^3)	2658516.234
Electronics Housing Cavity Volume (mm^3)	824914.439
Motor Assembly Volume (mm^3)	38702.349
Total Additional Volume (mm^3)	786212.090
Final Assembly Volume (mm^3)	3444728.324

The final assembly volume displayed above was used for buoyancy calculations. The buoyancy force acting on the propulsion module was calculated using Equation 8.2 below.

$$F_B = V * \rho * g \qquad \textit{Eq. 8.2}$$

V is the final assembly volume from Table 8.6 in m^3, ρ is the density of water (997 kg/m^3), g is the gravitational constant (9.81 m/s^2), and F_B is the buoyancy force acting on the module. The gravitational force acting on the module was then calculated using Equation 8.3 below.

$$F_G = m * g \qquad \textit{Eq. 8.3}$$

m is the total mass of the assembly in kg (including water mass), g is the gravitational constant, and F_G is the gravitational force acting on the module. The two force vectors oppose each other, with the buoyancy force pushing the module upward and the gravitational force pushing the module downwards. The delta between the two forces, calculated with Equation 8.4, determined the buoyancy of the module.

$$F_{Delta} = F_B - F_G \qquad Eq.\ 8.4$$

The module would be positively buoyant if the force delta is greater than 0. Conversely, the module would be negatively buoyant if the force delta value is less than 0. A force value equal to 0 would represent neutral buoyancy. Buoyancy force values calculated for this assembly are organized in Table 8.7 below.

Table 8.7: Prototype V2 Assembly (No Ballast) Buoyancy Calculations

Buoyancy Analysis (No Ballast)				
Total Volume (m^3)	**Total Mass (kg)**	**Buoyancy Force (N)**	**Gravitational Force (N)**	**Force Delta (N)**
0.003444728324	2.692204	33.691	26.411	7.281

In the module's current configuration, the force delta was calculated to be 7.281 N, meaning the module would be positively buoyant. Additional ballast will be required to increase the gravitational force of the module and drive the force delta closer to neutral buoyancy.

8.3.3 COG and Buoyancy Calculation With Ballast

Ballast needed to be added to the propulsion module to manipulate its center of gravity and decrease its buoyancy force delta. 3.175 mm lead sheet was used for ballast due to its high density of 11.29 g/cm^3. Lead sheet is also easy to work with and

can be formed into various geometries with simple tools. Due to its high density, adding lead ballast to the module will significantly increase the gravitational force acting on the module while minimally increasing the buoyancy force acting on the module. The location of the ballast will also heavily impact the location of the module's center of gravity.

The optimal amount of ballast would achieve the desired center of gravity and neutral buoyancy with a minimal amount of additional mass. Multiple different ballast setups were analyzed using the assembly. Ballast setups that were more efficient at manipulating the location of the module's center of gravity did not always add enough mass to achieve neutral buoyancy. Adding more ballast to these setups to achieve neutral buoyancy would once again offset the location of the center of gravity. An optimized ballast setup that satisfied both conditions had to be created.

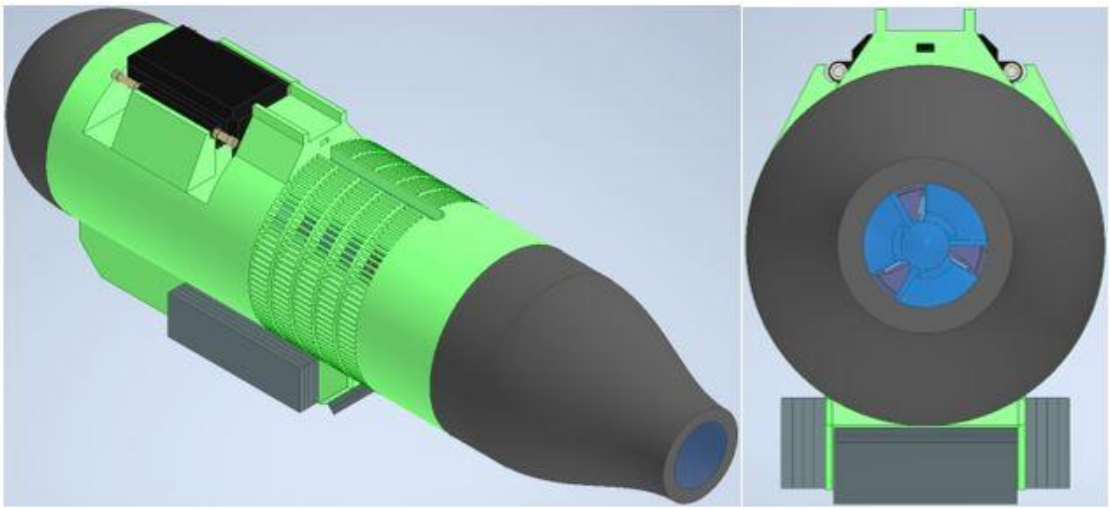

Figure 8.12: Prototype V2 Ballast Setup

The final optimized ballast setup selected for Prototype V2 is displayed in Figure 8.12 above. Eight 90 mm x 26 mm x 3.175 mm pieces of lead ballast,

weighing 88.180 g each, and two 53 mm x 25 mm x 3.175 mm pieces of lead ballast, weighing 49.120 g each, were used for this setup. The total additional mass added by the lead ballast was 803.680 g. Four 90 mm x 26 mm x 3.175 mm ballast pieces flanked each side of the battery compartment, located as close to the nozzle as possible. The two 53 mm x 25 mm x 3.175 mm ballast pieces were mounted to the back face of the battery compartment. A breakdown of individual component mass in this assembly can be viewed in Table 8.8 on the following page.

Table 8.8: Prototype V2 Assembly (With Ballast) Component Mass

Component	Mass (g)
Propulsion Module V2	461.54
Nozzle V1 36 mm D	151.22
Waterproof Cap	189.40
3-Blade Impeller	14.40
3200 mAh LiPo Battery	216.71
DYS 3548-5 Brushless Motor	160.99
150 A Waterproof ESC	188.45
Driveshaft	4.41
Shaft Connector	5.50
Brushless Motor Mount Bracket	10.60
146x54 mm Aluminum Sheet	8.69
Nozzle V1 36 mm D Water	636.61
Waterjet Channel Water	643.69
(8) 90x26 mm Ballast	705.44
(2) 53x25 mm Ballast	98.24
Total Mass (g)	3495.88

The center of gravity and delta to midpoint values for the assembly with ballast are displayed in Table 8.9. The location of the center of gravity on the new assembly is shown in Figure 8.13 on the following page.

Table 8.9: Prototype V2 Assembly (With Ballast) Center of Gravity and Deltas

Center of Gravity (Eight 90x26mm Ballast, Two 53x25mm Ballast)				
X (mm)	X Delta from Midpoint (mm)	Y (mm)	Y Delta from Midpoint (mm)	Z (mm)
14.623	13.373	131.160	-0.963	0.000

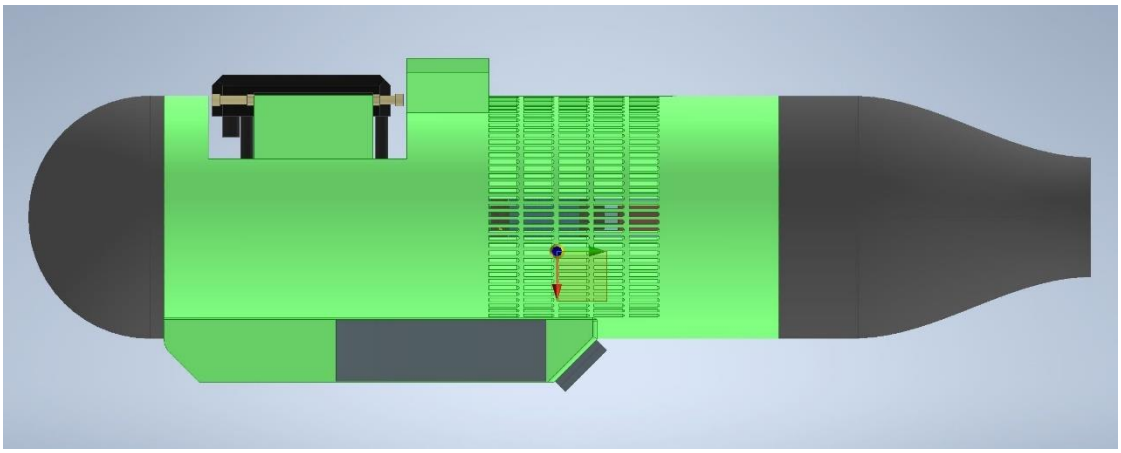

Figure 8.13: Prototype V2 Assembly (With Ballast) Center of Gravity Location

The X delta between the center of gravity and midpoint was 13.373 mm, moving the center of gravity well below the midpoint of the module. The Y delta shrunk to -0.963 mm, moving the center of gravity forward to the midpoint. Compared to the assembly without ballast, the center of gravity's X component was lowered by 12.917 mm, and the Y component was nearly centered, moving forward by 12.617 mm. Buoyancy calculations for the assembly are organized in Table 8.10 below.

Table 8.10: Prototype V2 Assembly (With Ballast) Buoyancy Calculations

Buoyancy Analysis (Eight 90x26mm Ballast, Two 53x25mm Ballast)				
Total Volume (m^3)	Total Mass (kg)	Buoyancy Force (N)	Gravitational Force (N)	Force Delta (N)
0.003522757074	3.495884	34.455	34.295	0.160

The additional 803.68 g of mass added by the lead ballast increased the gravitational force acting on the module by 7.884 N to 34.295 N. The buoyancy force of the module only increased by 0.764 N to 34.455 N, driving the force delta to 0.160 N, ensuring the module will be essentially neutrally buoyant.

8.4 Physical Assembly and Waterproofing Issues

The brushless motor and ESC were the first components assembled to Prototype V2. With these components in place, the wiring holes for each component were sealed using a silicone sealant. The aluminum sheet was then secured to the window on the battery housing using a marine adhesive. At this point, Prototype V2 (with the waterproof cap screwed on) was submerged in the test tub to verify that the module was waterproof. Unfortunately, the module did not pass this initial test after multiple leaks were discovered at the motor wire holes. Silicone sealant was removed and reapplied to the motor wire holes, however, further testing remained unsuccessful. Due to the lack of access to the motor wire holes, the aluminum sheet and brushless motor had to be disassembled to address the waterproofing issues.

This troubleshooting process proved to be extremely tedious and delayed physical testing. Multiple weeks were spent chasing waterproofing issues as the silicone sealant and marine adhesive required a full day to cure before being exposed to water. Eventually, a solution for the leaks at the motor wire holes was found. The motor wires were carefully routed through the holes such that the wires did not touch the edges of the holes. This allowed silicone sealant to be applied evenly around the wires without leaving any gaps at the edges of the holes. A minor leak was still present but did not present a danger for electronic component failure. Figure 8.14

displays the silicone applied on the front and back of the motor mount and wiring holes. A fully assembled image of Prototype V2 is shown in Figure 8.15.

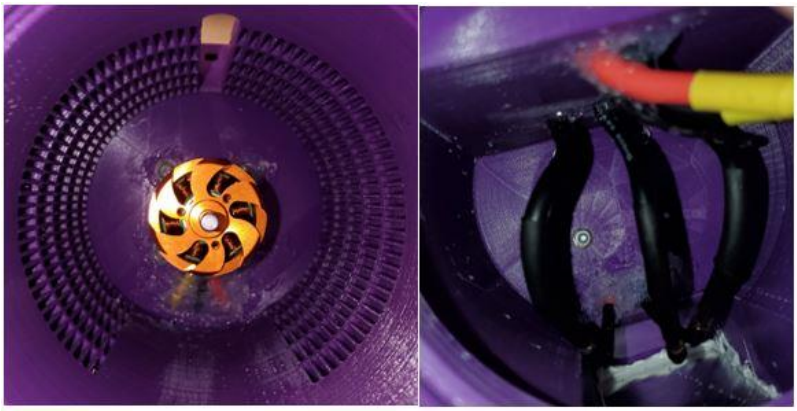

Figure 8.14: Silicone Applied to Motor Mount and Wiring Holes

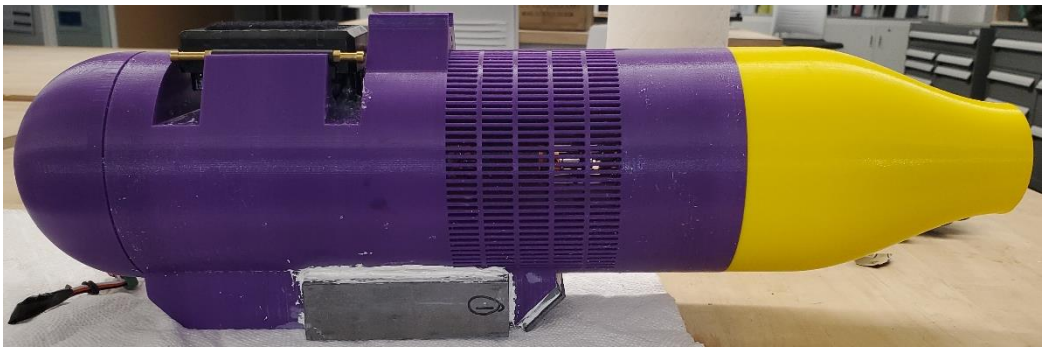

Figure 8.15: Prototype V2 Fully Assembled

8.5 Initial Testing

8.5.1 Testing Setup

The lever arm of the testing apparatus was attached to the mount on Prototype V2 using a zip tie. An extension cable was used to connect the onboard ESC to the servo tester secured to the testing apparatus. The extension cable and ESC connection was fully submerged and needed to be waterproofed. Several layers of electrical tape were applied at the joint to ensure water would not compromise the connection. The

thermometer used for thermal testing was routed through the ESC XT60 hole to record battery temperature data. A laptop next to the testing apparatus was used to power the thermometer. Prototype V2 assembled to the testing apparatus is displayed in Figure 8.16 below.

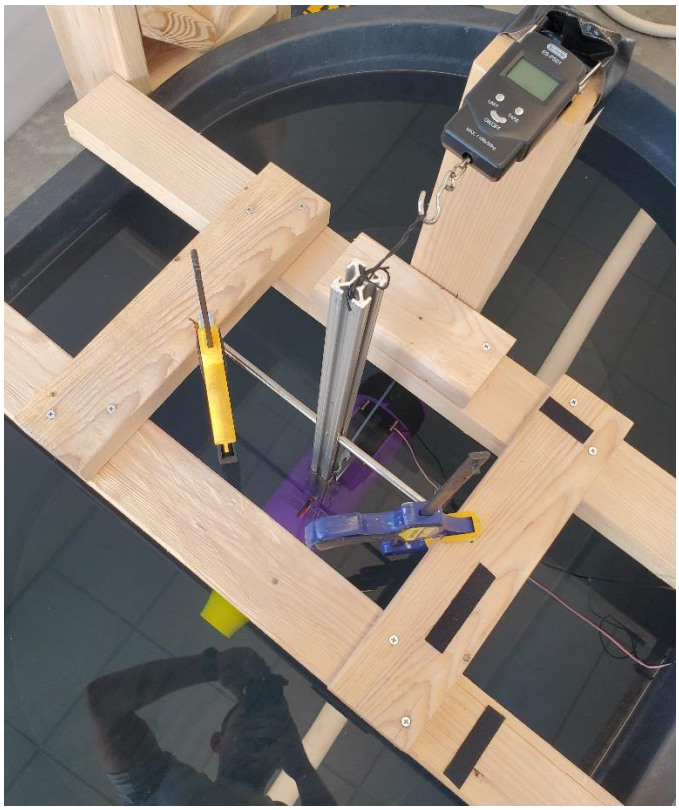

Figure 8.16: Prototype V2 Assembled to Testing Apparatus

8.5.2 Testing Results

Prototype V2 initial testing was primarily intended to verify the module's functionality and optimize the performance of Nozzle V1. Any issues with the module would be addressed in the design of the final nozzle. The best performing nozzle of the five with different outlet diameters would be selected as the basis for the final dual-channel nozzle.

The 36 mm outlet diameter nozzle was the first nozzle tested on the module. Upon startup, the throttle was set to 30% to verify the module was operating correctly. The module did not appear to rotate the lever arm at all, and the force gauge was displaying negative values. Increasing the throttle percentage did not solve this issue. After reaching into the tub while the module was running, it was discovered that a "suction" effect was occurring at the nozzle's outlet. Fluid was entering through the outlet of the nozzle and exiting through the intake, opposite of the intended direction of flow.

Initially, it was thought that the motor was running in the wrong direction. The direction of the motor was reversed, and Prototype V2 was tested again. Reversing the direction of the motor only enhanced the issue, verifying that the motor was in fact spinning in the correct direction during the first test. The 40 mm and 50 mm outlet diameter nozzles were tested next. Both larger outlet diameter nozzles experienced the same suction phenomena during testing. Likewise, the 20 mm and 30 mm outlet diameter nozzles also did not solve this issue.

A resistance issue appeared to be causing the reversal of the flow direction. Fluid preferred to enter through the nozzle outlet rather than the intake, possibly due to greater resistance at the intake. Large sections of the intake were cut out to increase the total open surface area, with the intent of decreasing fluid resistance at the intake. Intake modifications are displayed in Figure 8.17 on the following page.

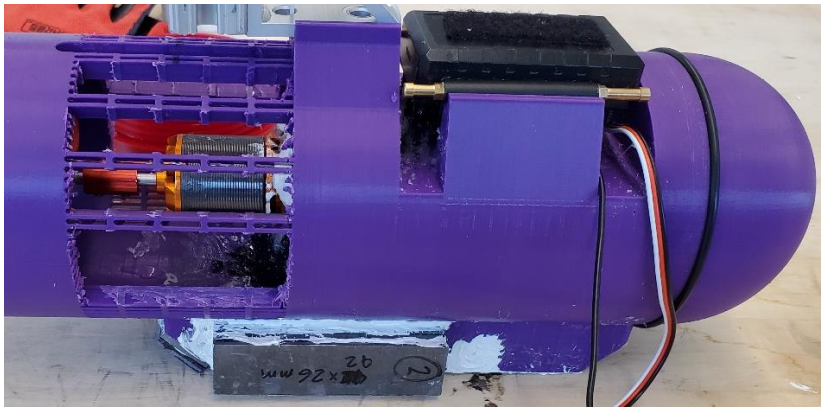

Figure 8.17: Prototype V2 Intake Modifications

With the modified intake, Prototype V2 was once again tested with all five nozzles. Unfortunately, the reversed flow direction issue persisted. Several more tests were conducted with tape covering specified lengths of the intake as shown in Figure 8.18 below.

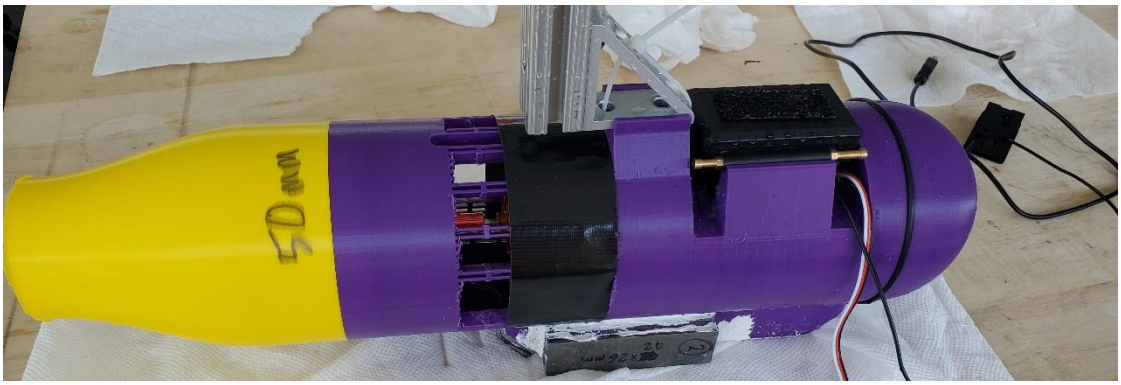

Figure 8.18: Prototype V2 Modified Intake with Tape

These tests intended to determine if decreasing the intake's open surface area would influence the direction of flow. Similar to previous tests, taping specified lengths of the intake did not solve the flow reversal issue.

A deeper analysis into the Nozzle V1 CFD simulation results from Table 6.6 was conducted to identify the root cause of the flow reversal issue. Figure 8.19 below is a plot constructed from simulation data displaying the static pressure at each nozzle's outlet.

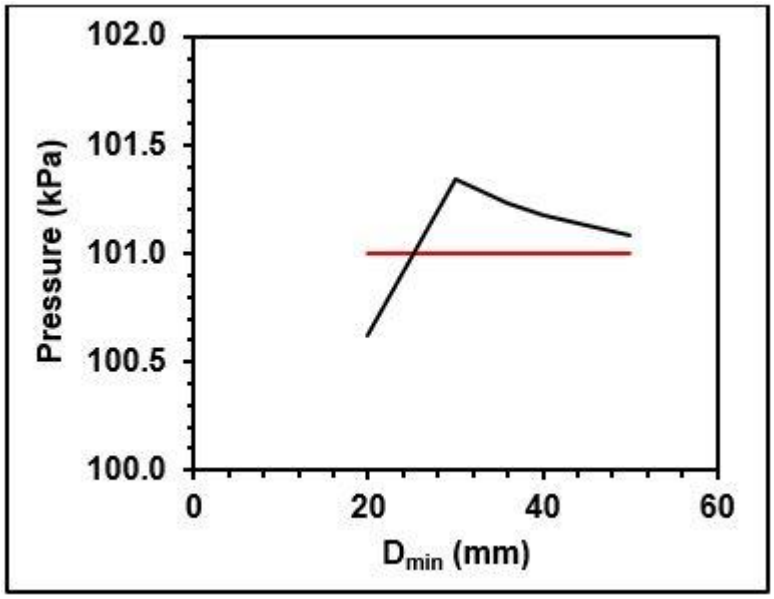

Figure 8.19: Nozzle V1 Outlet Static Pressure Plot

The red line is representative of ambient pressure, 101 kPa. The 30 mm, 36 mm, 40 mm, and 50 mm outlet diameter versions of Nozzle V1 all have outlet static pressures exceeding ambient pressure. This could have potentially caused the flow reversal issue experienced during the initial testing of Prototype V2. The 20 mm outlet diameter version of Nozzle V1 was the only nozzle with an outlet static pressure below ambient. Although the flow reversal issue was still present when testing this 20 mm outlet diameter nozzle, the effects were not as severe relative to the other four nozzles.

8.6 Nozzle V2 Design

A new nozzle was designed to combat the flow reversal problem experienced during initial testing. The two-stage design of Nozzle V1 included a 50 mm waterjet channel extension followed by the 100 mm tapered section, significantly increasing the internal volume of the nozzle. Fluid energized by the impeller would have to travel the entire length of this nozzle and exit through a relatively small diameter outlet. Prototype V2's motor and impeller combination could not generate enough power to move such a large volume of fluid through the nozzle to the outlet. It was theorized that the energized fluid would travel through the channel extension section of the nozzle but stalled once it reached the tapered section. This potentially reversed the direction of the flow field, creating the suction effect at the nozzle's outlet.

The primary design objectives for Nozzle V2 were to simplify the nozzle's geometry, shorten the length of the nozzle, and increase outlet diameters. Four nozzles with outlet diameters of 70 mm, 65 mm, 60 mm, and 50 mm were designed and manufactured for testing. Figure 8.20 below displays a CAD model and manufactured prototype of Nozzle V2 with a 65 mm diameter outlet.

Figure 8.20: Nozzle V2 65mm Diameter Outlet

Like Nozzle V1, Nozzle V2 features a 16 mm long M95x4 exterior thread to attach the nozzle to the propulsion module. A simplified conical geometry was used for the design of Nozzle V2. Instead of featuring a tapered section, the diameter of the nozzle decreases linearly from inlet to outlet. Specifications for the new nozzles are organized in Table 8.11 below.

Table 8.11: Nozzle V2 Specifications

Outlet Diameter (mm)	Inlet Diameter (mm)	Length (mm)	Length w/ Thread (mm)	Internal Volume (mm^3)
50	89	44	60	171301.623
60	89	44	60	194224.777
65	89	44	60	206550.292
70	89	44	60	219451.766

All four nozzles share the same inlet diameter and length but differ in outlet diameter and internal volume. A length over diameter ratio study, displayed in Table 8.12 below, was completed to compare the dimensional specifications of Nozzle V1 to Nozzle V2.

Table 8.12: Nozzle V1 vs Nozzle V2 Length over Diameter Study

Nozzle	Inlet Diameter (D, mm)	Outlet Diameter (d, mm)	Length (mm)	L/D	L/d	D/d	Internal Volume (mm^3)
V1 20mmD	89	20	130.756	1.469	6.538	4.450	474566.833
V1 30mmD	89	30	132.396	1.488	4.413	2.967	513181.419
V1 36mmD	89	36	133.246	1.497	3.701	2.472	538984.336
V1 40mmD	89	40	133.759	1.503	3.344	2.225	557275.618
V1 50mmD	89	50	134.855	1.515	2.697	1.780	606761.172
V2 50mmD	89	50	44	0.494	0.880	1.780	171301.623
V2 60mmD	89	60	44	0.494	0.733	1.483	194224.777
V2 65mmD	89	65	44	0.494	0.677	1.369	206550.292
V2 70mmD	89	70	44	0.494	0.629	1.271	219451.766

Nozzle V1 ratios and internal volumes were significantly larger than Nozzle V2. Nozzle V2 was designed to target length over diameter ratios below 1 to contrast with the dimensional parameters of Nozzle V1. A 50 mm outlet diameter Nozzle V2,

which shares the same outlet diameter as a version of Nozzle V1, was designed to test if the inlet diameter over outlet diameter ratio impacted the flow reversal issue.

Shortening the length of Nozzle V2 by approximately 90 mm brings the outlet of the nozzle closer to the impeller. The motor and impeller will have to move the fluid volume a significantly shorter distance to travel through the nozzle. Increasing the size of the outlet diameters should also decrease the pressure buildup within the nozzle, decreasing the fluid resistance to exit through the nozzle's outlet.

8.7 Testing Part 2

The second round of testing was conducted to determine if the new design of Nozzle V2 would eliminate the flow reversal problem from initial testing. With the modified intake, the same propulsion module was reused for the second part of testing. Printing and reassembling a new propulsion module proved too costly and time-consuming for it to make sense logistically. Regardless, the suction issue from initial testing remained present after modifying the intake. Although the intake would not be representative of the original, the success of Nozzle V2 with this modification would still provide valuable knowledge for the development of the final prototype.

No alterations were made to the testing setup and methodology used for initial testing. Figure 8.21 on the following page shows Prototype V2, with the 70 mm outlet diameter Nozzle V2 attached, prepared for testing.

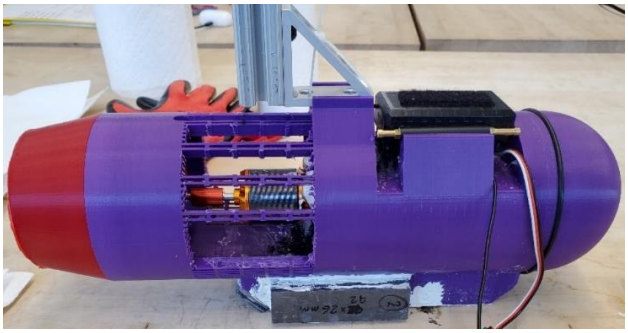

Figure 8.21: Prototype V2 with 70 mm Outlet Diameter Nozzle V2 Attached

A total of eight tests were conducted, two with each of the new nozzles. The motor was run at 80% throttle for the duration of a single battery charge for one test and 100% throttle for the other. Thrust values, battery temperatures, and operational times were recorded for each test. Testing results are organized in Table 8.13 below and are displayed graphically in Figures 8.22, 8.23, and 8.24 on the following page.

Table 8.13: Prototype V2 Testing Part 2 Results

Nozzle	Throttle (%)	Max Thrust (lbf)	Avg. Thrust (lbf)	Initial Battery Temp (C)	Max Battery Temp (C)	Runtime
V2 70mmD	80	8.07	7.50	21.7	54.1	4 min 38 sec
V2 65mmD	80	9.01	8.25	22.0	56.2	4 min 18 sec
V2 60mmD	80	7.49	6.75	23.1	59.7	4 min 22 sec
V2 50mmD	80	4.67	4.25	22.7	63.3	3 min 56 sec
V2 70mmD	100	10.03	9.50	23.2	65.9	3 min 07 sec
V2 65mmD	100	11.39	10.50	21.4	68.7	2 min 59 sec
V2 60mmD	100	9.53	8.75	21.9	72.4	2 min 59 sec
V2 50mmD	100	5.11	4.50	22.5	76.8	2 min 34 sec

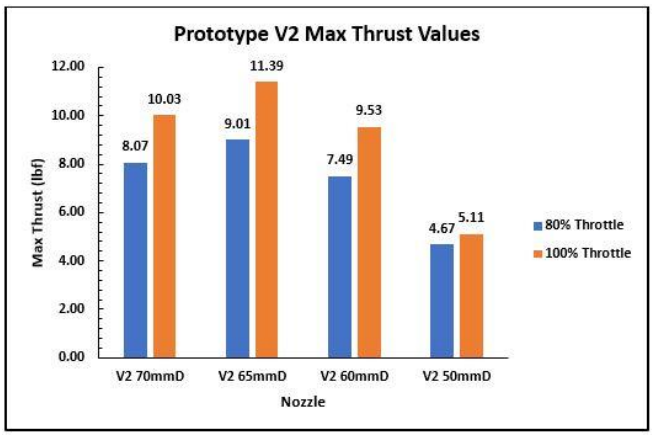

Figure 8.22: Prototype V2 Max Thrust Values

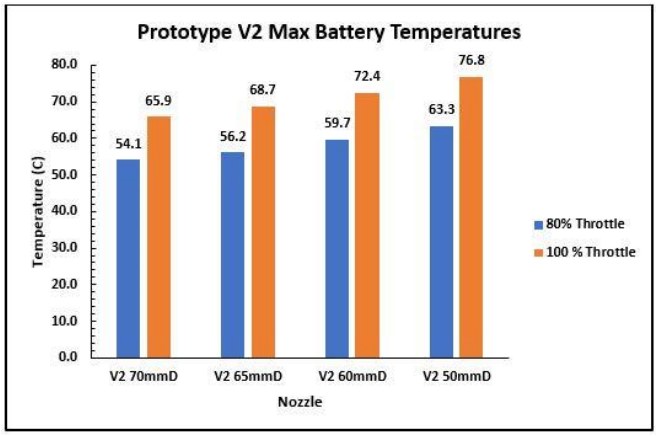

Figure 8.23: Prototype V2 Max Battery Temperatures

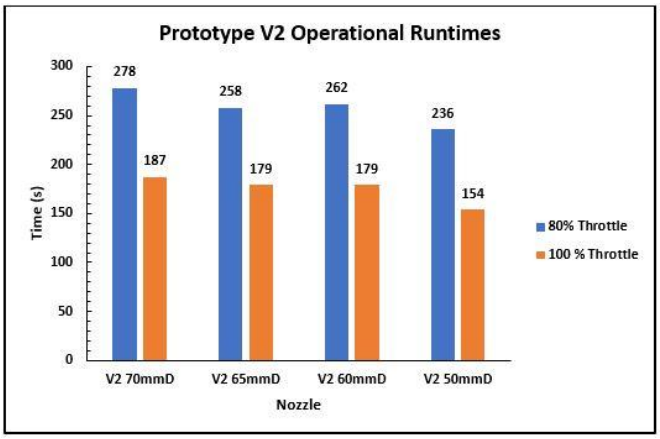

Figure 8.24: Prototype V2 Operational Runtimes

This second round of testing confirmed that Nozzle V2 eliminated the flow reversal problem experienced during initial testing. The 65 mm outlet diameter nozzle emerged as the best performer of the four nozzles in terms of thrust at both 80% and 100% throttle. Decreasing the outlet diameter below 65 mm yielded lower thrust values, likely due to increased pressure buildup throughout the nozzle. The 70 mm outlet diameter nozzle appeared to be the best all-around performer of the four nozzles. Although this nozzle only posted the second-highest thrust values, the nozzle did produce the lowest maximum battery temperatures and longest operational times during both 80% and 100% throttle tests. Compared to the 65 mm outlet diameter nozzle, the 70 mm outlet diameter nozzle on average produced 11.19% lower maximum thrust values, 3.91% lower maximum battery temps, and 5.74% longer operational times. The 50 mm outlet diameter nozzle performed the worst in all categories substantially.

The 70 mm and 65 mm outlet diameter versions of Nozzle V2 appeared to be the optimal nozzles choices for Prototype V2. Because of Prototype V2's modified intake, it was not guaranteed that this would remain the case with the Final Prototype. Before developing the final dual-channel nozzle, the 70 mm, 65 mm, and 60 mm outlet diameter versions of Nozzle V2 would first be tested with the Final Prototype. A 62.5 mm, outlet diameter nozzle was also manufactured for Final Prototype testing. The best performing single-channel nozzle with the Final Prototype would be chosen as the basis for dual-channel nozzle development.

8.8 Motor Case Impeller Design and Testing

An impeller designed to mount directly to the DYS 3548-5 brushless motor was created to increase propulsion module thrust output further. This impeller would be operated in conjunction with the primary 3-blade impeller. A CAD model and physical prototype of the motor case impeller are displayed in Figure 8.25 below.

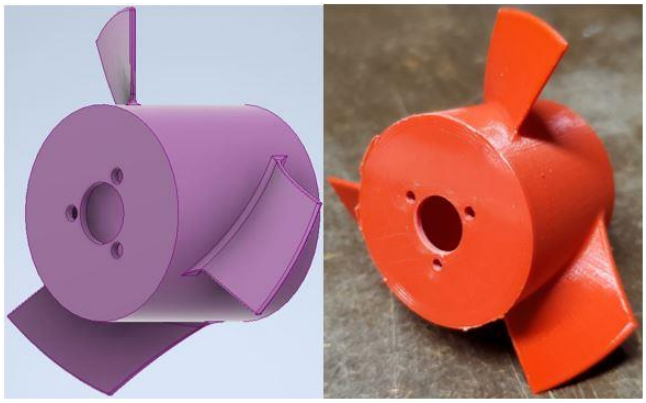

Figure 8.25: Motor Case Impeller CAD Model and Physical Prototype

The motor case impeller was designed to act as a shroud for the brushless motor, secured to the front of the motor with three screws. When operating underwater, the case of the brushless motor rotates freely, generating turbulent vortices. These vortices could potentially disturb the flow field entering the intake and decrease the overall efficiency of the propulsion module. Ideally, the motor case impeller would neutralize the formation of vortices and help reshape the flow field before reaching the primary 3-blade impeller. Figure 8.26 on the following page shows the motor case impeller assembled to the brushless motor on Prototype V2.

Figure 8.26: Motor Case Impeller Assembled to Prototype V2

The motor case impeller was tested on Prototype V2 without a nozzle attached to verify functionality. The brushless motor was run at 100% throttle to determine the maximum thrust output of the setup. Early in the test, it was evident that the motor case impeller had created a new problem. Battery temperatures were increasing at an alarming rate relative to previous tests and the max recorded thrust value was only 4.29 lbf. After one minute and six seconds, the motor ceased operating. Smoke began exiting from the electronics housing once the waterproof cap was removed.

Upon further inspection, it appeared that one of the motor wires had experienced a failure. The wire was desoldered from the bullet connector after reaching critically high temperatures. The case impeller's additional 12.9 g of rotating mass increased the load on the motor enough to increase the total resistance in the circuit significantly. Increased resistance in the electronic components caused temperatures to spike, leading to the motor wire failure. Although the motor case

impeller still presented a potential for further development, the concept had to be abandoned due to time constraints.

8.9 Prototype V2 Conclusions

Prototype V2 successfully fulfilled its primary goal to create a functional propulsion module prototype. After diagnosing the flow reversal issues with Nozzle V1, Prototype V2 was physically tested using the redesigned Nozzle V2. Despite Prototype V2's overall success, questions remained after testing. All of Prototype V2's physical testing was completed using the modified intake. The single-channel versions of Nozzle V2 would still need to be tested with the Final Prototype to ensure the propulsion module will correctly function with the intake as intended. Development of the dual-channel nozzle will commence once this has been verified.

9. Final Propulsion Module Prototype

The Final Prototype was the first propulsion module to implement the innovative dual-channel nozzle design. Before dual-channel nozzle development, multiple new motor and impeller setups were tested to optimize the performance of the Final Prototype. Subtle adjustments were made to the Final Prototype propulsion module component relative to Prototype V2. A majority of the work completed with the Final Prototype focused on optimizing propulsion module performance and experimentally verifying the theoretical benefits of the dual-channel nozzle.

9.1 Electronic and Mechanical Components

The HOOVO 3200 mAh 11.1 V 3S 50C LiPo battery, FLYCOLOR 150 A Waterproof ESC, and 5 mm to 5 mm shaft connector were all carried over from Prototype V2 to be used in the Final Prototype. The servo tester and 300 mm extension cable used for Prototype V2 were also carried over to control the speed of the brushless motor.

The DYS 3548-5 brushless motor used in Prototype V2 was set to be replaced after the motor wire failure experienced during motor case impeller testing. DYS manufactures three different 3548 motors: the 3548-6, 3548-5, and 3548-4. All three of these motors are dimensionally identical but differ in KV rating. The mid-range 3548-5 had a 900 KV rating, while the 3548-6 and 3548-4 had KV ratings of 790 KV and 1100KV, respectively. The 790 KV DYS 3548-6 was initially chosen to replace the 900 KV DYS 3548-5 used in Prototype V2. Lower KV brushless motors offer increased torque numbers and tend to make peak power at lower RPM. Although the maximum unloaded RPM of the 900 KV motor was 9990 RPM, this RPM value

would never be reached when operating an impeller underwater. The same remains true for the 790 KV motor with a maximum unloaded RPM of 8769 RPM. However, the benefits of increased torque and producing peak power at lower RPMs should make the 790 KV brushless motor a better performance choice. The lower KV rating will also decrease the total resistance in the circuit, decreasing electronic component temperatures.

Unfortunately, the manufacturer shipped the 1100 KV 3548-4 model instead of the 790 KV 3548-6. Due to time constraints, the 1100 KV motor was used for initial Final Prototype testing but experienced a failure before dual-channel nozzle testing. The 790 KV 3548-6 brushless motor was purchased once again and replaced the 1100 KV 3548-4 for the remainder of testing.

Two new impellers were also introduced for Final Prototype testing. One of the impellers was heavily inspired by the design of a jet ski impeller. The other new impeller featured a 2-blade design with a far more aggressive pitch angle and blade height relative to the 3-blade impeller. These new impellers would be compared to the performance of the 3-blade impeller to determine the optimal impeller choice. Further details regarding the design of the jet ski and 3-blade impellers can be found in Section 9.3 of this report.

9.2 Propulsion Module Design

9.2.1 Design Modifications

Minor design alterations were made to the design of the Final Prototype's propulsion module component relative to Prototype V2's propulsion module

component. Figures 9.1, 9.2, and 9.3 display side by side comparisons of the Final Prototype versus Prototype V2.

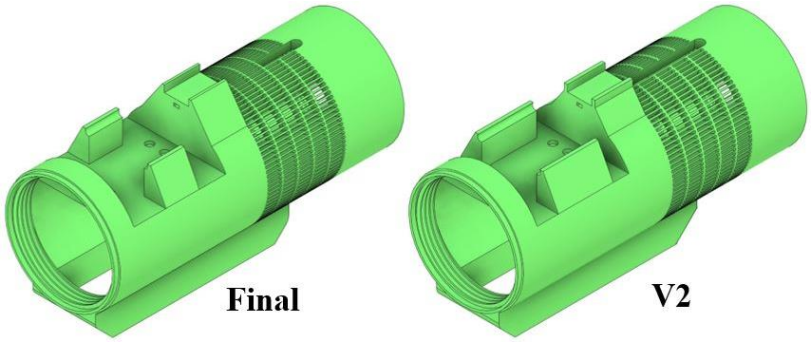

Figure 9.1: Final Prototype vs Prototype V2 Isometric Comparison

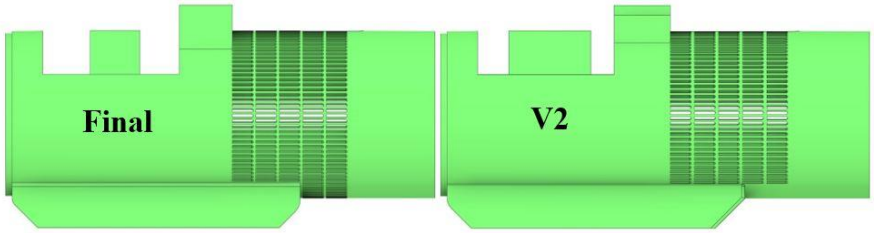

Figure 9.2: Final Prototype vs Prototype V2 Side Comparison

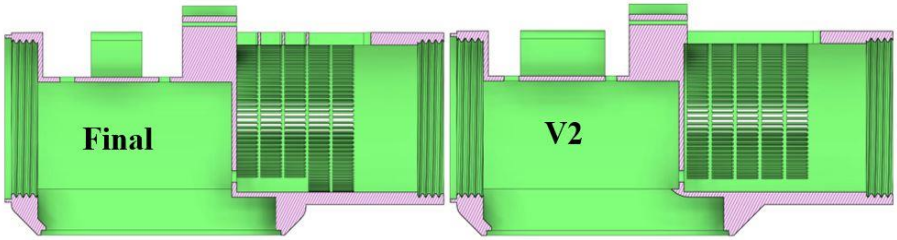

Figure 9.3: Final Prototype vs Prototype V2 Section View Comparison

Increasing the number of intake slits represented the primary design change of the Final Prototype. The two rows of slits closest to the nozzle now circled the entire diameter of the module, increasing the total surface area of the intake. The battery compartment was shortened from 185.5 mm to 179.2 mm to make room for this. As

all Prototype V2 testing was completed with the modified intake, it was unknown if the mesh geometry intake would function as designed. Increasing the surface area of the intake should help replicate the performance of the modified intake from Prototype V2. The Final Prototype's intake was also receded 2 mm such that the intake starts directly at the wall separating the electronics housing from the waterjet channel. The allen key slot was shortened and repositioned to sit directly above the shaft coupler. A comparison between intake specifications of the Final Prototype and Prototype V2 is shown in Table 9.1 below.

Table 9.1: Final Prototype vs Prototype V2 Intake Specifications

	Prototype V2	Final Prototype
Intake Length (mm)	73.0	71.4
Number of Rows	5	5
Slits Per Row	76	79 (3 rows), 96 (2 rows)
Total Number of Slits	380	429
Slit Surface Area (mm^2)	25.571	25.571
Allen Key Slit Surface Area (mm^2)	539.089	345.812
Total Intake Surface Area (mm^2)	10255.992	11315.771
Slit Volume (mm^3)	191.781	191.781
Allen Key Slit Volume (mm^3)	4043.168	2593.590
Total Intake Volume (mm^3)	76919.937	84867.639

The redesigned intake on the Final Prototype increased both total surface area and volume by 10.33% relative to Prototype V2.

Small dimensional adjustments were made to the ESC mount on the Final Prototype. The symmetrical support structures were decreased in length from 51 mm to 31 mm to gain better access to the wiring holes when sealing them with silicone.

The radius of the rails at the top of the structures that hold the ESC in place was decreased from 5 mm to 3.25 mm for a tighter fit.

The geometry of the lever arm mount was also tweaked slightly. The horizontal support pillars at the top of the mount were conjoined with the base of the mount, increasing strength and durability.

9.2.2 Assembly V1 COG and Buoyancy Analysis

The first round of testing with the Final Prototype was to be conducted using the existing single-channel versions of Nozzle V2. Because of this, the initial center of gravity and buoyancy analysis was completed with the 65 mm diameter outlet Nozzle V2 attached to Assembly V1. The impeller and driveshaft were also not included in this initial calculation as the final impeller had yet to be decided. Like Prototype V2, the center of gravity and buoyancy of the Final Module was first calculated without ballast. The total length (Y-axis) of the Final Prototype assembly in this configuration was 365.0 mm and the maximum height was 138.5 mm (X-axis). A list of all components and their masses included in this assembly and the calculated center point of the assembly are organized in Tables 9.2 and 9.3 respectively. A CAD rendering displaying the datum and calculated center point is displayed in Figure 9.4 on the following page.

Table 9.2: Final Prototype Assembly V1 Component Mass (No Ballast)

Component	Mass (g)
Final Propulsion Module	448.20
Nozzle V2 65 mm D	66.24
Waterproof Cap	177.39
3200 mAh LiPo Battery	216.71
DYS 3548-4 Brushless Motor	160.99
150 A Waterproof ESC	188.45
Shaft Connector	5.50
Brushless Motor Mount Bracket	10.60
146x54 mm Aluminum Sheet	8.24
Nozzle V2 65 mm D Water	206.20
Waterjet Channel Water	831.31
Total Mass (g)	2319.82

Table 9.3: Calculated Center Point of Final Prototype Assembly V1

Final Prototype Midpoint		
X (mm)	Y (mm)	Z (mm)
1.250	87.500	0.000

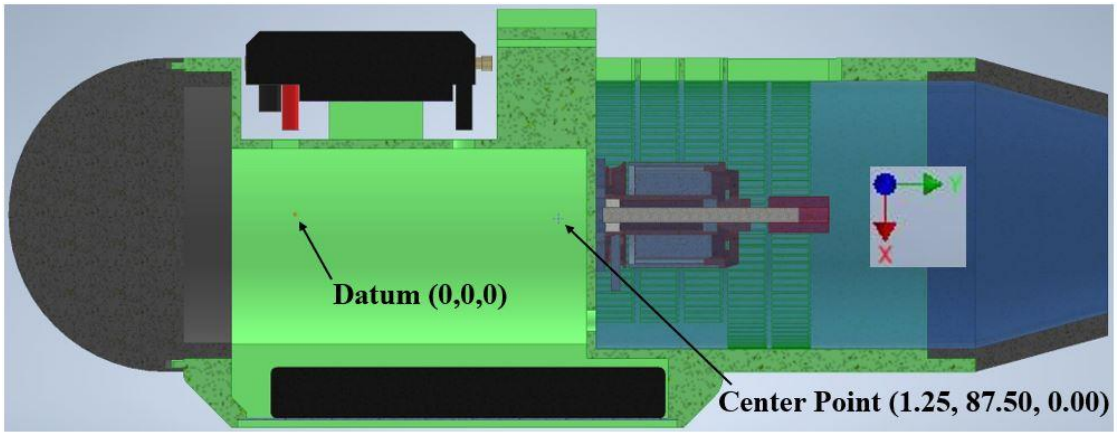

Figure 9.4: Final Prototype Assembly V1 with Datum and Center Point

Without water, the total mass of the Final Prototype was 1282.32 g. The additional 1037.51 g of water mass brought the total mass of Assembly V1 to 2319.82 g. Using the same methodology from Section 8.3, the Final Prototype's center of gravity relative to its midpoint was calculated. The center of gravity and delta to midpoint values for Assembly V1 without ballast are displayed in Table 9.4. The location of the center of gravity on the assembly is shown in Figure 9.5.

Table 9.4: Final Prototype Assembly V1 (No Ballast) Center of Gravity and Deltas

Center of Gravity (No Ballast)				
X (mm)	**X Delta from Midpoint (mm)**	**Y (mm)**	**Y Delta from Midpoint (mm)**	**Z (mm)**
1.843	0.593	117.866	30.366	0.000

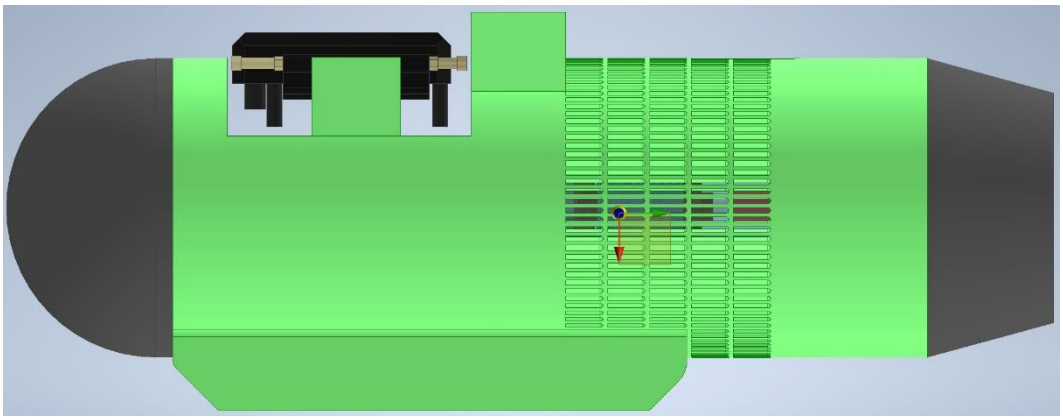

Figure 9.5: Final Prototype Assembly V1 (No Ballast) Center of Gravity Location

The X delta between the center of gravity and midpoint was only 0.593 mm, with the center of gravity slightly below the midpoint of the module. The Y delta was much larger at 30.366 mm as the center of gravity was further towards the rear of the module (nozzle) than the midpoint. Ballast would be required to locate the Final Prototype's center of gravity at its midpoint, closer to the front of the module.

Buoyancy calculations were also completed using the same methodology from Section 8.3. Contrary to the buoyancy calculations for Prototype V2, the volume of water in the inner channel intake was now accounted for. The motor assembly volume only considered the volumes of the motor, motor mount bracket, and shaft coupler as a final impeller and driveshaft had yet to be determined. The various volumes used for buoyancy calculations and buoyancy force values for this assembly are organized in Tables 9.5 and 9.6, respectively.

Table 9.5: Final Prototype Assembly V1 (No Ballast) Volumes

iProperties Assembly Volume (mm^3)	2139212.478
Electronics Housing Cavity Volume (mm^3)	826466.984
Inner Channel Intake Volume (mm^3)	83572.443
Total Additional Volume (mm^3)	910039.427
Subtracted Motor Assembly Volume (mm^3)	25808.010
Assembly V1 (No Ballast) Final Volume (mm^3)	3023443.895

Table 9.6: Final Prototype Assembly V1 (No Ballast) Buoyancy Calculations

Buoyancy Analysis (No Ballast)				
Total Volume (m^3)	**Total Mass (kg)**	**Buoyancy Force (N)**	**Gravitational Force (N)**	**Force Delta (N)**
0.003023443895	2.319824	29.601	22.757	6.843

In its current configuration, the module would be positively buoyant, with a force delta of 6.843 N. Additional ballast will be required to increase the gravitational force of the module and drive the force delta closer to neutral buoyancy.

The eight 90 mm x 26 mm x 3.175 mm pieces of lead ballast from Prototype V2 were reused for the Final Prototype. The final ballast setup featured four of these rectangular pieces flanking each side of the battery compartment, positioned as close

to the waterproof cap as possible. An 85 mm diameter piece of lead ballast, with a mass of 205.21 g, was secured to the inside face of the waterproof cap. A list of components and their masses, including the additional ballast, can be viewed in Table 9.7. A CAD model of the assembly with the final ballast setup is displayed in Figure 9.6.

Table 9.7: Final Prototype Assembly V1 Component Mass (With Ballast)

Component	Mass (g)
Final Propulsion Module	448.20
Nozzle V2 65 mm D	66.24
Waterproof Cap	177.39
3200 mAh LiPo Battery	216.71
DYS 3548-4 Brushless Motor	160.99
150 A Waterproof ESC	188.45
Shaft Connector	5.50
Brushless Motor Mount Bracket	10.60
146x54 mm Aluminum Sheet	8.24
Nozzle V2 65 mm D Water	206.20
Waterjet Channel Water	839.95
(8) 90x26 mm Ballast	705.44
85 mm D Ballast	205.21
Total Mass (g)	3239.11

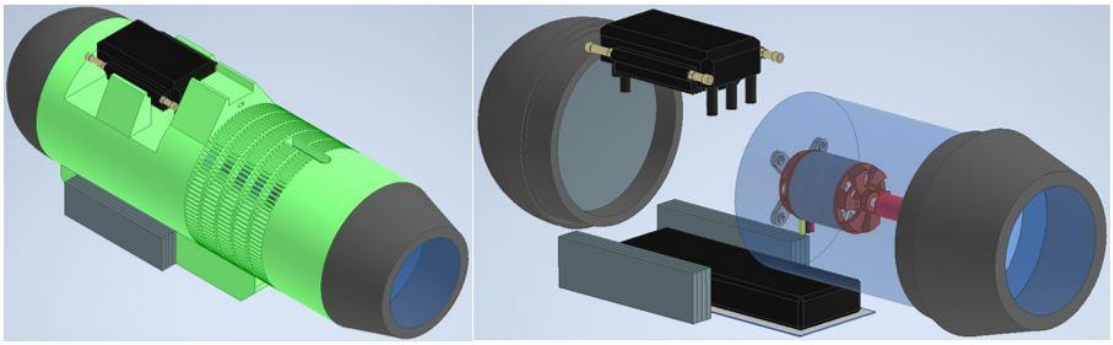

Figure 9.6: Final Prototype Ballast Setup

The lead ballast added a total of 910.65 g of mass to the assembly. The center of gravity and delta to midpoint values for Assembly V1 with ballast are displayed in Table 9.8. The location of the center of gravity on the assembly is shown in Figure 9.7.

Table 9.8: Final Prototype Assembly V1 (w/ Ballast) Center of Gravity and Deltas

Center of Gravity (Eight 90x26mm Ballast, One 85mm Diameter Ballast)				
X (mm)	X Delta from Midpoint (mm)	Y (mm)	Y Delta from Midpoint (mm)	Z (mm)
13.887	12.637	88.231	0.731	0.000

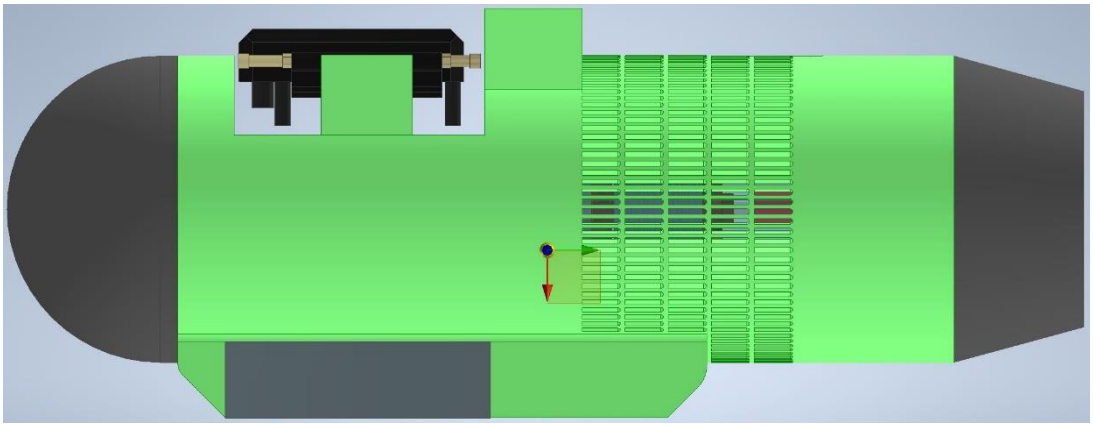

Figure 9.7: Final Prototype Assembly V1 (w/ Ballast) Center of Gravity Location

The X delta between the center of gravity and midpoint was 12.637 mm, moving the center of gravity well below the midpoint of the module. The Y delta shrunk to 0.731 mm, moving the center of gravity forward to the midpoint. Compared to the assembly without ballast, the center of gravity's X component was lowered by 12.044 mm and the Y component was nearly centered, moving forward by 29.635 mm. Buoyancy calculations for the assembly are organized in Table 9.9 on the following page.

Table 9.9: Final Prototype Assembly V1 (With Ballast) Buoyancy Calculations

Buoyancy Analysis (Eight 90x26mm Ballast, One 85mm Diameter Ballast)				
Total Volume (m^3)	Total Mass (kg)	Buoyancy Force (N)	Gravitational Force (N)	Force Delta (N)
0.003093058895	3.239114	30.282	31.776	-1.493

The additional 910.65 g of mass added by the lead ballast increased the gravitational force acting on the module by 9.019 N to 31.776 N. The buoyancy force of the module only increased by 0.681 N to 30.282 N, driving the force delta to -1.493 N, making the module negatively buoyant by a small margin.

9.3 New Impellers Design

Two new impellers were designed to optimize the Final Prototype's performance further. The design of the 3-blade impeller used in Prototype V2 featured a relatively fine blade pitch of 50 mm to reduce drag. This impeller would most likely be better suited operating in an outboard underwater environment. Both new impellers were designed with more aggressive blade pitches to test and compare their performance outputs to the 3-blade impeller. Initially, it was theorized that an impeller with an increased blade pitch would generate larger thrust values operating in the waterjet channel. Increased drag from the more aggressive blade pitch most likely would decrease the operational time of the module. However, it was still unknown how this modification would affect the module's efficiency operating in a ducted environment.

The first of the new impellers was heavily influenced by the design of modern jet ski impellers. This impeller was the most aggressive of the three impellers tested, featuring a three-blade design with a blade pitch of 87.5 mm and a cone-shaped hub.

Dimensional specifications and a CAD model of the jet ski impeller are displayed in Table 9.10 and Figure 9.8, respectively.

Table 9.10: Jet Ski Impeller Dimensional Specifications

Diameter (mm)	Hub Length (mm)	Front Hub Diameter (mm)	Rear Hub Diameter (mm)	Blade Pitch (mm)	Blade Height (mm)
84.250	45.000	11.033	31.625	87.500	32.409

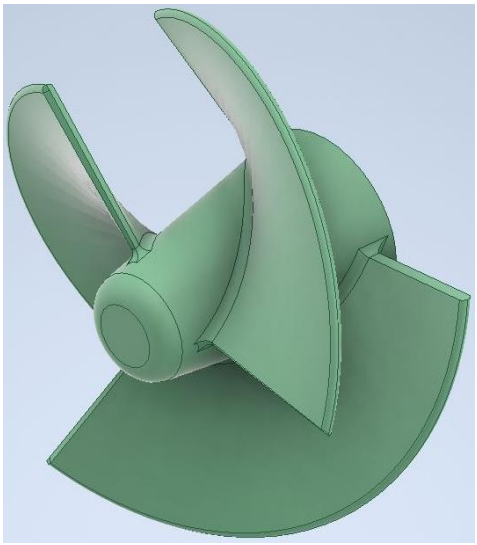

Figure 9.8: Jet Ski Impeller CAD Model

The second new impeller featured a two-blade design with a blade pitch of 66.5 mm. It was initially thought that this impeller would be the best performer of the three. The 2-blade impeller's pitch was less aggressive than the 87.5 mm pitch of the jet ski impeller but 16.5 mm larger than the 3-blade impeller. Subtracting a blade should help offset the additional drag introduced by the increased blade pitch relative to the 3-blade impeller. Dimensional specifications and a CAD model of the 2-blade impeller are displayed in Table 9.11 and Figure 9.9, respectively, on the following page.

Table 9.11: 2-Blade Impeller Dimensional Specifications

Diameter (mm)	Hub Length (mm)	Hub Diameter (mm)	Blade Pitch (mm)	Blade Height (mm)
85.000	44.605	17.000	66.500	27.300

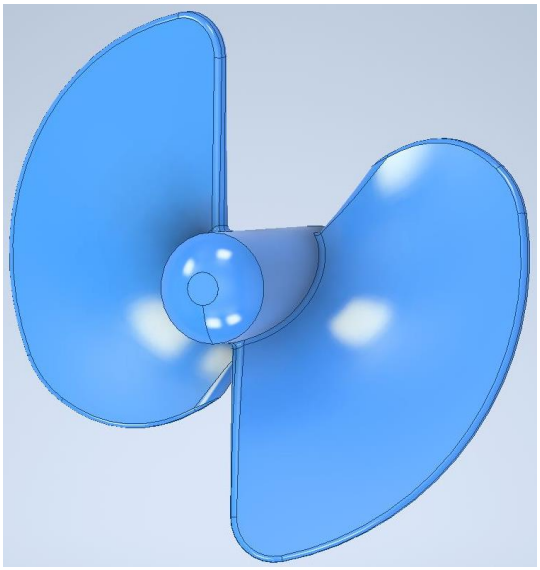

Figure 9.9: 2-Blade Impeller CAD Model

Both impellers were designed with hub lengths close to or equal to 45 mm. This allowed the impellers to be positioned as far away from the intake as possible, with the front of the impeller hub directly at the inlet of the nozzle.

The same CFD model described in Section 5.8 was used before physical testing to simulate and compare the theoretical performance of these impellers. The two impellers were simulated at a baseline rotational velocity of 1000 RPM over three seconds to compare the maximum flow velocity produced by each impeller. The Y-Z plane velocity contours for the jet ski and 2-blade impeller at t = 3 seconds are displayed in Figures 9.10 and 9.11, respectively, on the following page.

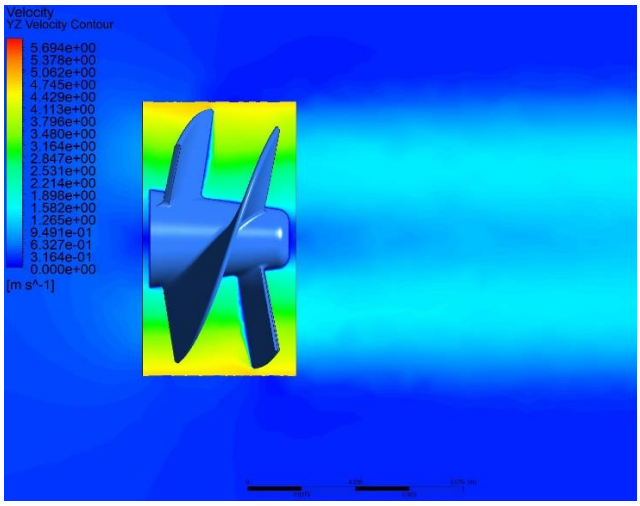

Figure 9.10: Jet Ski Impeller YZ-Plane Velocity Contour (t = 3s)

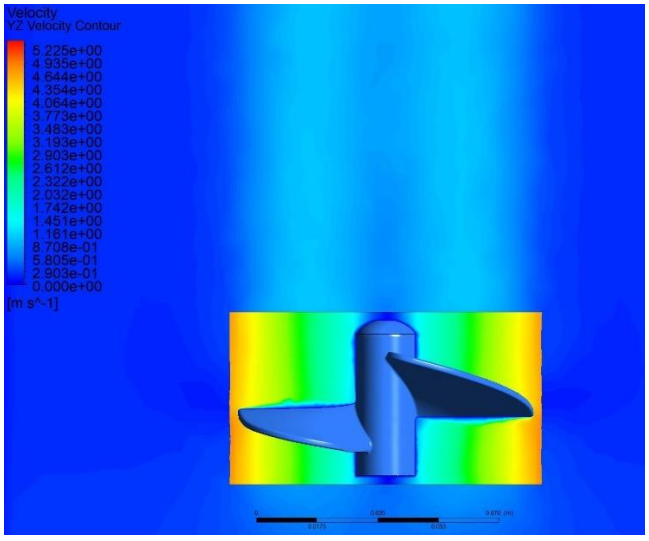

Figure 9.11: 2-Blade Impeller YZ-Plane Velocity Contour (t = 3s)

The maximum flow velocity produced by the jet ski impeller was 5.892 m/s, while the maximum flow velocity produced by the 4-blade impeller was 5.406 m/s. Relative to the 3-blade impeller simulation, the jet ski impeller's maximum flow velocity was 0.094 m/s larger, while the 2-blade's maximum flow velocity was 0.392 m/s smaller. Results from this simulation marginally favor the jet ski impeller over

the 3-blade impeller, with the 2-blade impeller lagging behind. However, this simulation does not replicate the ducted environment of the waterjet channel that the impeller will have to operate in. Physical testing would later confirm which impellers were the best choice for the propulsion module.

9.4 Initial Testing

Two stages of testing were planned for initial testing. The three impellers would first be tested on the Final Prototype without any nozzle attached. The best-performing impeller would then be carried over to the second stage of initial testing, where the different outlet diameter versions of Nozzle V2 would be tested. The best performing iteration of Nozzle V2 would then serve as the basis for dual-channel nozzle development.

Unfortunately, initial testing did not go according to plan. During the first testing stage, the 1100 KV DYS 3548-4 brushless motor experienced a critical failure and was replaced by the 790 KV DYS 3548-6 brushless motor. A shipping delay and the additional time spent installing the new motor significantly decreased the amount of time available for testing. Regardless, the 790 KV motor did prove to be the better choice of motor for this propulsion module.

9.4.1 Impeller Testing with 1100 KV Brushless Motor

Four different tests were scheduled for impeller testing. The 3-blade impeller was tested with a 31.65 mm and 47.65 mm driveshaft to analyze the effects of altering the location of the impeller within the waterjet channel. The 31.65 mm driveshaft positioned the back of the impeller directly at the end of the intake. The 47.65 mm

driveshaft positioned the front of the impeller directly at the inlet of the nozzle. Both the jet ski and 2-blade impeller were tested using driveshafts that positioned the front of the impellers directly at the inlet of the nozzle. Smaller driveshafts could not be used with these impellers as the clearance between the impeller and shaft connector was already minimized due to the larger hub lengths. Each test was run with the 1100 KV motor at 100% throttle for the duration of a single battery charge without a nozzle attached to the Final Prototype. Maximum and average thrust outputs, maximum LiPo battery temperatures, and operational run-times were recorded. Results from these tests are organized in Table 9.12 below.

Table 9.12: Final Prototype Impeller Test Results with 1100 KV Motor

Impeller	Driveshaft (mm)	Max Thrust (lbf)	Avg. Thrust (lbf)	Max Battery Temp (C)	Operational Time
3-Blade	31.650	7.13	6.25	72.0	2 min 34 sec
3-Blade	47.650	9.99	9.00	79.0	2 min 19 sec
2-Blade	27.045	11.97	10.75	77.9	2 min 7 sec
Jet Ski	26.650	12.21	11.00	70.2	1 min 38 sec

The 3-blade impeller with the 47.65 mm driveshaft produced a 40.11% larger maximum thrust output than the 3-blade impeller with the 31.65 mm driveshaft. This confirmed that positioning the impeller as far from the intake as possible at the inlet of the nozzle was the optimal setup for thrust performance. The maximum thrust output of the 2-blade impeller was 19.82% larger than the maximum thrust output of the 3-blade impeller with the 47.65 mm driveshaft.

The jet ski impeller produced the highest maximum thrust output of all the impellers tested, topping the 2-blade impeller by 2.01%. During this test, the motor ceased operating after 1 minute and 38 seconds. After further inspection, a bullet

connector on one of the motor wires had completely desoldered. At 22.7 g, the jet ski impeller was the heaviest of three impellers, with the 3-blade at 14.37 g and the 2-blade at 17.78 g. The additional rotational mass of the jet ski impeller increased the resistance in the electrical circuit, causing the motor wires to reach a critical temperature inducing the failure.

As expected, the 1100 KV brushless motor did not perform at the same level as the 900 KV brushless motor. Maximum battery temperatures were significantly higher for all four impeller tests than the temperatures recorded from Prototype V2 testing. Even without a nozzle attached, operational times also decreased from Prototype V2 testing.

9.4.2 Impeller Testing with 790 KV Brushless Motor

Impeller testing was repeated with the new 790 KV brushless motor installed to compare results from the previous round of testing and identify the optimal impeller choice for the propulsion module. Results from this iteration of impeller testing are organized in Table 9.13 below.

Table 9.13: Final Prototype Impeller Test Results with 790 KV Motor

Impeller	Driveshaft (mm)	Max Thrust (lbf)	Avg. Thrust (lbf)	Max Battery Temp (C)	Operational Time
3-Blade	31.650	11.17	9.75	75.2	3 min 4 sec
3-Blade	47.650	6.53	6.00	44.6	2 min 4 sec
2-Blade	27.045	13.86	12.50	68.1	3 min 26 sec
Jet Ski	26.650	12.34	11.25	42.3	1 min 12 sec

A high-pitched noise and significant performance loss were present when testing the 3-blade impeller with the 47.65 mm driveshaft, leading to a prudent motor shut down. No damage or interference was detected after a thorough inspection of the

module. This test with the same impeller and driveshaft was repeated, but the noise and performance loss remained. No other impeller and driveshaft setup experienced this issue. The jet ski test was also manually cut short for precautionary reasons due to a spike in battery temperature.

The 3-blade impeller with the 31.65 mm driveshaft and the 2-blade impeller experienced performance increases in almost every recorded parameter relative to the 1100 KV motor results. The maximum thrust output and operational time of the 3-blade impeller with the 31.65 mm driveshaft increased by 56.66% and 20.00%, respectively. However, the maximum battery temperature increased by 4.44% for this setup. Performance across the board was improved with the 2-blade impeller. The impeller's maximum thrust output increased by 15.79%, and the maximum battery temperature decreased by 12.58% despite the operational run-time increasing by 62.20%. Relative to the 3-blade impeller with the 31.65 mm driveshaft, the 2-blade impeller had a 24.08% larger maximum thrust output, 11.96% increase in operational run-time and a 9.44% reduction in maximum battery temperature.

The 2-blade impeller was chosen as the primary propulsion module impeller used for the remainder of Final Prototype testing. Results from this round of testing confirmed that the 790 KV brushless motor was the best choice for the propulsion module. The motor's additional torque and lower RPM power curve allowed it to produce increased thrust values and operational run-times without thermally overloading the battery.

9.4.3 Nozzle V2 Testing

After determining the optimal impeller for the module, the Final Prototype was tested with different variations of Nozzle V2 to identify the best performing single-channel nozzle. A 62.5 mm outlet diameter version of Nozzle V2 was manufactured to test along with the existing 70 mm, 65 mm, and 60 mm outlet diameter single-channel nozzles. Similar to impeller testing, each test was run with the 790 KV motor at 100% throttle for the duration of a single battery charge, this time with a nozzle attached to the module. Maximum and average thrust outputs, maximum LiPo battery temperatures, and operational run-times were recorded. Results from these tests are organized in Table 9.14 below.

Table 9.14: Final Prototype Nozzle V2 Test Results

Nozzle	Max Thrust (lbf)	Avg. Thrust (lbf)	Max Battery Temp (C)	Operational Time
V2 70 mm	15.64	14.50	71.9	2 min 57 sec
V2 65 mm	14.63	13.25	74.9	2 min 47 sec
V2 62.5 mm	12.37	11.00	80.5	2 min 28 sec

The 70 mm outlet diameter nozzle performed the best in all recorded parameters with a 14.78% advantage in maximum thrust output, 5.99% increase in operational run-time, and 4.02% reduction in maximum battery temperature compared to the 65 mm outlet diameter nozzle. Because of its performance in testing, this nozzle was chosen as the basis for dual-channel nozzle development. The 62.5 mm outlet diameter nozzle was the worst performer of the three, generating reduced performance numbers across all measurements. The 60 mm, outlet diameter version of Nozzle V2 was omitted from testing due to the extreme maximum battery temperature produced with the 62.5 mm outlet diameter nozzle.

9.5 Dual-Channel Nozzle

9.5.1 Design

The dual-channel nozzle design was based on the single-channel 70 mm outlet diameter Nozzle V2, the best performing nozzle from the previous round of testing. A total of four different dual-channel nozzles were manufactured for testing. All nozzles shared the same design methodology but differed in overlap distance between the outer and inner channels. Keeping the overall design methodology stagnant made the nozzle's overlap the only variable to be evaluated and analyzed during testing. A CAD model and cross-sectional view with labeled dimensions of the dual-channel nozzle with 0 mm of overlap are displayed in Figures 9.12 and 9.13, respectively.

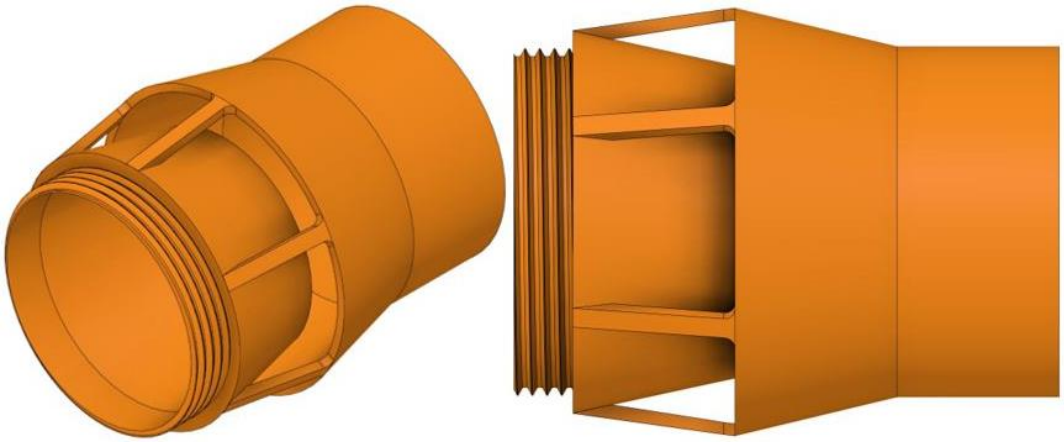

Figure 9.12: Dual-Channel Nozzle (0 mm Overlap) CAD Model

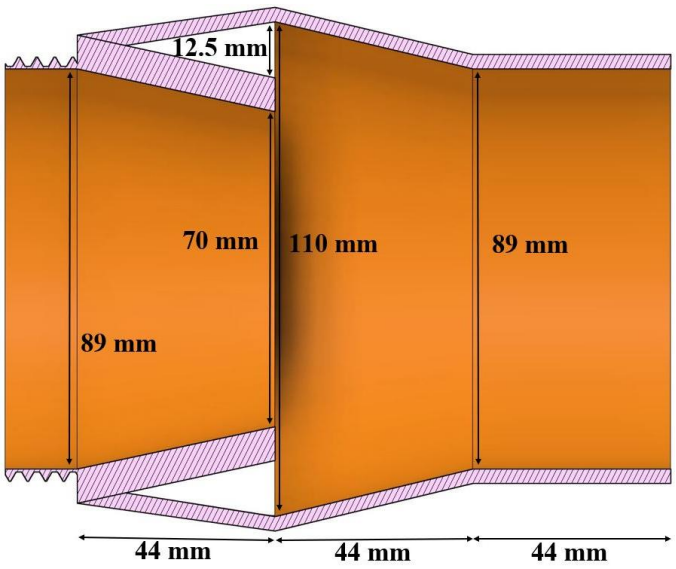

Figure 9.13: Dual-Channel Nozzle (0 mm Overlap) Cross-Section Dimensions

Attached to the outlet of the inner nozzle was a 16 mm long M95x4 exterior thread to connect the dual-channel nozzle to the waterjet channel of the Final Prototype. The inner channel shared the exact dimensions of the 70 mm outlet diameter version of Nozzle V2, while the outer channel comprised two sections: a conical inlet section and a cylindrical outlet section. Both sections were the same length as the inner channel at 44 mm each. The cylindrical outlet section's diameter was set to 89 mm to mirror the inlet diameter of the inner channel. The difference between the outer channel's inlet and outlet diameter was 21 mm, slightly larger than the 19 mm difference between the inner channel's inlet and outlet diameter.

Six rectangular support pillars connected the inner channel to the outer channel. These pillars differed in length based on the length of overlap between inner and outer channels. In addition to the 0 mm overlap dual-channel nozzle displayed on the previous page, a 15 mm, 30 mm, and -15 mm overlap versions were created.

Overlap was defined as the length at which the outer channel engulfs the inner channel. The -15 mm overlap refers to the outer channel extending away from the inner channel by 15 mm, rather than overlapping it. Specifications for these nozzles are organized in Table 9.15 below.

Table 9.15: Dual-Channel Nozzle Specifications

Overlap (mm)	Length (mm)	Overlap Inlet Diameter (mm)	Internal Volume (mm^3)
-15	147	12.425	617128.178
0	132	12.500	617128.178
15	117	9.053	518379.768
30	102	5.887	419631.358

The overlap inlet diameter refers to the distance between the inner diameter of the outer channel to the outer wall of the inner channel (see 12.5 mm gap displayed in Figure 9.13). This section of the dual-channel nozzle is where additional fluid from the environment enters the outer channel to later conjoin with energized fluid exiting the inner channel. An increase in channel overlap above 0 mm leads to a decrease in overlap inlet diameter, decreasing the fluid volume that could enter this section. A smaller overlap inlet diameter could prove beneficial, as the decreased surface area of the overlap inlet could increase the fluid's velocity entering the outer channel from the external environment. Figure 9.14 on the following page displays the four dual-channel nozzles, with the 30 mm, 15 mm, 0 mm, and -15 mm overlap versions pictured from left to right.

Figure 9.14: Final Dual-Channel Nozzles

A CFD model was developed to evaluate the theoretical performance differences between the four dual-channel nozzles. Physical testing of the nozzles would be conducted with the Final Prototype mounted to the static testing apparatus. Because of this, the model was designed to simulate the performance of the dual-channel nozzle with a forward velocity equal to 0. Any fluid entering through the overlap inlet would solely be due to the low-pressure zone created by the flow of energized fluid exiting the inner channel outlet. The CFD model's geometry, mesh, and simulation parameters are organized into Tables 9.16, 9.17, and 9.18, respectively. The -15 mm overlap model's geometry can be viewed in Figure 9.15 on the following page.

Table 9.16: Dual-Channel Nozzle CFD Model Geometry Parameters

Geometry Parameter	Value
Cylinder	r = 150 mm, Varying Length (Based on Overlap)
Boolean 1	Subtract, Target = Fluid Domain, Tool = Dual-Channel Nozzle, Preserve
Parts	Dual-Channel Nozzle, Fluid Domain

Table 9.17: Dual-Channel Nozzle CFD Model Mesh Parameters

Mesh Parameter	Value
Element Size (mm)	5.0
Max Element Size (mm)	5.0
Defeaturing	On
Capture Curvature	On
Capture Proximity	On
Smoothing	High

Table 9.18: Dual-Channel Nozzle CFD Model Simulation Parameters

Simulation Parameter	Value
Solution	Steady
Model	k-ε, Scalable, Realizable
Boundary Conditions	Inlet 1 = 2.5 m/s, Inlet 2 = 0 m/s, 2 Pressure Outlets
Methods	Coupled, Least Squares, Second Order All
Convergence Criteria	10^{-6}
Iterations	1000

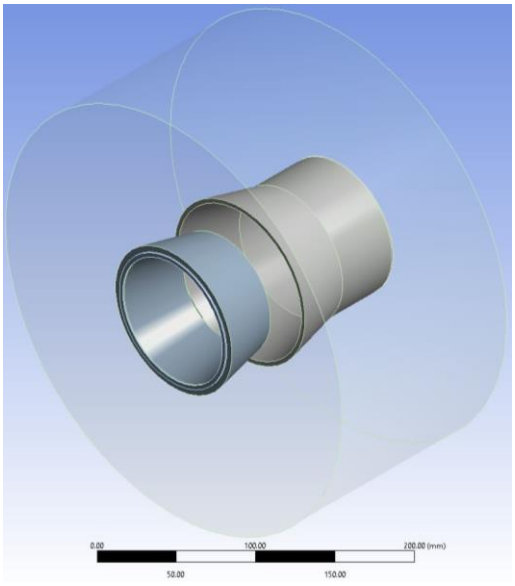

Figure 9.15: -15 mm Overlap Dual-Channel Nozzle CFD Model Geometry

Inlet 1 refers to the inlet of the inner channel nozzle. The inlet velocity of this boundary condition was set to 2.5 m/s to simulate a flow of energized fluid exiting the waterjet channel and entering the inner channel of the nozzle. Inlet 2 refers to the face of the fluid domain surrounding Inlet 1. The inlet velocity of this boundary condition was set to 0 m/s to replicate the static environment that the nozzles will be physically tested in. Average outlet velocities and thrust values were calculated at Outlet 1, referring to the outlet of the outer channel. Results from the simulations are organized in Table 9.19 below. YZ-plane velocity contours and vectors for the -15 mm overlap dual-channel nozzle are displayed in Figures 9.16 and 9.17, respectively.

Table 9.19: Dual-Channel Nozzle CFD Simulation Results

Overlap (mm)	Avg. Outlet Velocity (m/s)	Outlet Thrust (N)	Outlet Thrust (lbf)
-15	2.983	70.909	15.941
0	2.923	69.330	15.586
15	2.856	68.723	15.450
30	2.821	68.284	15.351

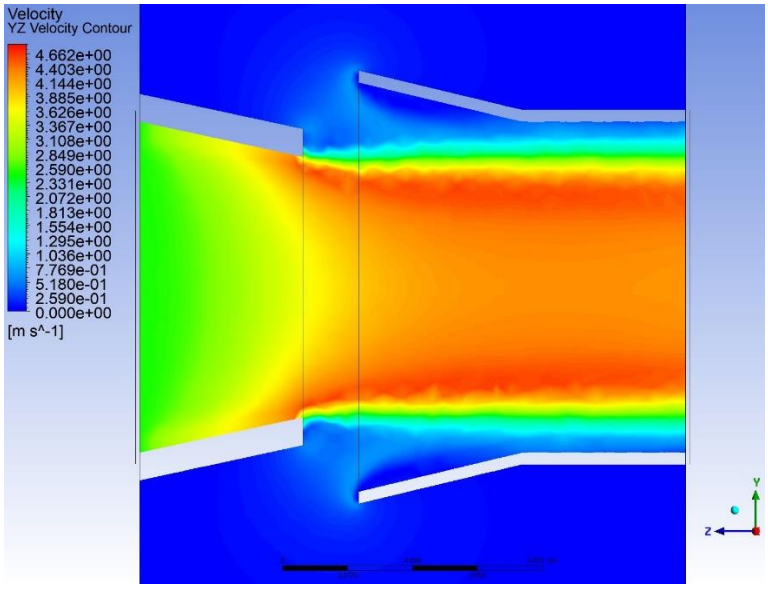

Figure 9.16: -15 mm Overlap Dual-Channel Nozzle YZ-Plane Velocity Contours

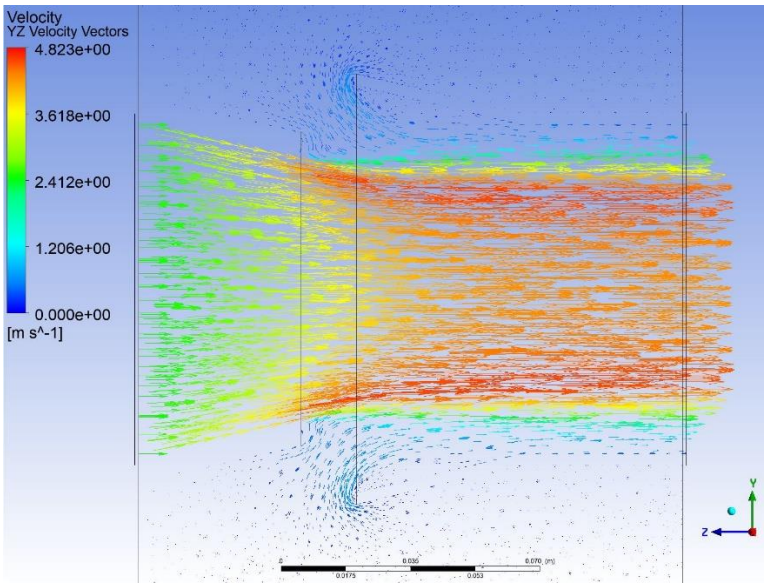

Figure 9.17: -15 mm Overlap Dual-Channel Nozzle YZ-Plane Velocity Vectors

Simulation results suggested that larger overlap distances would negatively affect the performance of the nozzle when the propulsion module has a forward velocity equal to 0. The -15 mm overlap dual-channel nozzle yielded the best simulation results by a small margin. Relative to the worst-performing 30 mm overlap nozzle, the -15 mm overlap nozzle produced a 5.74% higher average outlet velocity and held a 3.84% advantage in outlet thrust. The intended suction effect created by the dual-channel design can be viewed in Figures 9.16 and 9.17. Static water surrounding the nozzle is drawn in through the overlap intake and conjoined with the energized fluid exiting the inner channel outlet.

9.5.2 Final Testing

Despite the previous simulations, it was still largely unknown which of the four nozzles would perform the best when physically tested with the Final Prototype. Results from testing the 70 mm outlet diameter version of Nozzle V2 with the Final

Prototype would serve as a useful comparison to determine if the innovative dual-channel nozzle design improved performance relative to the single-channel nozzle.

A total of four tests were completed, one with each of the dual-channel nozzles attached to the Final Prototype. Each test was run with the motor at 100% throttle for a single battery charge duration. The 2-blade impeller was used for all four tests. Maximum and average thrust outputs, maximum LiPo battery temperatures, and operational run-times were recorded. Results from these tests are organized in Table 9.20 below and displayed graphically in Figures 9.18, 9.19, and 9.20.

Table 9.20: Final Prototype Dual-Channel Nozzle Testing Results

Nozzle	Max Thrust (lbf)	Avg. Thrust (lbf)	Max Battery Temp (C)	Operational Time
15 mm Extension	14.53	13.50	72.9	3 min 3 sec
0 mm Overlap	15.32	14.25	74.1	2 min 59 sec
15 mm Overlap	15.89	14.75	78.0	2 min 52 sec
30 mm Overlap	16.93	15.75	77.3	2 min 49 sec

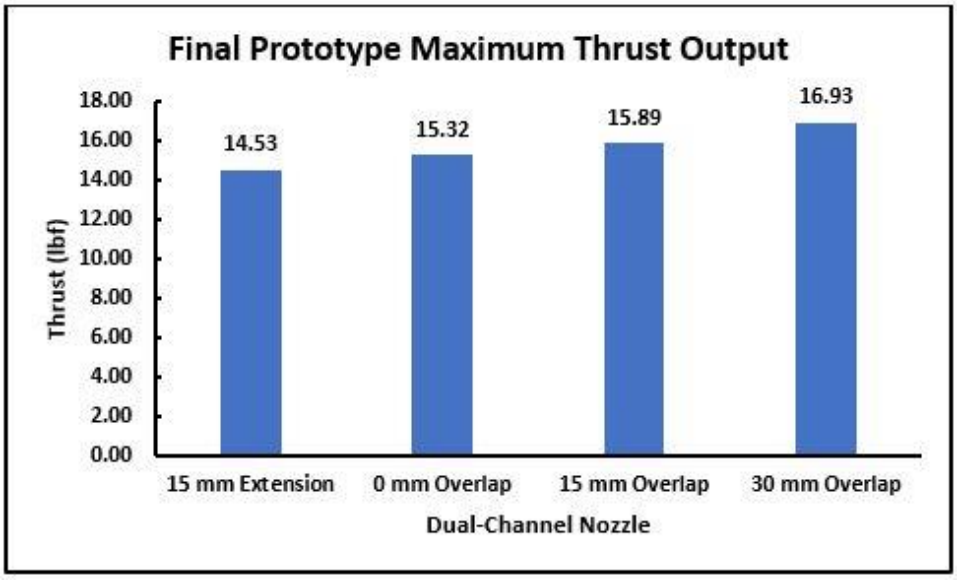

Figure 9.18: Final Prototype Maximum Thrust Output

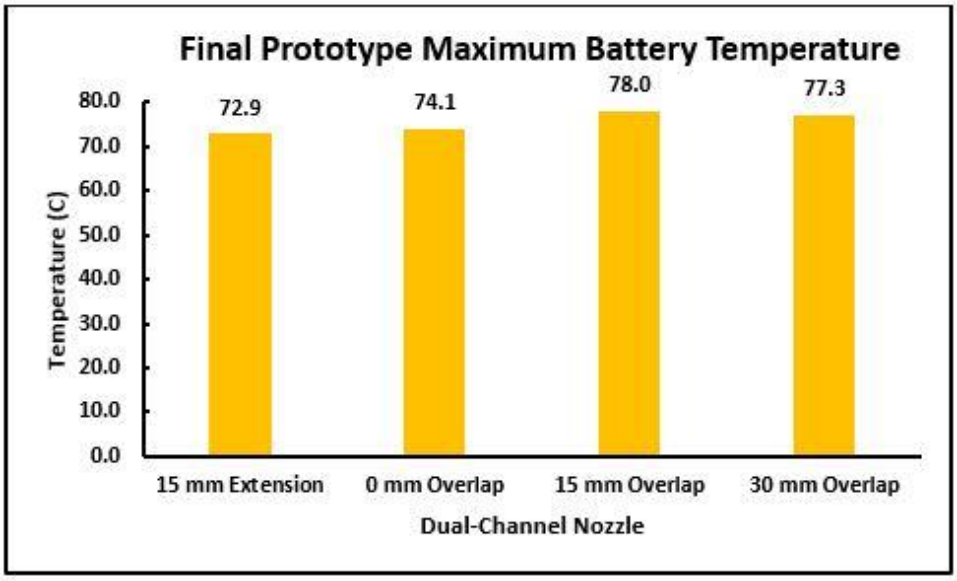

Figure 9.19: Final Prototype Maximum LiPo Battery Temperature

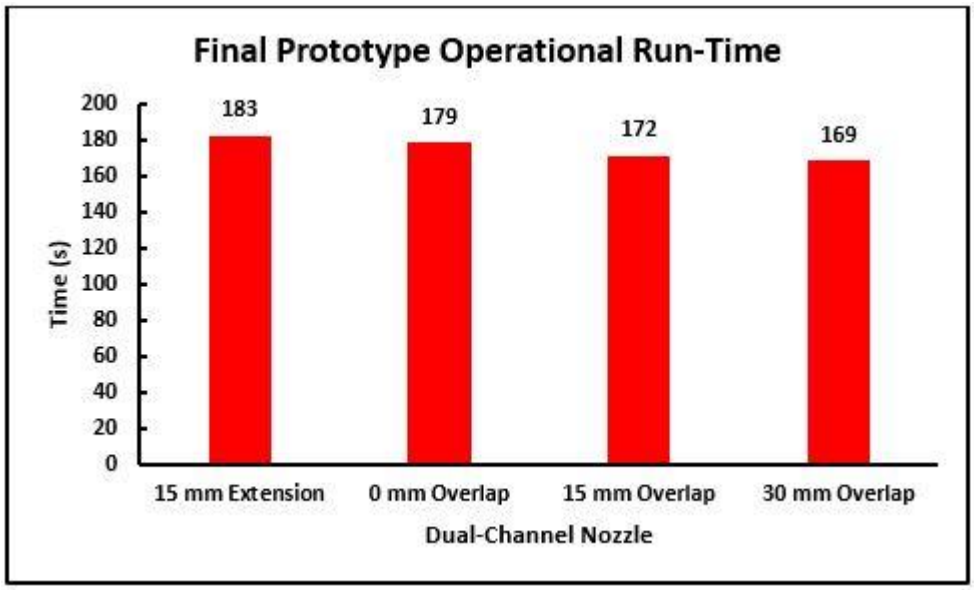

Figure 9.20: Final Prototype Operational Run-Time

The Final Prototype's thrust output increased as the dual-channel nozzle's overlap distance increased. The 30 mm overlap dual-channel nozzle produced the highest maximum thrust output of 16.93 lbf, 6.54% larger than the second-best

performing 15 mm overlap nozzle. This maximum thrust output was also a 16.52% improvement over the -15 mm (15 mm extension) dual-channel nozzle, which produced the highest simulated thrust values. The 30 mm overlap dual-channel nozzle attached to the Final Prototype can be viewed in Figure 9.21 below.

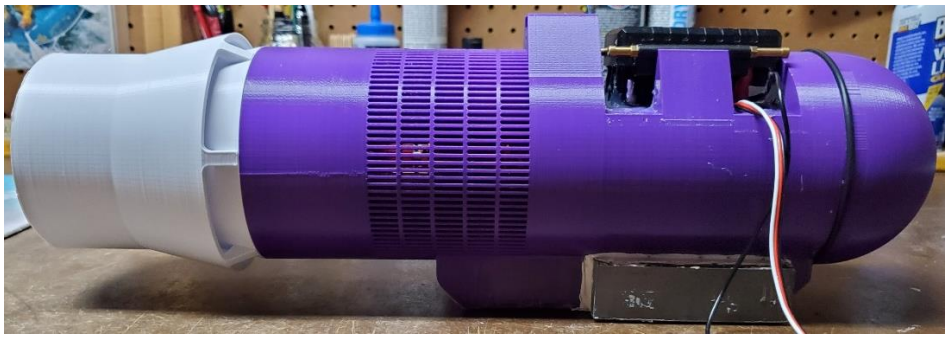

Figure 9.21: Final Prototype with 30 mm Overlap Dual-Channel Nozzle

Maximum LiPo battery temperature increased as the dual-channel nozzle's overlap distance increased. The 15 mm overlap dual-channel nozzle posted the highest maximum battery temperature of 78.0 C, only 0.91% larger than the maximum battery temperature experienced with the 30 mm overlap nozzle. Relative to the -15 mm overlap dual-channel nozzle, the 30 mm overlap nozzle recorded a 6.04% higher maximum battery temperature.

The Final Prototype's operational run-time decreased as overlap distance and thrust increased. With the 30 mm overlap dual-channel nozzle attached, the operation run-time of the propulsion module was 169 seconds. This was a 7.65% decrease relative to the run-time of the module with the -15 mm overlap nozzle attached.

Referring to the Final Prototype testing results with the single-channel 70 mm outlet diameter version of Nozzle V2 (Table 9.14), the 30 mm overlap dual-channel

nozzle improved maximum thrust output by 8.25%. The 15 mm overlap nozzle was the only other dual-channel nozzle tested that increased maximum thrust output relative to the single-channel version, with a marginal increase of 1.60%. The 0 mm and -15 mm overlap dual-channel nozzles failed to beat the 15.64 lbf maximum thrust output of the 70 mm outlet diameter version of Nozzle V2.

Results from physical testing contradicted the results obtained from CFD simulation, likely due to the dynamic and environmental factors not accounted for in the model. Although the module was mounted to a static testing apparatus, the flow field in the test tub surrounding the module was not perfectly static as in the CFD model. During testing, energized water exiting the module would collide with the tub's inner wall and disperse throughout the tub, creating a significant amount of turbulence around the module. It is unclear whether this provided any performance benefits for the dual-channel nozzles with increased overlaps. Turbulent flow fields around the module could have disturbed the module's operation and efficiency, decreasing performance. On the other hand, it is possible the "suction" effect created by the dual-channel nozzle experienced an increase in performance due to the surrounding high-velocity fluid entering through the overlap inlet and conjoining with the energized fluid exiting the inner channel of the nozzle.

9.5.3 Final Prototype Specifications

Specifications for the Final Prototype with the 30 mm overlap dual-channel nozzle are displayed in the figures and tables on the following two pages.

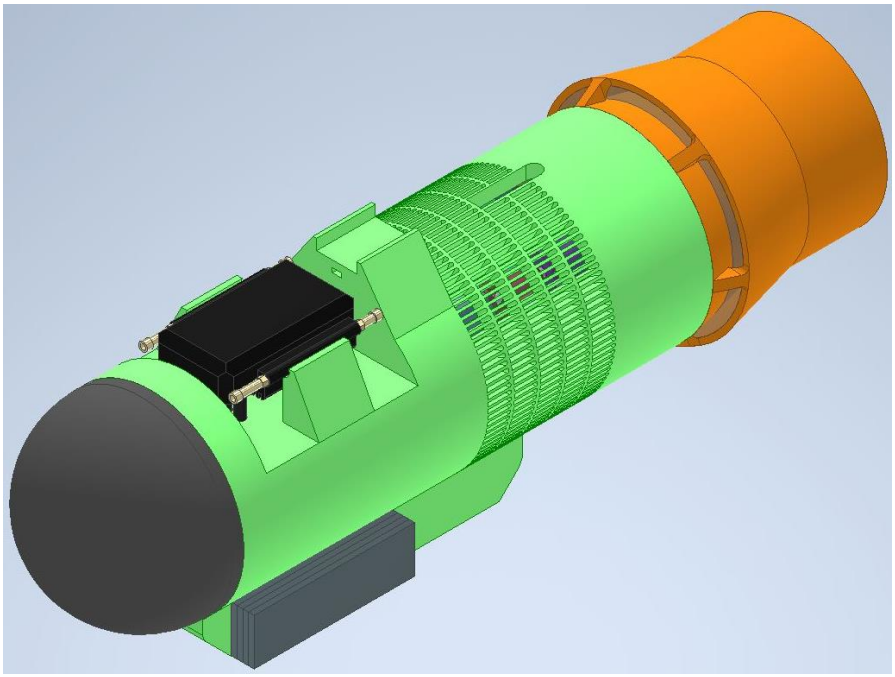

Figure 9.22: Final Prototype CAD Assembly

Table 9.21: Final Prototype Component Mass

Component	Mass (g)
Final Propulsion Module	448.20
Dual-Channel Nozzle 70 mm D 30 mm Overlap	162.10
Waterproof Cap	177.39
3200 mAh LiPo Battery	216.71
DYS 3548-4 Brushless Motor	160.99
150 A Waterproof ESC	188.45
Shaft Connector	5.50
Brushless Motor Mount Bracket	10.60
2-Blade Impeller	17.78
27.045 mm Driveshaft	3.69
146x54 mm Aluminum Sheet	8.24
Dual-Channel Nozzle 70 mm D 30 mm Overlap Water	638.00
Waterjet Channel Water	839.95
(8) 90x26 mm Ballast	705.44
85 mm D Ballast	205.21
Total Mass (g)	3788.24

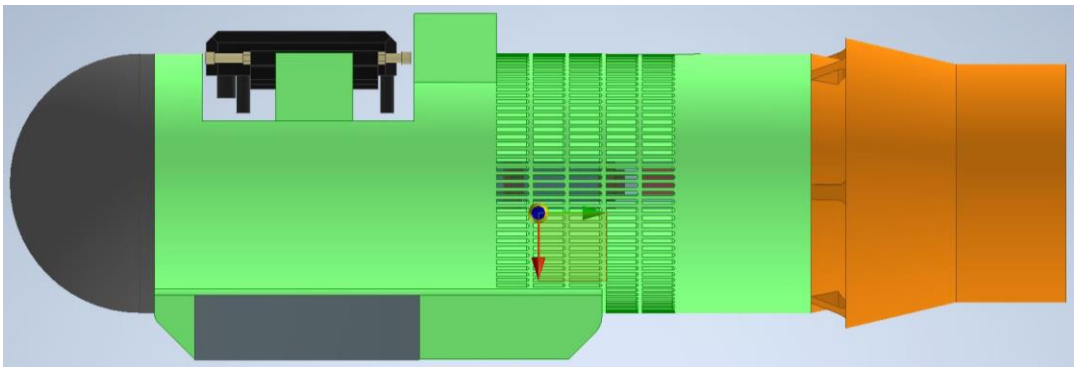

Figure 9.23: Final Prototype Center of Gravity Location

Table 9.22: Final Prototype Center of Gravity and Deltas

Center of Gravity (Final Prototype)				
X (mm)	**X Delta from Midpoint (mm)**	**Y (mm)**	**Y Delta from Midpoint (mm)**	**Z (mm)**
11.874	10.624	116.753	0.253	0.000

Table 9.23: Final Prototype Buoyancy Calculations

Buoyancy Analysis (Final Prototype)				
Total Volume (m^3)	**Total Mass (kg)**	**Buoyancy Force (N)**	**Gravitational Force (N)**	**Force Delta (N)**
0.003616450626	3.788243	35.406	37.163	-1.756

The design of the 30 mm overlap dual-channel nozzle allowed the same ballast configuration to be carried over from Assembly V1 without negatively impacting the center of gravity and buoyancy of the propulsion module.

10. Financial Analysis

10.1 Final Propulsion Module Prototype

A bill of materials displaying the cost of each item used to construct the Final Propulsion Module Prototype is shown in Table 10.1 below.

Table 10.1: Final Propulsion Module Prototype Bill of Materials

Final Propulsion Module Prototype Bill of Materials				
Item	**Unit**	**Quantity**	**Unit Cost**	**Cost**
eSun PLA+ 2.85mm	g	811.20	$0.02	$20.18
Ultimaker Breakaway White 2.85mm	g	273.20	$0.09	$25.48
Sheet Lead 1/8"	in^3	1.49	$2.06	$3.06
Flash Hobby D3548 790Kv Brushless Motor	Units	1.00	$20.99	$20.99
HOOVO 3S 11.1V 3200mAh 50C LiPo Battery	Units	1.00	$18.50	$18.50
uxcell 5mm to 5mm Shaft Coupler	Units	1.00	$3.75	$3.75
RilexAwhile 100mm x 5mm Stainless Steel Shaft	mm	27.05	$0.02	$0.57
146mm x 54mm x 0.5mm Aluminum Sheet	Units	1.00	$1.98	$1.98
FLYCOLOR Waterproof 150A ESC	Units	1.00	$59.99	$59.99
Apex RC 4mm Male/Female Gold Plated Bullet Connectors	Units	9.00	$0.50	$4.50
M3-0.5 x 8mm Stainless Steel Machine Screw	Units	4.00	$0.33	$1.32
M3-0.5 3mm Stainless Steel Hex Nut	Units	4.00	$0.23	$0.92
M3-0.5 3mm Stainless Steel Washer	Units	4.00	$0.09	$0.36
GE Advanced Silicone 2.8 FL OZ	Units	0.15	$6.99	$1.05
LOCTITE PL Marine Adhesive Sealant 3 FL OZ	Units	0.10	$9.98	$1.00
Amazing GOOP Marine Contact Adhesive and Sealant	Units	0.02	$8.59	$0.17
Flex Seal Liquid Rubber Sealant Coating 14 OZ	Units	0.01	$12.99	$0.13
Aluminum Repair Tape 10YD	Units	0.01	$4.99	$0.05
HiLetgo RC Servo Tester	Units	1.00	$2.83	$2.83
HONBAY 300mm Servo Extension Cable	Units	1.00	$0.73	$0.73
Total Cost				$167.55

A target cost of $100 was specified as a design specification in Section 2.1 for this propulsion module. The total cost of the Final Prototype was $167.55, missing the design specification by $67.55. The $100 target cost was initially put in place, assuming one of the provided motors would be used for the final propulsion module, eliminating the purchase cost of a motor. Unfortunately, the provided DYS 3548-5 brushless motor experienced a failure during testing and had to be replaced with a new

motor. The DYS 3548-6 motor used in the Final Prototype increased the total cost of the module by $20.99.

At $59.99, the FLYCOLOR Waterproof 150 A ESC was the most expensive component featured on the Final Prototype. The Electricparts.com 80 A ESC used for Prototype V1 was less expensive at $35.99 but was not suitable for this application due to thermal issues. Developing a cooling system for the 80 A ESC likely would have increased costs beyond the 150 A waterproof ESC price, making it a difficult component to replace.

The items listed in the bill of materials were broken down into five categories for further analysis. A pie chart displaying these categories and their respective costs is displayed in Figure 10.1 below.

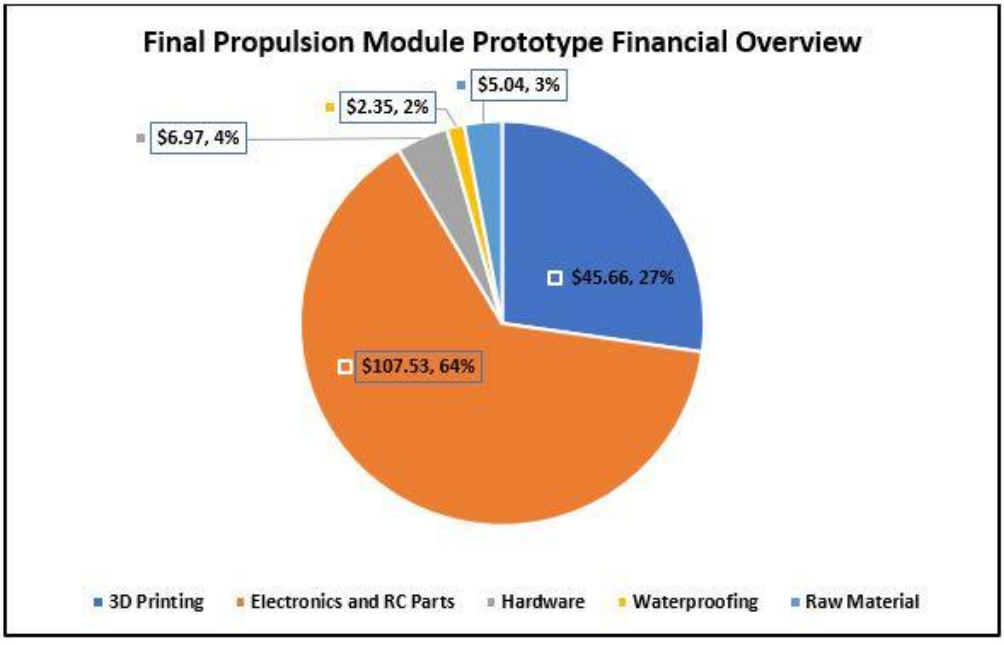

Figure 10.1: Final Propulsion Module Prototype Financial Overview

Electronics and RC Parts commanded 64.18% of the $167.55 spent on the Final Prototype, representing the largest piece of the module's total cost. The ESC, LiPo battery, and brushless motor were three of the most expensive items on the propulsion module, costing $99.48 in total. The remainder of the items grouped into this category consisted of the wires, electrical connectors, and servo controller necessary for propulsion module operation.

The total cost of the filament required to 3D print all the Final Prototype components was $45.66, representing 27.25% of the total cost of the module. Ultimaker Breakaway White support material made up 55.80% of this cost despite using 66.32% less of this filament than eSun PLA+. Much research and work went into minimizing the amount of support required for propulsion module components to prioritize reduced costs. Without Ultimaker Breakaway White, it would not have been possible to manufacture the primary propulsion module component.

Hardware, Waterproofing, and Raw Material made up the remaining $14.36 of the $167.55 total. These categories included approximately half of the total items used for the Final Prototype but only represented 8.57% of the total cost.

10.2 Overall Project

A bill of materials displaying the cost of each item purchased throughout the duration of this project is shown in Table 10.2 on the following page.

Table 10.2: Overall Project Bill of Materials

Overall Project Bill of Materials				
Item	**Unit**	**Quantity**	**Unit Cost**	**Cost**
eSun PLA+ 2.85mm	g	4768.70	$0.02	$118.65
Ultimaker Breakaway White 2.85mm	g	1438.40	$0.09	$134.15
Sheet Lead 1/8" x 12" x 12"	in^3	18.00	$2.06	$36.99
Flash Hobby D3548 790Kv Brushless Motor	Units	1.00	$20.99	$20.99
Flash Hobby D3548 1100Kv Brushless Motor	Units	1.00	$20.99	$20.99
HOOVO 3S 11.1V 3200mAh 50C LiPo Battery	Units	2.00	$18.50	$36.99
uxcell 5mm to 5mm Shaft Coupler	Units	2.00	$3.75	$7.49
RilexAwhile 100mm x 5mm Stainless Steel Shaft	mm	500.00	$0.02	$10.59
146mm x 54mm x 0.5mm Aluminum Sheet	Units	2.00	$1.98	$3.96
Electricparts.com RC 80A ESC	Units	1.00	$35.99	$35.99
FLYCOLOR Waterproof 150A ESC	Units	1.00	$59.99	$59.99
Apex RC 4mm Male/Female Gold Plated Bullet Connectors	Units	40.00	$0.50	$19.98
Electricparts.com RC ESC Programming Card	Units	1.00	$14.99	$14.99
Goolsky FLYCOLOR ESC Programming Card	Units	1.00	$15.99	$15.99
Donepart 5mm x 11mm x 4mm MR115-2RS Bearings	Units	20.00	$0.65	$12.98
16AWG 30CM 3.5mm Bullet Connector Extension Wire	Units	6.00	$1.67	$9.99
GE Advanced Silicone 2.8 FL OZ	Units	1.00	$6.99	$6.99
LOCTITE PL Marine Adhesive Sealant 3 FL OZ	Units	1.00	$9.98	$9.98
Amazing GOOP Marine Contact Adhesive and Sealant	Units	1.00	$8.59	$8.59
Flex Seal Liquid Rubber Sealant Coating 14 OZ	Units	1.00	$12.99	$12.99
Aluminum Repair Tape 10YD	Units	1.00	$4.99	$4.99
M3-0.5 x 8mm Stainless Steel Machine Screw	Units	16.00	$0.33	$5.28
M3-0.5 3mm Stainless Steel Hex Nut	Units	16.00	$0.23	$3.68
M3-0.5 3mm Stainless Steel Washer	Units	8.00	$0.09	$0.72
M2.5-0.45 x 8mm Stainless Steel Machine Screw	Units	8.00	$0.95	$7.60
Hobbypark XT60 Male to Female Adapter Connectors 10AWG	Units	2.00	$6.49	$12.98
2" x 4" x 96" Wood	Units	3.00	$3.35	$10.05
HiLetgo RC Servo Tester	Units	3.00	$2.83	$8.49
HONBAY 300mm Servo Extension Cable	Units	10.00	$0.73	$7.29
Total Cost				$660.34

The total cost of the project from start to finish was $660.34. This includes all items used to construct the testing apparatus and prototypes. The items listed in the bill of materials were broken down into five categories and displayed graphically in Figure 10.2 on the following page.

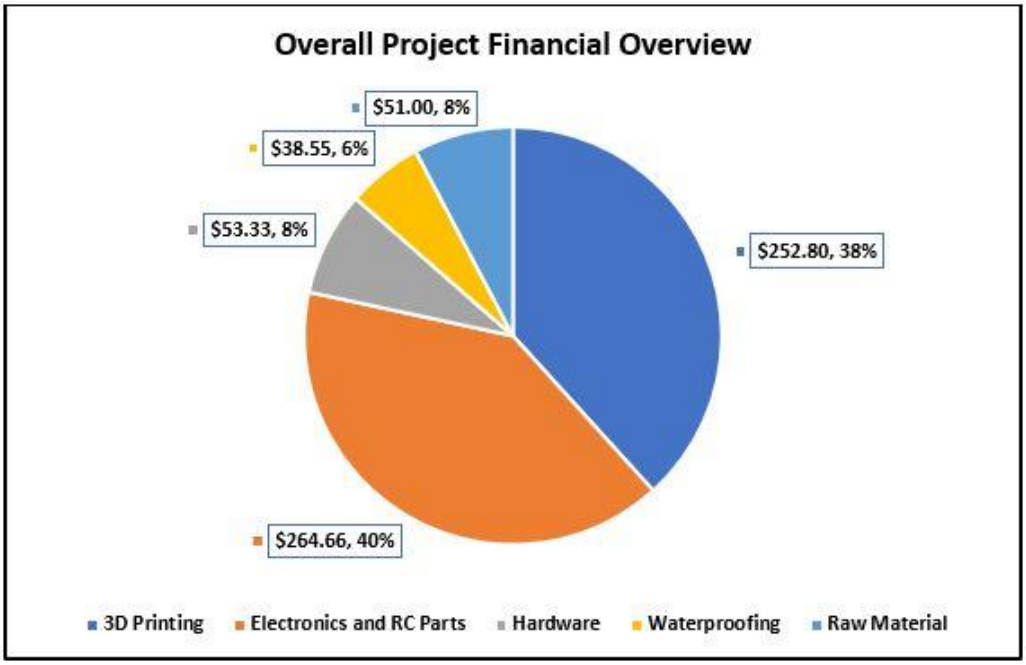

Figure 10.2: Overall Project Financial Overview

$264.66 was spent on Electronics and RC Parts, representing 40.08% of the project's total cost. The two brushless motors, two LiPo batteries, and two ESCs added up to $174.95, with the remaining $89.71 spent on extension wires, electrical connectors, and servo controllers. 3D Printing costs were not far behind Electronics and RC Parts, making up 38.28% of the project's total cost. A total of 6207.1 g of filament was used to manufacture the propulsion module prototypes and different component iterations. The Raw Material, Hardware, and Waterproofing categories represented the remaining 21.64% of the project's total cost.

11. Conclusion

Five of the seven design specifications created at the start of this project were successfully achieved by the Final Propulsion Module Prototype. The module met the desired length and diameter specifications, was solely constructed using additive manufacturing techniques, and featured a fully modular battery design. The Final Prototype achieved a maximum thrust of 16.93 lbf with the dual-channel nozzle attached, satisfying the 10-20 lbf requirement. The total cost of the module exceeded the $100 target cost by $67.55. This was partly due to the purchase of a replacement motor and the substantial cost of the waterproof ESC. The Final Prototype did not meet the operational run-time design specification of 30 minutes. To reach this goal, a significantly larger battery would have been required. This would have further increased the cost of the propulsion module, which was already well over budget. Instead of focusing on run-time, most propulsion module testing focused on maximizing thrust performance at full throttle.

All of the project objectives laid out in Section 1.2 were accomplished at project completion. Although more time was spent achieving a functional propulsion module than initially intended, an innovative dual-channel nozzle was eventually designed, manufactured, and tested. Several mechanical failures and design setbacks delayed the project's progress and limited the total time to test and develop the dual-channel nozzle. The results gathered from the final testing were promising and demonstrated the performance potential of the 30 mm overlap dual-channel nozzle. Further development and testing of the dual-channel nozzle concept will have to be completed to confirm the performance benefits of the design.

12. Future Work

This study's Final Prototype was primarily developed to serve as a functional propulsion module used to test the performance of the innovative dual-channel nozzle. The module operated successfully in this usage case. However, nearly every facet of the Final Prototype's design could be further optimized to increase performance and efficiency. Several design revisions were conceptualized throughout the development process but were never implemented due to time constraints.

Despite solving the major thermal issues that plagued Prototype V1, the Final Prototype still experienced various temperature-related problems that hindered its performance. Moving the brushless motor and ESC outside of the propulsion module significantly decreased their operating temperatures and allowed the module to be physically tested. However, the wired connection between these components was still designed to occur inside of the electronics housing, presenting a new set of thermal issues. Although the operating temperatures of the motor and ESC remained close to ambient water temperature, the wires inside of the electronics housing still spiked to dangerous temperatures under load, causing multiple motor wire failures with both Prototype V2 and the Final Prototype. The high motor wire temperatures also negatively impacted the LiPo battery's operating temperature as the wires were located directly above the battery. When the LiPo battery was thermally tested inside the test box, maximum operating temperatures never exceeded the recommended thermal limit of 70 C. When tested inside Prototype V2 and the Final Prototype, maximum battery operating temperatures routinely exceeded 70 C.

Moving the motor and ESC wires outside of the electronics housing and mounting them externally would allow the wires to be water-cooled by the surrounding environment. This would also diminish the need for a large electronics housing. The electronics housing adds a significant empty cavity volume to the module, requiring 910.65 g of ballast to achieve neutral buoyancy on the Final Prototype. A compact electronics housing, designed to allow access to the motor mount and accommodate the LiPo battery, would eliminate a significant amount of empty volume from the module and substantially reduce its final mass.

The impeller, waterjet channel, and intake could all be further optimized for increased propulsion module performance. The 2-blade impeller, introduced for final testing, emerged as the best of the four impellers. Additional design refinements to improve its thrust to drag ratio will increase the impeller's efficiency and reduce the applied load on the brushless motor. The waterjet channel and intake functioned as intended. However, optimizing the dimensions of these components will also enhance the module's efficiency and performance.

The 30 mm overlap dual-channel nozzle tested during this study showed promise, increasing thrust output relative to the single-channel nozzle by 8.25%. Overlap distance was the only design parameter tested due to time constraints. Further analysis into the effects of altering other nozzle parameters, such as outer channel dimensions, will need to be completed to improve performance and efficiency. As discussed in Section 2.3, the primary theoretical benefit of the dual-channel nozzle is the ability to generate additional efficient hydrodynamic thrust when the module has a forward velocity greater than 0. A testing plan will need to be designed and

completed to verify this theory. This propulsion module never required a control system as all testing was completed using the static testing apparatus. To test the performance of the dual-channel nozzle when the propulsion module has a forward velocity, a control system will need to be implemented to stabilize the module and control the brushless motor remotely.

The 2021-2022 University of Rhode Island's Mechanical Engineering Capstone Team 28 has taken over this project. It is currently in the process of testing a new 200 KV brushless motor and 6 cell 6000 mAh LiPo battery configuration. The 790 KV DYS 3548-6 brushless motor and 3 cell 3200 mAh LiPo battery setup achieved the target thrust objective set for this propulsion module but failed to reach an operational run-time of 30 minutes. The new 200 KV brushless motor was designed specifically for high torque applications. The additional 2800 mAh of capacity provided by the new LiPo battery will help drive the module's operational run-time closer to the 30-minute target. Both components are much larger in mass and dimensions than their counterparts featured in the Final Prototype. A redesign of the propulsion module will be required if Team 28 chooses to implement these components.

13. References

1. MakerBot. “10 Advantages of 3D Printing,” May 3, 2019. https://www.makerbot.com/stories/engineering/advantages-of-3d-printing/.

2. Ahmad, T, S L Plee, and J P Myers. “Fluent User’s Guide,” n.d., 2692.

3. Pro Tool Reviews. “Brushed vs Brushless Motors: What’s the Difference?,” March 17, 2021. https://www.protoolreviews.com/brushed-vs-brushless-motors/.

4. “Brushless Vs Brushed DC Motors: When and Why to Choose One Over the Other | Article | MPS.” Accessed October 17, 2021. https://www.monolithicpower.com/en/brushless-vs-brushed-dc-motors.

5. Bulten, Dr Norbert. “A Breakthrough in Waterjet Propulsion Systems,” n.d., 7.

6. Claus, B, R Bachmayer, and C D Williams. “Development of an Auxiliary Propulsion Module for an Autonomous Underwater Glider.” *Proceedings of the Institution of Mechanical Engineers, Part M: Journal of Engineering for the Maritime Environment* 224, no. 4 (November 2010): 255–66. https://doi.org/10.1243/14750902JEME204.

7. “Drone LiPo Battery Calculator • Electrical, RF and Electronics Calculators • Online Unit Converters.” Accessed October 31, 2021. https://www.translatorscafe.com/unit-converter/en-US/calculator/multicopter-lipo-battery/.

8. Formlabs. “FDM vs. SLA: Compare the Two Most Popular Types of 3D Printers.” Accessed October 26, 2021. https://formlabs.com/blog/fdm-vs-sla-compare-types-of-3d-printers/.

9. Jiao, Weixuan, Li Cheng, Di Zhang, Bowen Zhang, Yeping Su, and Chuan Wang. "Optimal Design of Inlet Passage for Waterjet Propulsion System Based on Flow and Geometric Parameters." *Advances in Materials Science and Engineering* 2019 (October 24, 2019): 1–21. https://doi.org/10.1155/2019/2320981.

10. Jos, Dunărea de. "Theoretical Approaches Regarding the VENTURI Effect," no. 3 (n.d.): 5.

11. LEFEET. "LEFEET S1." Accessed December 7, 2021. https://www.lefeet.com/products/lefeet-s1-underwater-scooterchristmas-sale.

12. Merza, Saeed A. "Propulsions for Deep-Sea Research Applications," n.d., 106.

13. Parsons, Richard. "Things in Motion: How to Estimate the Torque of a BLDC (PMSM) Electric Motor Using Only Its Kv and Current Draw." *Things in Motion* (blog), December 25, 2018. https://things-in-motion.blogspot.com/2018/12/how-to-estimate-torque-of-bldc-pmsm.html.

14. SCUBAJET. "SCUBAJET PRO Underwater Kit." Accessed December 7, 2021. https://www.scubajet.com/shop/accessories/scubajet-pro-underwater-kit/.

15. Shahrubudin, N., T.C. Lee, and R. Ramlan. "An Overview on 3D Printing Technology: Technological, Materials, and Applications." *Procedia Manufacturing* 35 (2019): 1286–96. https://doi.org/10.1016/j.promfg.2019.06.089.

16. Wislicenus, George F. "Hydrodynamic Design Principles of Pumps and Ducting for Waterjet Propulsion:" Fort Belvoir, VA: Defense Technical Information Center, June 1, 1973. https://doi.org/10.21236/AD0775620.

17. Yamaha Seascooters. “YAMAHA RDS250 SEASCOOTER.” Accessed December 7, 2021. https://yamahaseascooters.com/products/yamaha-rds250-seascooter.

18. Zhao, Prepared Jian, and Yangwei Yu. “Brushless DC Motor Fundamentals Application Note,” 2014, 19.